Department of Physics and Astronomy
Heidelberg University

Bachelor Thesis in Physics
submitted by

Julia Schlägel

born in Waiblingen (Germany)

2024

Neutral meson measurements with the Photon Conversion Method in ALICE Run 3 in proton-proton collisions at $\sqrt{s} = 13.6$ TeV

This Bachelor Thesis has been carried out by Julia Schlägel at the
Physikalisches Institut Universität Heidelberg, Heidelberg (Germany)
under the supervision of
Prof. Dr. Johanna Stachel

Abstract

For the LHC Run 3, upgrades to the detector of the ALICE experiment were made. These upgrades lead to many changes which have to be understood and implemented in the also new Online-Offline (O^2) system. This thesis focuses on the analysis of two neutral mesons - the π^0 and the η meson- with the goal of obtaining their differential cross sections. By doing this analysis simultaneously on their two main decay channels, the $\gamma\gamma$-decay and the Dalitz ($e^+e^-\gamma$) decay, the GEANT implementation of the detector material budget can be checked and the performance of the new V^0-finder can be analysed.
The analysis is started by doing an invariant mass calculation for the two mesons, from which the raw yield can be extracted. After that, corrections in terms of the geometrical acceptance and the reconstruction efficiency have been applied to finally obtain the differential invariant yields. In order to compare between the two decay modes, a ratio of (0.882 ± 0.065) for the π^0 meson was fitted to the resulting invariant yield. Furthermore, the results are compared with the PYTHIA 8 model prediction and the results from ALICE Run 2 at a collision energy of $\sqrt{s} = 13$ TeV. Finally the η/π^0 ratio is also calculated. These results agree with the universal trend measured at lower energies.

Für den LHC Run 3 wurden Verbesserungen am Detektor des ALICE-Experiments vorgenommen. Diese Upgrades führen zu vielen Änderungen, die nun verstanden und in das neue Online-Offline (O^2) System implementiert werden müssen. Diese Bachelorarbeit konzentriert sich auf die Analyse von zwei neutralen Mesonen - dem π^0- und dem η-Meson - mit dem Ziel, deren differentielle Wirkungsquerschnitte zu erhalten. Durch die gleichzeitige Analyse der beiden Hauptzerfallskanäle, dem $\gamma\gamma$-Zerfall und dem Dalitz ($e^+e^-\gamma$)-Zerfall, kann die GEANT Implementierung des Materialbudgets überprüft und die Performance des neuen V^0-Finder analysiert werden.
Die Analyse beginnt mit der Berechnung der invarianten Masse für die beiden Mesonen, aus welcher der Rohertrag extrahiert werden kann. Danach werden Korrekturen in Bezug auf die geometrische Akzeptanz und die Effizienz der Rekonstruktion angewendet, um schließlich den invarianten Ertrag zu erhalten. Um zwischen den beiden Zerfallsarten zu vergleichen, wurde ein Fit an das Verhältnis der invarianten Erträge angelegt, welcher einen Wert von (0.901 ± 0.024) für das π^0 meson ergab. Des Weiteren wird in dieser Arbeit der Vergleich mit der PYTHIA 8 Modellvorhersage und den Ergebnissen von ALICE Run 2 bei einer Kollisionsenergie von $\sqrt{s} = 13$ TeV gezogen. Schließlich wird auch das η/π^0 Verhältnis berechnet. Diese Ergebnisse stimmen mit dem Trend der Messungen, die bereits bei geringeren Energien durchgeführt wurden, überein.

Contents

1 Introduction

1.1 Motivation

In particle physics the primary goal is to explore and understand the smallest and most fundamental constituents of the universe. To do so particle accelerators are of great benefit. The largest of such an accelerator is the Large Hadron Collider (LHC) located at the research center Conseil européen pour la Recherche nucléaire (CERN). A Large Ion Collider Experiment (ALICE) is one of the main experiments of the LHC and focuses on strongly interacting matter and the formation of the so-called Quark-Gluon Plasma. Many components of the experiment were upgraded during the Long Shutdown 2, which lasted from 2019 until 2022. Also a new Online-Offline (O^2) framework was added, where the upgraded detector was implemented using Geant [1]. Therefore, the implementation of the new properties into the Monte Carlo simulation has to be investigated and the particle reconstruction performance has to be analysed.

Within the scope of this bachelors thesis two neutral mesons, the π^0 and the η, will be analysed and their properties will be investigated. Moreover, the two main decay channels consisting of the two γ decay

$$\pi^0(\eta) \rightarrow \gamma\gamma \tag{1}$$

and the Dalitz decay

$$\pi^0(\eta) \rightarrow e^+e^-\gamma \tag{2}$$

will be the main interest.
There are two reasons why it is important to study and compare these two decay channels. At first the Geant material budget implementation can be investigated with these decay modes. This is of interest as the material budget of the experiment changed for Run 3 and the third version of the V^0 finder was used [2]. This new V^0 finder has now the advantage of being able to take ITS, ITS-TPC, and TPC only tracks into account, as well as being able to work at higher interaction rates. The two γ decay mode has two photons as constituents and therefore, the material enters quadraticaly. Whereas the Dalitz decay only enters linearly. The comparison of the two decay modes allows important conclusions concerning the material budget and its implementation in the Monte Carlos Simulations. Secondly, ALICE got upgraded to be able to do a continuous read out for Run 3. But this makes the V^0 method more complicated as it uses secondary tracks, and some ambiguity in the track to collision association process may appear. For the Dalitz decay the two primary tracks fix the collision of interest and therefore only if the photon belongs to the same collision a neutral meson can be reconstructed. By comparing the differential meson production cross section measured in the two decay channels it would be possible to make a statement about how good the two issues are understood.

Furthermore, the neutral meson differential cross section has already been measured for Run 2 of the ALICE detector at an energy of $\sqrt{s} = 13.0$ TeV. One can continue the research by comparing these results to the ones obtained at $\sqrt{s} = 13.6$ TeV.

The first chapter of this thesis shall give a short introduction into the physical background needed for the analysis. Namely this will be the Standard Model of particle physics, Quantum Chromo Dynamics and the Quark-Gluon Plasma. In chapter 2 the photon interactions needed for the detection and photon reconstruction process will be discussed. After that, the ALICE detector will be introduced in chapter 3. The five most important detector devices - the Inner Tracking System, the Time Projection Chamber, the Transiton Radiation Detector, the Time-of-Flight Detector and the Fast Interaction Trigger - will be discussed. As in this thesis the photons get reconstructed with the Photon Conversion Method, chapter 4 contains a detailed description of this method. Also all applied selection criteria for the photon and the virtual photon reconstruction are listed and explained in this chapter. The used data sets and Monte Carlo simulations as well as the analysis procedure is presented in chapter 5. In chapter 6 the results of the analysis of the neutral mesons can then be found. Not only the analysis of the invariant mass and the process of obtaining the raw yield is discussed there, but also a detailed description of all applied corrections and multiple comparisons of the results. Finally, chapter 7 gives the final conclusion and a short outlook of what still needs to be done.

1.2 The Standard Model

Up until today the Standard Model is the best established model in particle physics. It was developed in the 1970s and provides an understanding of how particles and three of the fundamental forces are related [3].

In general the model, which can be seen in fig. 1, distinguishes between two basic types of particles: leptons and quarks. As long as the particles have a half-integer spin they are also called fermions. Each type consists of three generations with two particles in each. Every generation differs in stability and weight, so that the first generation is the most stable one and the second and third generation are heavier and less stable. All ordinary matter is formed out of first generation particles.

There are four fundamental forces in total: gravity, the electromagnetic force, the weak force and the strong force. The forces vary in strength, range and in their force-carrier particle. The particles which mediate the interactions between fermions are bosonic and have an integer spin. They correspond to a specific fundamental force as for example the gluon to the strong interaction, the photon to the electromagnetic interaction and W- or $Z^{\pm}$-bosons to the weak interaction.

Gravity is the only fundamental force which is not covered by the Standard Model. On the

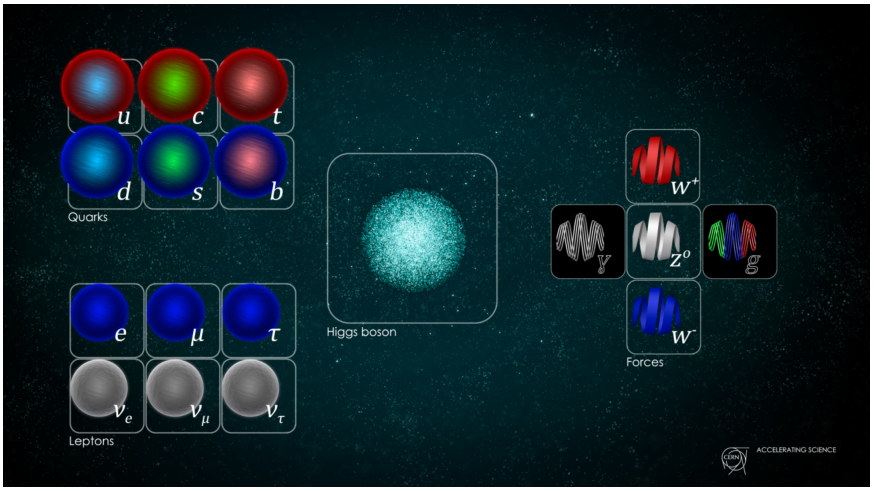

Figure 1: Illustration of the Standard Model and its constituents the quarks, leptons and forces [3]

minuscule scale of particles, it is so weak as to be negligible. The Standard Model still describes most of physics correctly. But the model is not complete and has some gaps. For example it can not yet describe dark matter [3].

1.3 Quantum Chromodynamics (QCD)

Quarks exhibit another particle characteristic: they have colour-charge. Between colour-charge carrying particles strong interaction takes place. Quantum Chromodynamic is the quantum field theory which describes this strong interaction. The colours are called red, green and blue as well as their respective anti-colours anti-red, anti-green and anti-blue. But not only quarks but also gluons can be charged with colour. This feature differentiates the gluon from other mediator particles as for example the photon which does not carry any electric charge to mediate the electromagnetic force. There are in total eight gluons that, by exchanging colour, can link with quarks, anti-quarks and other gluons.

Strong interaction is known for confining quarks inside of hadrons.The potential between quarks is given as

$$V_{q\bar{q}} = -\frac{4}{3}\frac{\alpha_s}{r} + \kappa r. \tag{3}$$

With this potential quarks can only be separated at infinite energy. When it comes to working with Quantum Chromo Dynamics (QCD), the coupling constant α_s must be known. But α_s is known for the asymptotic freedom, which means that it decreases with higher momentum transfer. For small values of α_s, perturbation theory can be applied. For larger values only lattice calculations can be used to solve a problem [4].

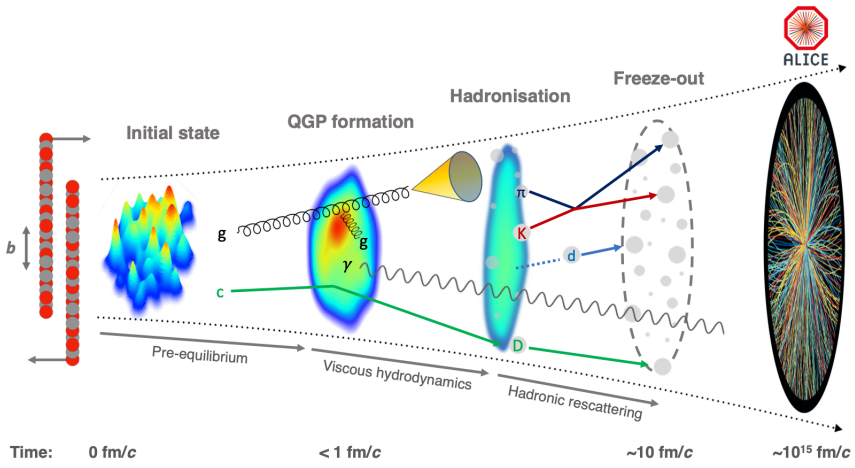

Figure 2: Evolution of a heavy ion collision, from left to right the timeline is visible beginning with the collision, the formation of the QGP and up to the freeze-out [7]

1.4 Quark-Gluon Plasma

At extremely high temperatures and densities a new state of matter can be observed: the Quark-Gluon Plasma (QGP). This state of matter is the main research interest of the ALICE program and of particular interest as shortly after the Big-Bang the universe was in this condition for a small period of time [5, 6, 7]. However, the collisions of interest will be proton-proton collisions rather than heavy-ion-collisions and therefore the QGP will not be a primary focus of this thesis. But as the QGP represents the principal research objective of the ALICE detector, a brief discussion of its properties is given in this section.

The high densities or temperatures lead to some interesting observations as quarks are no longer confined in hadrons, but can move freely.

In a laboratory these conditions can be imitated by colliding heavy ions at ultra-relativistic energies. The evolution of such a process is illustrated in fig. 2. As the particles get accelerated to velocities close to the speed of light Lorentz dilatation takes place and the particles assume the shape of discs. When colliding the heavy ions a fireball is formed, and after about 1 fm/c the Quark-Gluon plasma can be observed. As the cooling process continues the matter expands and starts to hadronize. This means that some quarks again get confined inside of a hadron. Eventually every quark is back in a confined state and the so-called freeze-out takes place. The formed hadrons scatter in all directions and have to be detected by multiple detectors to analyse them [7].

2 Photon interactions

As photons can not be detected directly, it is only possible to detect a photon via its interactions with matter or the detector material. This section should give a short overview of the interactions used in experiments to track electrons in detectors. The first part of this chapter shall discuss interactions of photons with matter which contains the photoelectric effect, Compton scattering as well as the process of pair production. Interactions of electrons with the detector material can be found in the second part of this chapter. These processes are of particular interest and required to understand the procedures which happen in the detectors. Therefore ionisation, bremsstrahlung and transition radiation will be described.

2.1 Interactions of photons with matter

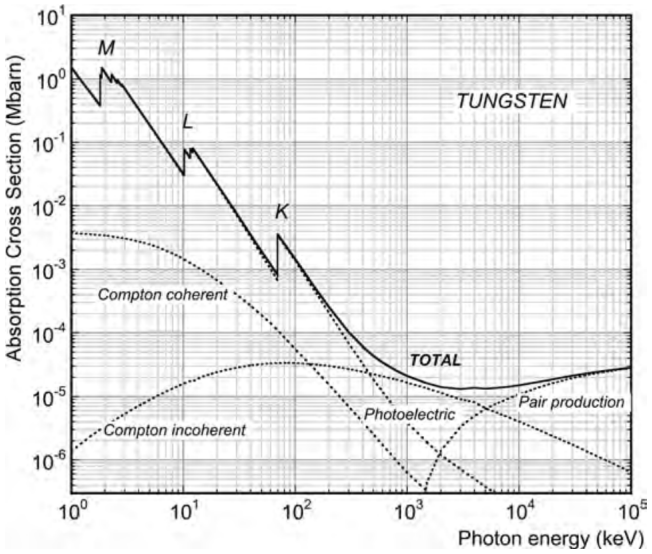

Figure 3: Absorption cross section of photons [8]

In fig. 3 the absorption cross section can be seen for different photon energies. This illustrates at which energy which process dominates. So at lower energy levels Compton scattering, at energies of around $1{\cdot}10^3$ keV the photoelectric effect and at high energies pair production dominates.

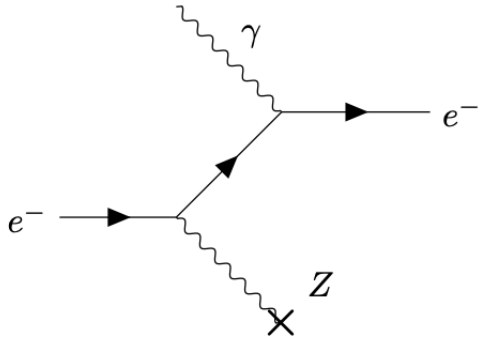

Figure 4: Feynman diagram for the photoelectric effect

2.1.1 The photoelectric effect

The photoelectric effect describes a process in which a photon gets fully absorbed by a shell electron. This shell electron has a kinetic energy of the following size:

$$E_{kin} = h\nu - E_b \tag{4}$$

where E_b is the binding energy of the absorbed photon. With this energy the shell electron gets emitted. The whole process is graphically shown in the Feynman-diagram in fig. 4.

This effect can not occur with a free electron as for conservation of momentum and energy an atom has to be involved. The cross section of the photoelectric effect is given by [9]

$$\sigma_{ph} \propto \frac{Z^5}{E_\gamma}. \tag{5}$$

Where E_γ is the energy of the photon and Z is the atomic number.

2.1.2 Compton scattering

In medium energy regimes around 50 keV to 500 keV Compton scattering takes place. This photon interaction basically happens when an incoming photon diffuses by an electron. That process can be seen in fig. 5. A present nucleus is not required since the scattering can happen with a free or quasi-free electron, as long as the energy of the shell electron is smaller than the energy of the incoming photon [8]. From this interaction a photon with the energy

$$E_\gamma^{'} = \frac{E_\gamma}{1 - \frac{E_\gamma}{m_e c^2}(1 - cos(\theta))} \tag{6}$$

is outgoing. Where m_e stands for the mass of the electron, c for the speed of light, E_γ for the energy of the incoming photon and θ for the scattering angle [4].

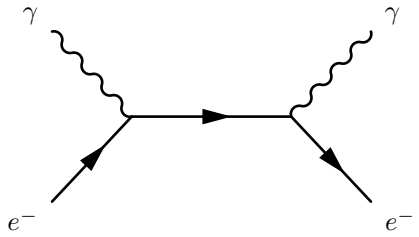

Figure 5: Feynman diagram for Compton scattering

The cross section for this process is given by

$$\sigma_{compton} \propto \frac{Z}{E_\gamma} \tag{7}$$

[9].

2.1.3 Pair production

At high energies of at least 1.02 MeV pair production becomes the dominant effect [8]. It describes the process of a photon converting into an electron-positron pair. Again this process can be seen in the Feynman-diagram in fig. 6.

Similar to the photoelectric effect an atomic nucleus needs to be present to conserve momentum and energy. The pair production cross section can be expressed as

$$\sigma_{pair} = \frac{7}{9}\frac{A}{\rho N_A}\frac{1}{X_0} \tag{8}$$

in the high energy limit. Where N_A stands for the Avogadro number, ρ for the density of the material, A for the atomic number of the material and X_0 for the radiation length.

2.2 Interactions of electrons with the detector material

As photons convert into electrons one can obtain many particle characteristics by measuring electrons. That is why this section focuses on explaining three possible electron detection processes that are used in the ALICE detector.

2.2.1 Ionisation

When passing through a medium, a charged particle exerts a force on the bound electrons of the medium atoms due to its charge. This results in a momentum transfer which ionises the

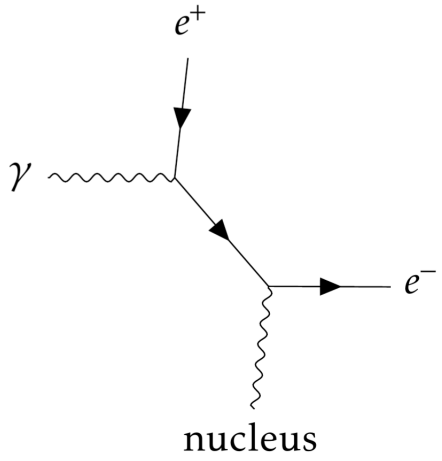

Figure 6: Feynman diagram for pair production

atoms. The equation describing this process is the Bethe-Bloch formula [4, 10]

$$-\left\langle \frac{dE}{dx} \right\rangle_{ion} = 4\pi N_A r_e^2 m_e c^2 z^2 \rho \frac{Z}{A} \frac{1}{\beta^2} \left[\frac{1}{2} ln \left(\frac{2m_e c^2 \gamma^2 \beta^2 T_{max}}{I^2} - \beta^2 - \frac{\delta}{2} \right) \right]. \tag{9}$$

This equation takes many arguments which are explained in the following:

- N_A stands for the Avogadro number
- r_e is the classical electron radius
- z stands for the charge of the incoming particle
- β is the velocity of the traversing particle
- ρ describes the density of the material
- Z is the atomic number
- A stands for the weight of the atom
- γ is the Lorentz factor
- I describes the mean excitation energy of the medium
- and finally the term $\frac{\delta}{2}$ is a density correction.

This formula is of particular interest as it allows for the differentiation of particles based on their respective shapes of the Bethe-Bloch curve. Consequently, particle identification can be

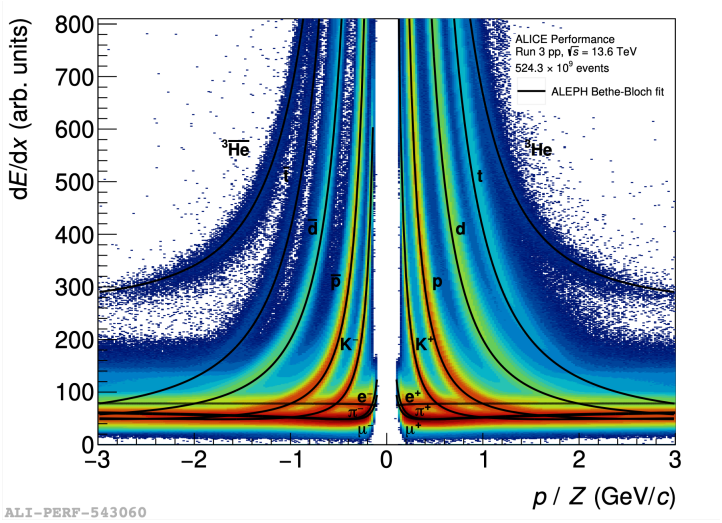

Figure 7: Specific energy loss dE/dx from ALICE Run 3 plotted versus rigidity, in black the Bethe-Bloch curve obtained from theoretical calculations is shown for different particles [11]

achieved through the measurement of energy loss and momentum.

In fig. 7 a plot of the specific energy loss dE/dx can be seen. In practice one can choose an interval around the expected Bethe-Bloch curve for a particle. Every particle with an energy loss outside of this chosen area is not identified as the wanted particle.

2.2.2 Bremsstrahlung

Electrons with high energies mostly loose their energy via Bremsstrahlung. This effect occurs if an electron gets deflected in the electric field of a nucleus and to conserve energy a photon gets sent out. The electron links with the nucleus and emits a photon. For Bremsstrahlung to happen the presence of a nucleus is mandatory. In this process the electron experiences energy loss of the form [4, 10]

$$-\left(\frac{dE}{dx}\right)_{Brems} = 4\alpha N_A \frac{z^2 Z^2}{A}\left(\frac{1}{4\pi\epsilon_0}\frac{e^2}{mc^2}\right)^2 E\ ln\left(\frac{183}{Z^{1/3}}\right) \propto \frac{E}{m^2} \tag{10}$$

where especially the proportionality gives an important statement. As the equation is mass dependant, Bremsstrahlung is only relevant for electrons and positrons and can be ignored for particles heavier than that.

2.2.3 Transition radiation

The phenomenon known as transition radiation occurs in consequence of a high energy particle traversing the interface between two distinct dielectric media with different refractive indices.

The electric field configuration changes and as a result electromagnetic radiation is emitted in form of photons. The angular distribution of this radiation has its peak at

$$\theta \simeq \frac{1}{\gamma} \tag{11}$$

with γ being the Lorentz factor [10]. The principle of transition radiation gets employed in the Transition radiation detector of ALICE [12, 13].

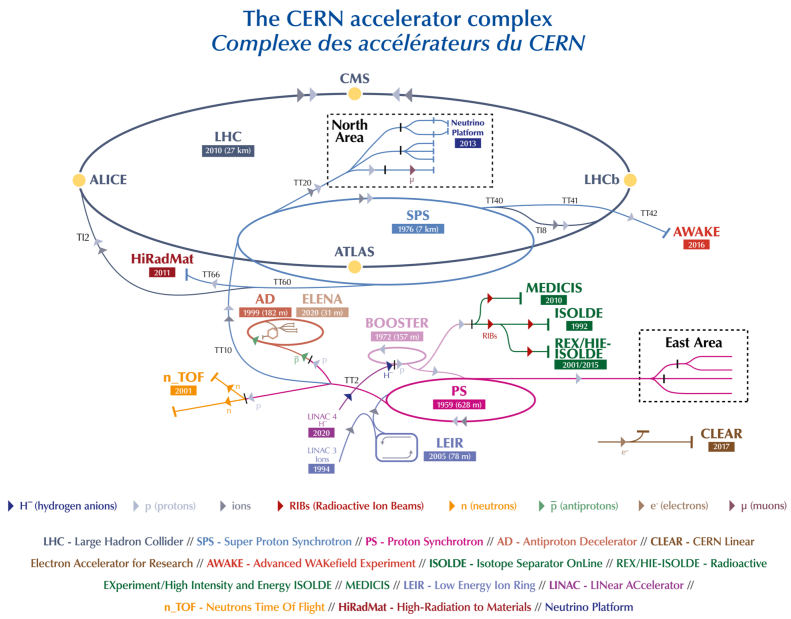

Figure 8: The CERN accelerator complex [15]

3 The ALICE detector

The data used in this thesis was obtained and made available by the European Organization for Nuclear Research CERN. CERN is located in Geneva, a city close to the French-Swiss border. Said organisation has committed itself to high energy particle physics and is most famous for providing a great particle accelerator complex, which is shown schematically in fig. 8. One of the particle accelerators is the Large Hadron Collider which - with a circumference of about 27 km - is until now the largest particle accelerator in the world. Since the first start of the LHC in September 2008, high energy beams have travelled inside the accelerator ring and got made to collide. In sum this accelerator complex has eight interaction points and four of them are equipped with experiments. This provides the possibility of various physical applications [14].

ALICE is located at Interaction Point 2 (IP2). This detector of special interest for this thesis is shown in fig. 9. The experiment is fully committed to heavy-ion physics and the study of the Quark-Gluon Plasma. Therefore, the detector was developed according to the goal of recreating situations similar to the universe shortly after the Big Bang. As explained in section 1.4 heavy ions have to collide at high energies to achieve this. For further research and understanding, the ALICE detector also records data for proton-proton and proton-lead collisions. The 26 m long, 16 m wide and 16 m high ALICE detector weighs about 10.000 tonnes and works with

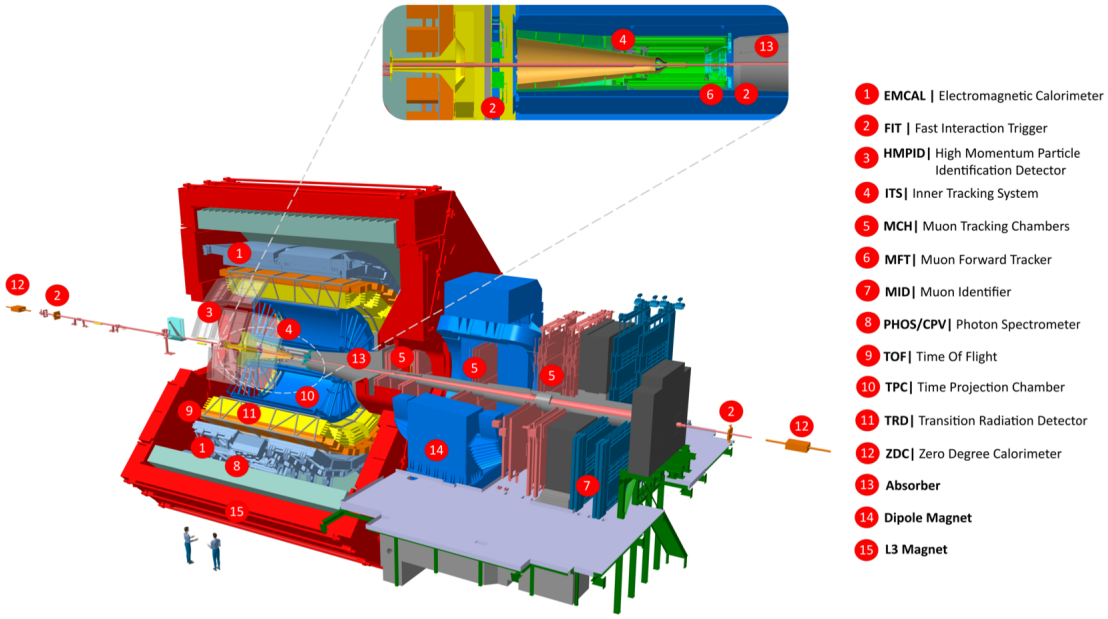

Figure 9: schematic representation of the ALICE detector used in Run 3 [17]

beams fed in by the LHC [16, 7].

The most important particle tracking detectors are the Inner Tracking System (ITS) which is the inner-most detector and the Time Projection Chamber (TPC) which uses the specific energy loss for particle identification. Not only the ITS but also the TPC got an upgrade for Run 3 of the ALICE experiment. The main change was a shift from the concept of selective event triggers to a continuous readout of all data. For more electron identification the tracking from the TPC gets carried on by the Transition Radiation Detector (TRD). Adding to that the Time of Flight (TOF) system is used, and the Fast Interaction Trigger (FIT) is applied to enhance the timing resolution. These detectors will be discussed in more detail in the following sections [7].

3.1 Inner Tracking System ITS2

As already mentioned the Inner Tracking System is the detector which the particles pass through immediately after leaving the beam pipe. This particle detection device has three main functions. First of all the ITS should determine the primary vertex with a very high resolution.

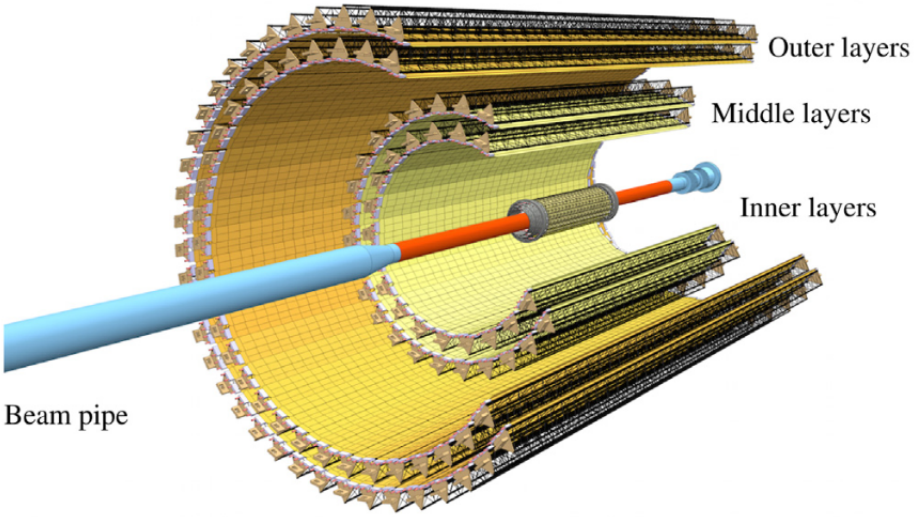

Figure 10: Schematic view of the Inner Tracking System 2 [20]

But not only primary but also secondary vertices should be reconstructed from this detector, as the secondary vertices are important for the reconstruction of charm and hyperon decays. And last but not least the ITS improves the momentum and angle resolution for the TPC [18, 19, 20].

In 2021 the ITS got replaced by the Inner Tracking System 2 (ITS 2), which can be seen in fig. 10, to give space for improvements for Run 3. The main functions and goals of the detector stayed the same but with a higher resolution. In this new detector the former six layers got replaced by seven layers which allow particles to be reassembled, based on ITS 2 information alone. One significant change of the ITS2 was to base the construction on Monolithic Active Pixel Sensors (MAPS). These sensors have the advantage of combining the charge signal collecting with the readout circuit in one underlay of silicon. The new ITS 2 consists of seven layers - all in cylindrical shape - covered with ALPIDE chips. ALPIDE chips got fully developed by ALICE and offer the benefit of a greatly reduced material budget. As the chips have the dimensions of about 50-100 μm thickness and an area of 15x30 mm^2, each chip includes more than half a million pixels [21, 18, 20, 22].

The new ITS 2 has three main advantages. First of all the impact parameter resolution is significantly improved by a factor of five in the z direction and a factor of three in the rϕ-direction. Then the tracking efficiency and the transverse momentum resolution got better at low p_T due to the seventh layer. And finally the increased readout rate is another important advantage [20].

In table 1 one can see the location of several components of the ITS 2. Due to its cylindrical

Layer	R_{min} [mm]	R_{max}[mm]
0	22.40	26.70
1	30.10	34.60
2	37.80	42.10
3	194.40	197.70
4	243.90	247.00
5	342.30	345.40
6	391.80	394.90

Table 1: Structure of the ITS2: the starting and ending radius of each layer of the ITS2 [22]

shape each location is given as a starting radius and the radius when the component ends. The first three layers listed in table 1 belong to the Inner Barrel, they are called the inner layers. Layers 3-6 are constituents of the Outer Barrel. Layer three and layer four are counted as middle layers and the last two layers as outer layers

3.2 Time Projection Chamber TPC

The Time Projection Chamber is the main tracking system for tracking charged particles and identifying them. The detector which can be seen in fig. 11 is build as a cylinder with a volume of 90 m^3 and it is filled with a gas mixture of Ne-CO_2-N_2 in a ratio of 90-10-5, respectively. This cylinder is divided into two drift regions by an electrode located in the axial center. The two plates at the end of the cylinder are divided into 18 sectors. Each of these sectors contains an inner readout channel (IROC) and outer readout channel (OROC), which means that overall the TPC has 36 IROCs and just as many OROCs.[24]
When a charged particle travels through the TPC the gas mixture gets ionized which sets electrons free. These electrons then drift towards the end plates where the readout takes place. For Run 3 a renewal of the previous readout systems by readout chambers using Gas Electron Multipliers (GEMs) was applied, to compensate for the continuous readout. GEMs are gaseous detectors made out of a thin insulating foil with Cu layers on both sides of the foil. In the TPC four of such GEM foils get stacked together and thus good particle identification is achieved

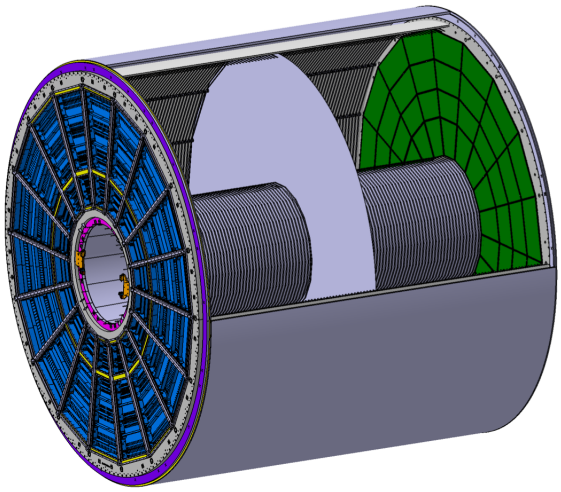

Figure 11: Schematic view of the Time Projection Chamber[23]

[24, 23].

3.3 Transition Radiation Detector TRD

The Transition Radiation Detector is located directly behind the TPC as can be seen in fig. 9. Its main purpose is to distinguish between electrons and hadrons, to provide triggering and to contribute to the track reconstruction in the central barrel. The TRD consists out of 540 detectors which are organised in 18 azimuth sectors to match with the readout chambers of the TPC. Each sector contains five stacks that each include six layers as visible in fig. 12. Each detector is filled with an active gas mixture of Xe and CO_2. It is positioned at a radial distance of 2.90 m to 3.68 m and has a length of 7 m [25, 26, 13].

The operating principle of the detector is based on the principle of Transition Radiation as the name suggests. Meaning that if a charged hadron passes through the detector the gas gets ionized, but no transition radiation takes place. If on the other hand an electron passes through the layers of the detector, a photon is emitted due to transition radiation. This photon gets absorbed close to the entrance window and this allows to distinguish between electrons and other hadrons [26].

3.4 Time-of-Flight Detector TOF

The Time-of-Flight Detector (TOF) also contributes to the particle identification via measuring the time of flight as the name of the detector already suggests. This detector is located 3.7 m

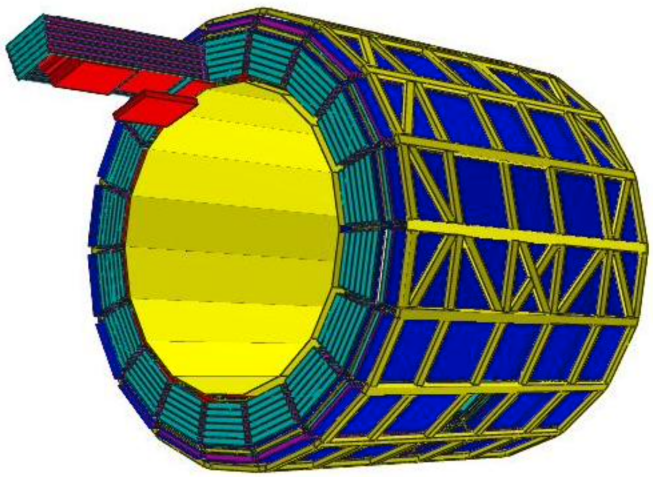

Figure 12: Schematic view of the Transition Radiation Detector

away from the interaction point and consists of a cylindrical array of Multigap Resistive Plate Chambers (MRPCs) as can be seen in fig. 13. One Gap Resistive Plate Chamber is composed of two plates parallel to each other. Between these plates there is a gap with a homogeneous electric field. When a particle traverses the gap an avalanche is created due to the sufficient high electric field. This avalanche can be measured then. The just mentioned gap is also filled with a gas to make use of every point in the detector but the space between the two plates is so small that the drift can be neglected before the avalanche sets in. A MRPCs makes use of multiple of such Gap Resistive Plate Chambers which are seperated by more resistive plates. This can be seen in fig. 14.

In total the array of the TOF consists of 1.593 of such MRPCs. And similar to the TPC and the TRD, the TOF is also divided into 18 azimuthal sectors.[29]

The identification of particles is possible by deriving the squared mass from the measured time a particle needs to travel from the vertex to the TOF. Basically one can calculate the velocity

$$\beta = \frac{L}{ct} \tag{12}$$

of a particle if the difference in time of arrival $t = t_1 - t_0$ of the particle at two places is known. If this is connected with the momentum of the particle

$$p = \beta\gamma mc \tag{13}$$

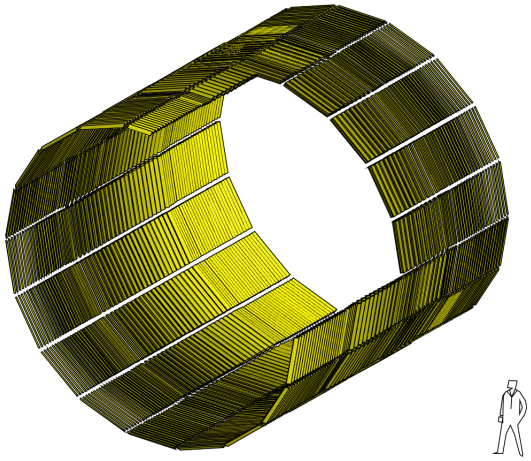

Figure 13: Time of flight detector layout [27]

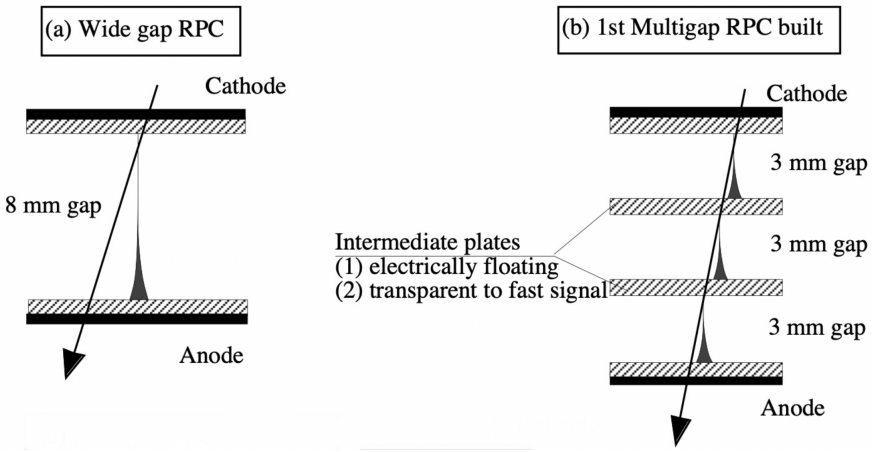

Figure 14: Schematic overview of a MRPC [28]

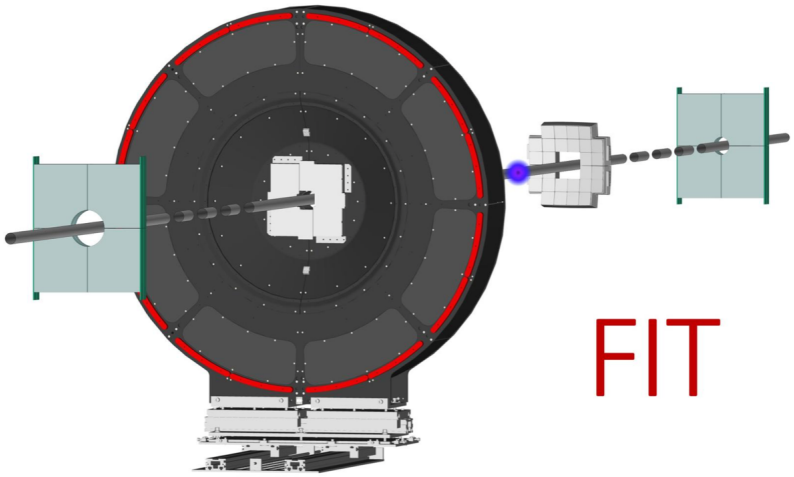

Figure 15: Constituent of the FIT detector. From left to right: FDD-A, FV0, FT0-A (FT0-A is the small quadratic structure in the center of the round FV0 structure), FT0-C and FDD-C [31]

the mass can be calculated to [30]

$$m^2 = \frac{p^2}{c^2}\left(\frac{c^2t^2}{L^2} - 1\right). \tag{14}$$

3.5 Fast Interaction Trigger (FIT)

The last detector to be discussed in more detail is the Fast Interaction Trigger (FIT) which has five different components all located along the beam pipe of ALICE as can be seen in fig. 15. These constituents are:

- the two FT0 detectors FT0-A and FT0-C which are responsible for measuring the time T0,
- the FV0 detector which makes the information on the vertex location V^0 available
- and finally the two Forward Diffractive Detectors (FDD´s) FDD-A and FDD-C.

The FT0 detector has the goal of achieving the best possible timing resolution. Therefore the FT0-A and FT0-C are both composed of a quartz Cherenkov radiator array which is coupled to Micro Channel Plate-based photomultipliers (MCP´s). These MCP´s were customized so that 64 anodes got arranged into four outputs to match with the four optically isolated quartz radiators. To further enhance the resolution of the timing, all paths the signal has to travel

along from the MCP anodes to the front-end electronic are made to be of the same length. The FT0-A contains 24 MCP´s and 96 quartz radiators and is placed at a distance of 3.3 m away from the interaction point. Whereas the FT0-C comprises 28 MCP´s and 112 quartz radiators. The FT0-C is also built in a convex shape to ensure that each quartz radiator is at the same distance of 84 cm from the interaction point. The reason for that is the closeness to the interaction point.
The second constituent of the FIT detector is the fastest trigger in the ALICE experiment: the FV0. This trigger is composed of a large segmented scintillator disk that is further split up into five rings, each covering the same pseudorapidity. The four inner rings are each divided into eight areas while the outermost ring is split into 16 subareas. These 48 sectors then get mapped into separate readout chambers for each sector via fibres. Combined with the information provided from the FT0 it is now possible to generate minimum bias and multiplicity triggers.
The last constituent of the FIT system is the FDD which can measure cross sections for diffraction and inelastic processes and studies centrality [31, 17].

4 Photon and virtual photon reconstruction

This section will focus on explaining the Photon Conversion Method, which was used to reconstruct the photons for this thesis. Adding to that this section will give all of the selection criteria that were applied on the data for the photon. Finally, the reconstruction of the virtual photons and the corresponding cuts are explained.

4.1 Photon Conversion Method

In general the ALICE detector has three possible ways to measure photons: via photon conversion in the central barrel, by using the Photon Spectrometer (PHOS) or by using the Electromagnetic Calorimeter (EMCal).
In this thesis the Photon Conversion Method (PCM) will be used to reconstruct photons with transverse momenta of 100 MeV or more. Here not the photon itself but its conversion products, the electron-positron pairs, get measured. By obtaining information about them the photon can then be reconstructed. To do so, one has to find V^0 candidates. Examples for V^0 particles are the K^0_S, the Λ, the $\overline{\Lambda}$ or in the case of this thesis the γ. Basically V^0 particles are neutral particles that can be detected via their decay products. The daughter particles in which a V^0 decays have to be charged oppositely. Therefore the decay of such a particle looks like a triangle or like the letter "V". Photon conversions are not typical V^0s as there is no decay. But as two oppositely charged particles emerge from it, one can treat it like a V^0 nevertheless.

The basic concept of such a V^0 reconstruction is to match a track which is chosen based on various selection criteria, with a track that is oppositely charged. To select the wanted V^0 candidate one has to pay attention to some criteria which can be understood in more detail by looking at fig. 16 like the ones listed here:

- The impact parameter b of each track at the primary vertex has to be large enough.
- The distance of closest approach (DCA) between the two tracks at the secondary vertex has to be smaller than a certain value.
- The secondary vertex has to be inside of a fiducial volume.
- The momentum of the V^0 candidate has to point towards the primary vertex [32].

As soon as the V^0 particle is identified one has to select the photons within the V^0 candidates. For this purpose various selection criteria are to be applied.

The selection criteria for particles in table 2 are aimed at identifying photons. For this reason the Armenteros-Podolanski plot is used as it can reduce the reconstructed V^0s by the

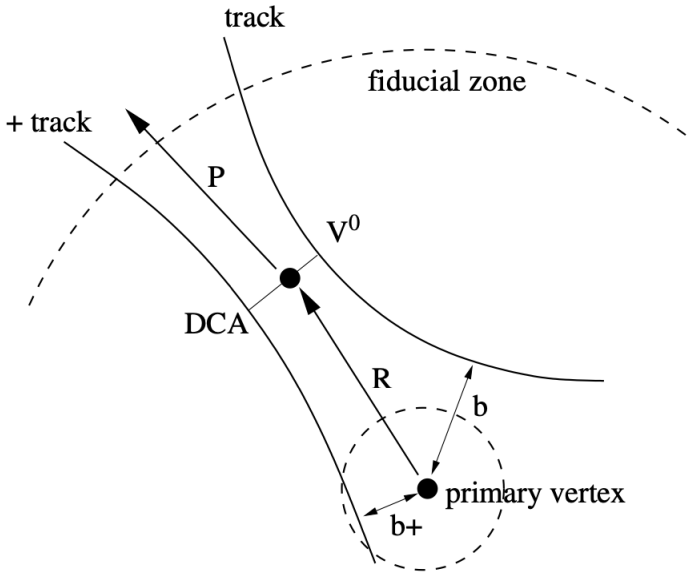

Figure 16: Geometrical overview of V^0 reconstruction [32]

background caused by the Λ, the $\overline{\Lambda}$ or the K^0_S. This plot consists of the longitudinal momentum asymmetry α

$$\alpha = \frac{p_L^{e^+} - p_L^{e^-}}{p_L^{e^+} + p_L^{e^-}} \tag{15}$$

versus the transverse momentum with respect to the mother particle q_T. Where p_L stands for the longitudinal momentum of the secondary electron or positron respectively. The transverse momentum of the electron positron pairs with respect to their mother particle is given as

$$q_T = p_e \cdot sin(\theta_{V_0,e}), \tag{16}$$

where $\theta_{V_0,e}$ is the angle between mother and daughter particle. As the two daughter particles fly away from the conversion point nearly parallel to each other, q_{T} is expected to be very small for photons. With this knowledge the cut on the Armenteros-Podolanski plot can be applied as

$$\left(\frac{\alpha_{V0}}{\alpha_{V0}^{max}}\right)^2 + \left(\frac{q_T}{q_T^{max}}\right)^2 < 1. \tag{17}$$

The values for α_{V0}^{max} and q_T^{max} can be found in table 2. To further visualize this process fig. 17 shows the Armenteros-Podolanski plot [1] before and after applying the cut. There one can see

[1] It shall be noted that for the Arementeros-Podolanski plot before the cuts the data set apass 3 was used, because the plot was not available for the apass 6, which was used for the rest of this thesis. As this plot is just for illustration purposes this will be sufficient nevertheless.

Applied cuts	min	max
χ^2 / number of clusters of the ITS	-	5
χ^2 / number of clusters of the TPC	-	4
TPC dE/dx for electron inclusion [σ]	-3	3
number of clusters in the TPC	10	-
number of crossed rows	20	-
α for the Armenteros-Podolanski cut	-0.95	0.95
q_{T} for Armenteros-Podolanski cut (GeV/c)	-	0.01
η for V^0 photons at PV	-0.8	0.8
distance between two legs [cm]	-	3
V^0 radius [cm]	4	90
cosine of pointing angle $cos(\theta_{PA})$	0.997	-
p_{T} for V^0 photons at PV	0.1	-
margin for z cut [cm]	7	-
reject V^0s on ITS IB	true	
select V^0s with correct xz	true	

Table 2: Selection criteria applied to the photons and secondary electrons (for the PCM).

the photons as the half ellipse at the very bottom of the plot.
Additional selection criteria are used to limit the rapidity of the V^0 particle at the primary vertex, to limit the value of the V^0 radius and to set the transverse momentum of the photons

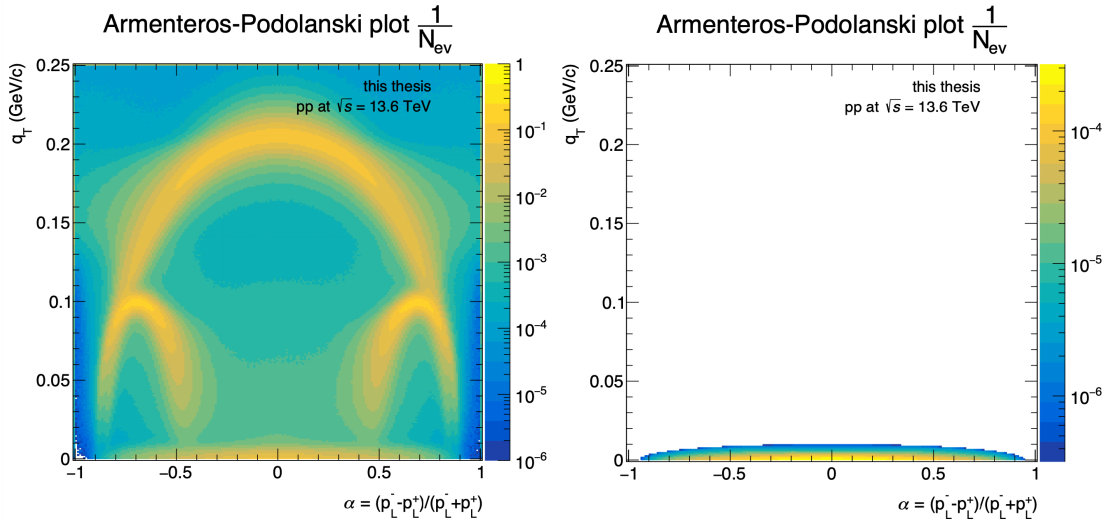

Figure 17: Armenteros-Podolanski plot before (left) and after (right) applying the cuts to seperate photons from other V^0 candidates.

at the primary vertex. The distance between the two legs of the V^0 candidate, which means the distance between the electron and the positron is also limited to three cm by the selection criteria. The particle identification takes place via the specific energy loss dE/dx in the TPC, which can be seen in fig. 7. There the specific energy loss of a particle has to be in a range of $\pm 3\sigma$ of the dE/dx of an electron for this track to be accepted. Another selection criterion concerns the pointing angle as this shows if the momentum of the photon is pointing towards the primary vertex. If that is the case the cosine of the pointing angle is expected to be one. Furthermore a line cut is applied to take the geometrical characteristics of the detector into consideration. For that every track that is outside of a fiducial area is not considered. The conversion radius has to fulfill

$$R_{conv} > |Z_{conv}|\ tan(2\arctan(exp(-\eta_{max}))) - Z_0. \tag{18}$$

Finally, the V^0 candidates from the ITS 2 Inner Barrel are rejected and only V^0 candidates with corrected xz are taken into consideration.

To give an illustration of the reconstructed photons that were used in this thesis, fig. 18 shows the distribution of reconstructed photons from the data set used. There one can see the conversion radius R_{xy} plotted over the z coordinate. This distribution is like a γ-ray tomography of the detector. And one can clearly see the structures of the detectors whose average positions are also drawn into the plot as the horizontal lines. These layers have already been mentioned in chapter 3.1 and their exact location can be found in table 1.

To further visualize this the converted photons can be plotted again, but this time from

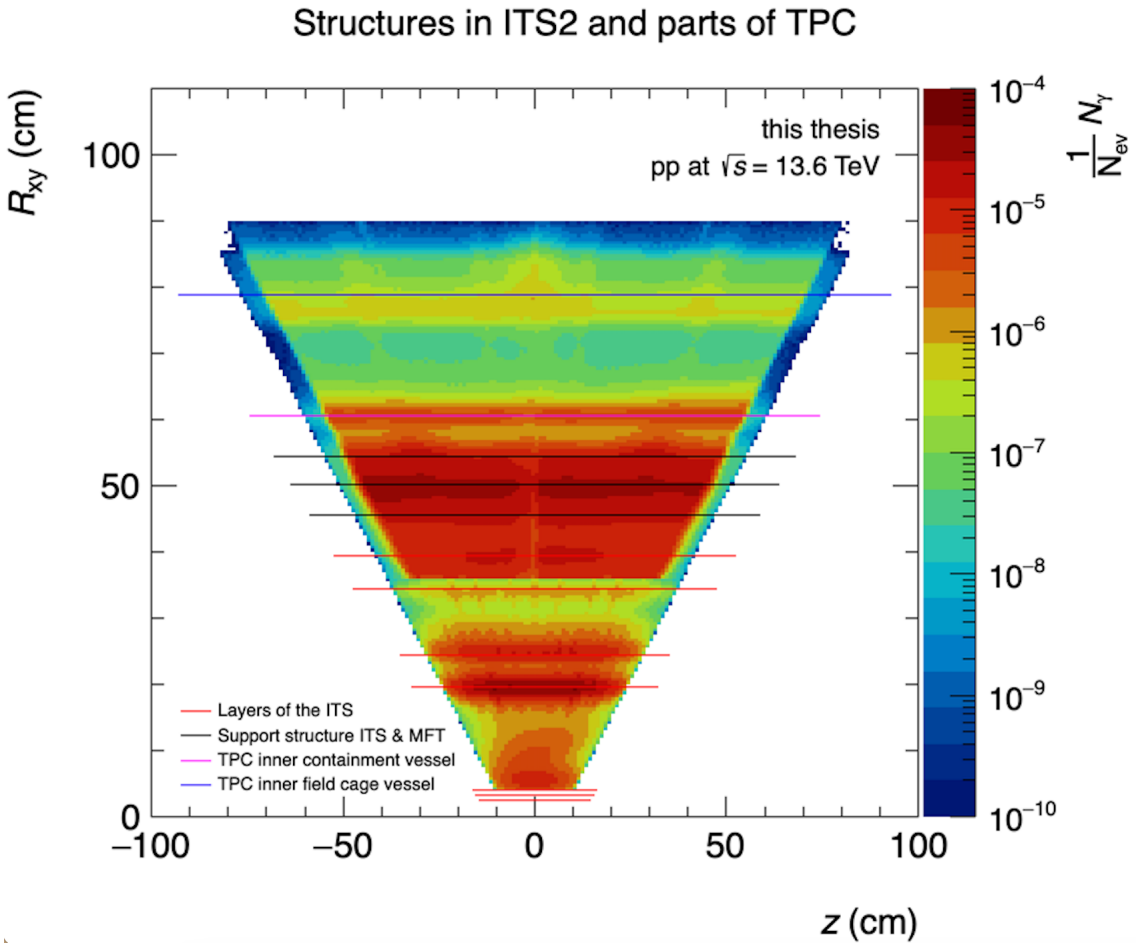

Figure 18: Plot of the normalised number of reconstructed photons drawn for the conversion radius as a function of the z coordinate of the conversion point, the lines represent the locations of different ITS2 and TPC components

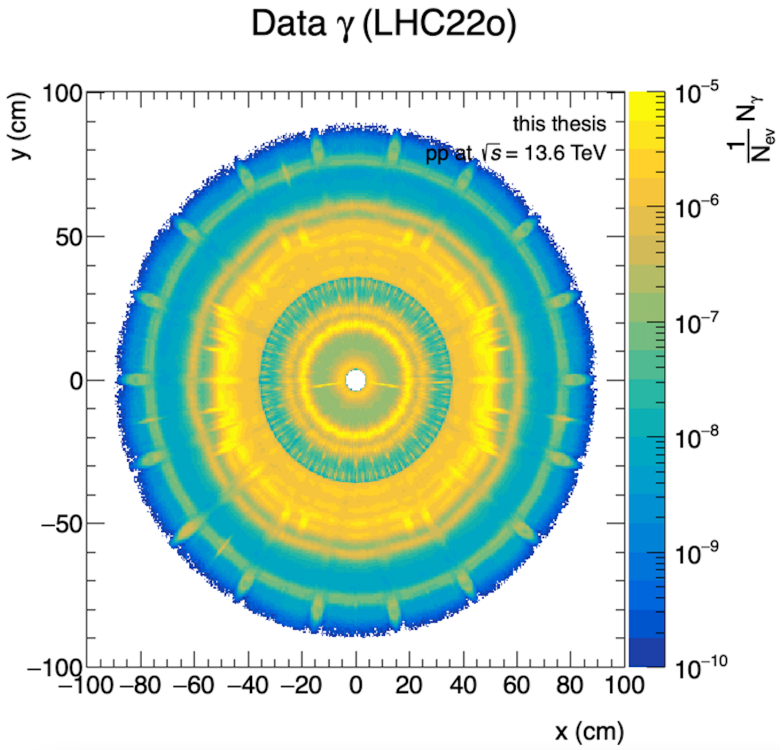

Figure 19: Plot of the normalised number of reconstructed photons for the y coordinate of the conversion point versus the x coordinate.

another point of view. The conversion radius is given as $R_{xy} = \sqrt{x^2 + y^2}$. So if the two spatial coordinates are plotted like visible in fig. 19 one gets the conversion points from a perspective 90 degrees rotated in relation to fig. 18. To make the plot more comparable with results obtained from data sets with a different number of events, this plot has already been scaled with the given number of events. Again in fig. 19 the structures from the detector can be seen.
After having reconstructed the photons one can go on and either combine two of these photons to make a pair and reconstruct π^0, or the π^0 meson can be reconstructed with the Dalitz decay. For this one would take one of the selected photons and continue with primary e^+e^- pairs.

4.2 Virtual photon reconstruction

The primary e^+e^- pairs from the Dalitz decays are combined into virtual photons. For the reconstruction of these virtual photons another set of selection criteria is applied to primary dileptons $e^\pm$. Table 3 shows these selection criteria applied to dilepton pairs i.e. primary electrons and positrons. The first selection criterion that is used here is the cut on the mass of the dileptons versus φ_v plot. The reason for this is that in data it could happen that a dilepton pair is not primary, but originates from a photon conversion. The goal of this selection criterion is to cut out photons from conversion so that only primaries are left. Therefore, the φ_v is used, which is defined as the angle between the direction of the magnetic field and the direction that is normal to the opening plane. The detailed definition of φ_v can be found in the Appendix A.2.1. e^+e^-pairs from photon conversions can only open in the plane perpendicular to the applied magnetic field, whereas the dilepton pair from the Dalitz decay can be oriented in any angle. The dileptons from photon conversions can therefore be found at the lower triangle that can be seen in fig. 20 on the left side. If the cut is applied, this triangle is no longer considered and the dilepton pairs can now be treated as primaries. The triangle used here has a slope of 0.0185 GeV/(c^2 rad.) and an intercept of -0.028 GeV/c^2.

In the selection criteria the χ^2 over the number of clusters of the ITS 2 and of the TPC is set to a maximal value. In general

$$\chi^2 = \sum \frac{(observed\ value - expected\ value)^2}{expected\ value} \tag{19}$$

is a statistical value which gives measure to the quality of the observed value. If the maximum is fixed by the selection criteria this assures to only treat high quality particles. The range of the rapidity η of a single track is also fixed to edges of ± 0.8. Various selection criteria are applied to make sure the wanted particles - the electrons and the pions to be rejected - are identified correctly. This is done via their specific energy loss, which is supposed to be within a σ-range with respect to the expected Bethe Bloch line for a given type of particle. Adding to that, criteria are applied to make sure that the particles have crossed enough clusters and rows in the detectors. Another cut sets the transverse momentum of the particles to a minimum

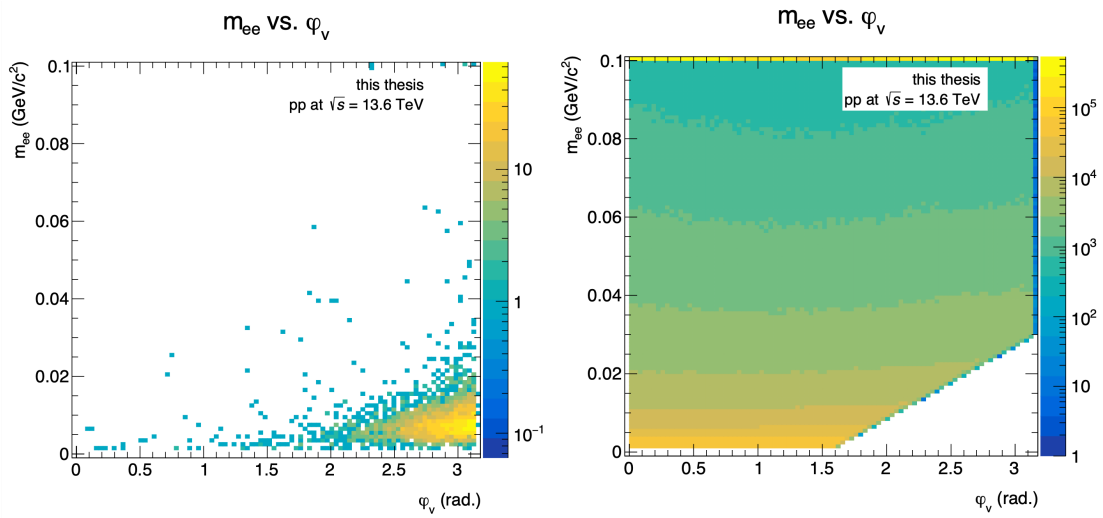

Figure 20: Plot of the mass m_{ee} versus φ_v for the dalitze ee qc data in the left side of the plot the Monte Carlo Simulation of true photons can be seen and on the right side of the plot the triangular selection criterium to cut out photons that origin from conversions has been applied.

number to again ensure good quality. Finally, one has to distinguish between the two cuts that were used for the analysis of the Dalitz decay: the dalitzee and the dalitz-itsibany. They do only differ by the requirement of hits in the ITS 2 Inner Barrel, as the dalitzee cut requires the first hit in the ITS 2 Inner Barrel and the dalitzee-itsibany requires any hit in the ITS 2 Inner Barrel.

Applied cuts	min	max
φ_v cut applied	true	-
intercept for m_{ee} vs φ_v [GeV/c^2]	-0.028	-
slope for m_{ee} vs φ_v [GeV/(c^2rad.)]	0.0185	-
χ^2 / number of clusters of the ITS	-	5
χ^2 / number of clusters of the TPC	-	4
distance of closest approach [cm]	-	0.2
pair distance of closest approach 3d [σ]	0.0	1e+10
η for single track	-0.8	0.8
TOF for electron inclusion [σ]	-3	3
TPC for electron inclusion [σ]	-2	3
TPC for pion exclusion [σ]	-1e+10	2
number of clusters in the ITS	5	-
number of clusters in the TPC	0	-
number of crossed rows	70	-
p_{T} for single track [GeV/c]	0.15	-
pid scheme	KTPConly	-
cuts	dalitzee	dalitzee-itsibany
require ITS IB 1st hit	x	-
require ITS IB any hit	-	x

Table 3: Selection criteria applied to the dileptons (virtual photons)

5 Data sets and analysis procedure

This section will give all of the needed information for the data that was used for the neutral meson reconstruction. Furthermore, the second subsection will explain the analysis procedure. An overview of all the written or modified python scripts will be given there and their purpose will be described.

5.1 Data sets and Monte Carlo

For this analysis a number of datasets were used. These datasets were all obtained by the ALICE experiment from the LHC Run 3. It shall be noted that for this thesis only pp-collisions were used. By comparing these datasets and their respective Monte Carlo simulations one can derive knowledge of how good the implementation of the characteristics of the detectors is.

period	HL train	pass	Collision energy $\sqrt{s}$	N.o.Events
Data				
LHC22o small	197579	6	13.6 TeV	24.8 10^8
LHC22o min Bias with TTCA	220661	6	13.6 TeV	46.1 10^9
Monte Carlo				
LHC24b1	197593	6	13.6 TeV	42.6 10^6
LHC24b1b with TTCA	223972	6	13.6 TeV	45.5 10^6

Table 4: Datasets that were used in this thesis ordered after data and Monte Carlo simulations

It shall be noted that the number of events of the full statistics were a lot better for data than for the Monte Carlo Simulation. This has lead to some difficulties in the analysis procedure of this thesis. But nevertheless this is 30 times more statistics for the data than there was in ALICE Run 2. The interaction rate was also increased for Run 3. It ranges and reaches 490 kHz at lowest and 513 kHz at highest. For each run number that was used for the data and Monte Carlo the belonging interaction rate can be found in table 14 in Appendix A.2.

Furthermore, some more criteria are applied to select the wanted events from the data sets. They are applied to all data sets no matter the particle and can be seen in table 5. These cuts set the Z vertex of the collision to a range in between -10 cm and 10 cm. Besides from that the event criteria require both FT0 detectors, FT0-A and FT0-C.

Applied cuts	min	max
Occupancy	-1	1e+9
Z Vertex [cm]	-10	10
require FT0AND	true	
require sel8	true	
require no time frame border	true	

Table 5: Selection criteria for the events applied to every data set

5.2 Analysis procedure

This section will provide an overview of how the data sets mentioned in section 5.1 were worked with and analysed during this thesis. For the analysis of the neutral mesons a list of python scripts to analyse the invariant mass for the π^0 has already existed. These scripts were created as part of the Bachelor´s thesis [33] and can be found on github ([34]). In order to complete the analysis and go from the raw yields to the invariant yields I adapted and extended the scripts with several new ones that can be found in table 6 and table 7, respectively. Every script needed for the analysis can be found in the git repository ([35]).

Scripts that already existed

python script	main contents
FitInvMassForPt.py	- calculates FWHM of the π^0 (η) invariant mass yield - calculates raw yield as a function of p_T - creates rootfile with the results
PlotSameAndMixed.py	plots the invariant mass for each p_T bin before subtracting the same and mixed event background
PlotInvMass.py	plots the invariant mass histogram in each p_T bin after background subtraction together with the asymmetric Gaussian fit
PlotRawYield.py	plots the π^0 (η) raw yield for different cuts
PlotParameterHistoInvMass.py	plots the parameters of the invariant mass fit: raw yield, mean, λ, σ and FWHM
PlotParametersCombined.py	plots the same parameters of the invariant mass fit, but in comparison for the different cuts
run_updated.py	steers the analysis

Table 6: Overview of the already existing and modified python macros and their contents. In black: scripts that I modified as part of this thesis, in blue: scripts that were not changed.

The basic structure contains several separately written macros that fulfill smaller tasks such as calculating or plotting a single quantity. As all of these scripts are written in the form of python classes it is then possible to collect every wanted definition in one central run file. The idea is to only have to change the inputs in this central file to run all of the analyses for different datasets, p_{T} ranges, mesons and decays. Therefore the inputs in form of the data and Monte Carlo rootfile, the rootfiles containing the results from Run 2, the configuration files, which contain the wanted p_{T} range, subsystems, fit- and integral-ranges-, and the meson which shall be analysed, need to be given.
The run file then goes through each analysis step firstly for each type, meaning for each given data file, then for each decay and in the last step, the comparison can be made while all wanted histograms have already been created.

Newly written scripts

python script	main contents
utility.py	- gets histograms from the rootfile - gets the number of events from the Hyperloop rootfile - provides the p_{T} edges for the variable binning from the configuration file - rebins the histograms
store_histograms.py	adds given histograms to a rootfile
acceptance.py	calculates and plots the geometrical acceptance [2]
efficiency.py	- calculates and plots the reconstruction efficiency - calculates and plots the product of efficiency, acceptance and branching ratio
corrected_yield.py	- calculates and plots the corrected yield - calculates and plots the PYTHIA expected yield - compares the corrected yield to the PYTHIA expected yield - fits the TCM to the corrected yield
comparison.py	- compares the results obtained with the two decay modes - compares to the results from Run 2 at $\sqrt{s} = 13$ TeV - compares between the different cuts

Table 7: Overview of the python scripts that I wrote for this analysis, and their contents

Once the code has finished, all of the results obtained are stored in a folder. The structure of this folder can be seen in fig. 21. Where each branch of the diagram visualizes one subfolder or for the bigger boxes each point stands for a graph stored inside the respective subfolder.

[2] At the moment it is not possible to calculate the acceptance and efficiency separately from the information stored in the Hyperloop train output.

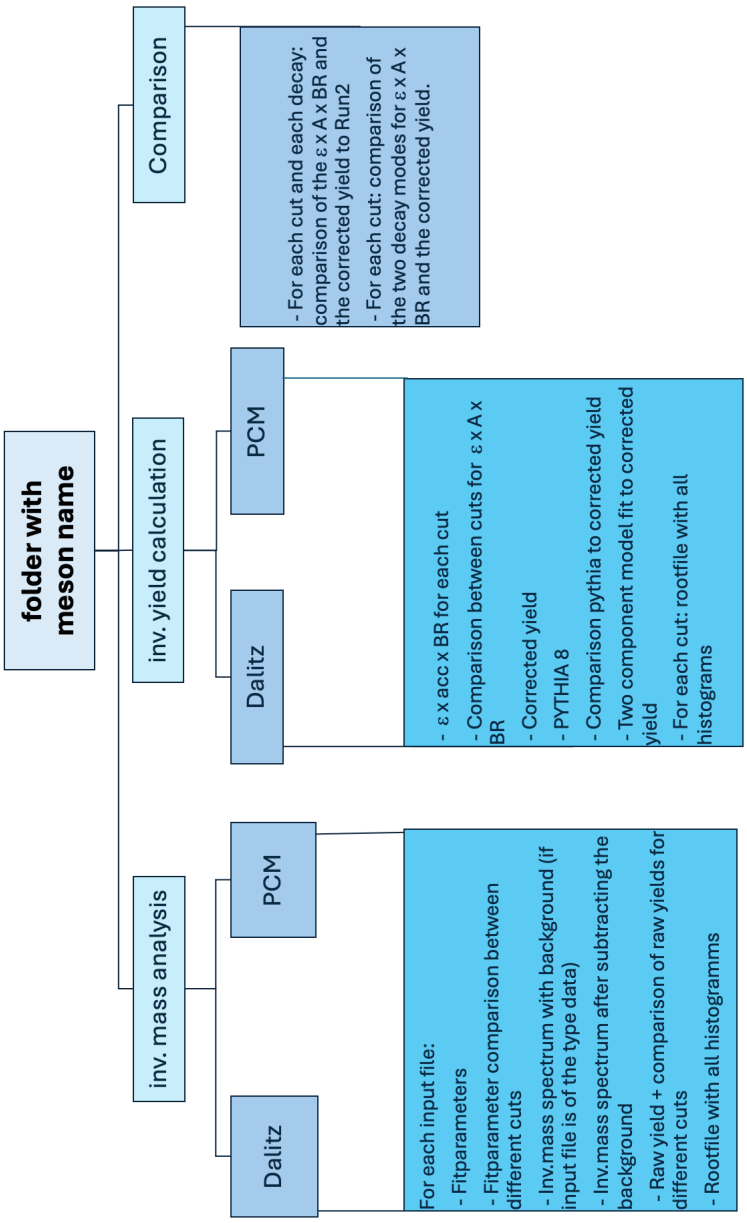

Figure 21: Structure of the folder in which the analysis results get stored.

6 Reconstruction of neutral mesons

The goal of this bachelors thesis is to measure the differential invariant yield of π^0 and η mesons. In this section the analysis procedure will be explained and the results will be shown.
First, it makes sense to familiarise with the two mesons that are going to be worked with: the π^0 and the η meson [36]. The π^0 is one of the three pion types: the π^+, the π^- and the π^0. The pions are composed of the quarks u and d. They decay via the electromagnetic force and the two main decay modes are the decay into two photons ($\gamma\gamma$) and the Dalitz decay into an electron, a positron and a photon ($e^+e^-\gamma$). The Dalitz decay can be seen in fig. 22.
The η meson consists of up, down and strange quarks as well as their respective anti-quarks.

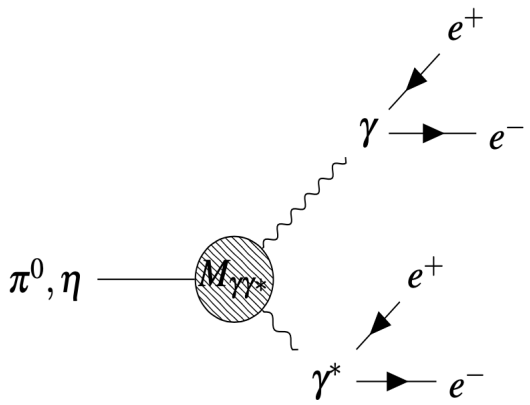

Figure 22: Feynman diagram of the Dalitz decay channel for the π^0 and η meson [37]

With a rest mass of 547 MeV/c^2 the η is more than four times as heavy as the π^0. The η also decays via the two γ and the Dalitz decay mode. But in contrast to the π^0 the Dalitz decay is a lot less frequent then some other decay modes, which shall not be discussed in this thesis. The branching ratios for the different decay modes as well as some further details on the mesons can be seen in table 8. In the following the two decay modes will be analysed for Run 3 data taken with the ALICE experiment.

There also are some selection criteria that are applied to the mesons, which can be seen in table 9.

One can see that not only the rapidity of the generated photon but also the rapidity of the reconstructed photon have a set limit of 0.8. Also the listed cuts set the amount of events with which each photon gets mixed up with in the event mixing for the background subtraction. The feed down correction to the π^0, to correct for secondary π^0 which originate from K^0_s, Λ and hadronic interactions with detector materiaal still needs to be implemented. As for the Dalitz decay one demands from the dileptons to be primary ones, this criterion will only affect the two γ decay channel.

Meson	π^0	η
Quark content	$\frac{u\bar{u}-d\bar{d}}{\sqrt{2}}$	$\frac{u\bar{u}-d\bar{d}-2s\bar{s}}{\sqrt{6}}$
Rest mass $[MeV/c^2]$	(134.9766 ± 0.0006)	(547.862±0.017)
Branching ratios:		
$\gamma\gamma$ [%]	(98.823 ± 0.034)	(39.36 ± 0.18)
$e^+e^-\gamma$ [%]	(1.174 ± 0.035)	(0.69 ± 0.04)

Table 8: Overview of the properties of the π^0 and the η meson

Applied cuts	min	max
Rapidity for generated particles	-0.8	0.8
Rapidity for reconstructed particles	-0.8	0.8
Depth for event mixing	10	-

Table 9: Selection criteria applied to the mesons

6.1 Analysis of the invariant mass of the π^0 and η

The analysis consists of different steps: the extraction of the raw yield, the extraction of the reconstruction efficiency and the geometrical acceptance and finally the calculation of the invariant yield. Each of these steps will be explained in the following section.

To start the invariant mass analysis one has to calculate the invariant mass distribution of the daughter particles. The invariant mass for the two decay channels is given as:

$$M_{\gamma\gamma}^2 = (E_{\gamma_1} + E_{\gamma_2})^2 - \left|\left|\mathbf{p}_{\gamma_1} + \mathbf{p}_{\gamma_2}\right|\right|^2 = 2E_{\gamma_1}E_{\gamma_2}(1 - cos(\theta)) \tag{20}$$

$$M_{\gamma\gamma_*}^2 = m_{\gamma^*}^2 + 2E_\gamma E_{\gamma^*}\left(1 - \sqrt{1 - \frac{m_{\gamma^*}^2}{E_\gamma^2}}cos(\theta_{\gamma\gamma^*})\right) \tag{21}$$

with the opening angle θ between the photons, E being the Energy and p being the four momenta of the respective particle which is defined as:

$$p_{\gamma_i}^\mu = \left(\frac{E_{\gamma_i}}{c}, \vec{p_{\gamma_i}}\right). \tag{22}$$

The π^0 (η) appears as a peak at its rest mass distribution on top of a combinatorial background.

The method of mixed events is used to estimate the background. This method is based on the knowledge that candidates of different events are completely uncorrelated with each other. That is why measured photons from differing events get paired up and, as these photons can never originate from the same mother particle (π^0), a peak will not appear in the invariant mass spectrum. By then choosing an integration range with its boundaries exterior to the invariant mass peak one can scale back the background calculation to the same events. The results obtained with this method can be found in the Appendix (A.3). However, this method can not describe correlations between reconstructed daughter particles as it removes correlation by definition. That is why there still remains some background, but it can be cancelled out by including a polynomial function into the used fit function. It should be noted that the background subtraction only has to be performed on data and not on a Monte-Carlo simulation as the Monte Carlo truth can be used to select the daughter particles originating from the same mother particle.

The analysis is carried out in differential intervals of the transverse momentum which were chosen based on the sufficiency of statistics. The intervals in the transverse momentum range that were chosen can be seen in table 11 and table 12 in the Appendix (A.1) for the π^0. As the statistics for the η meson were not as good as for the π^0, different intervals were chosen for each meson. The table for the η meson can be seen in table 13 in the Appendix (A.1).

To reach our goal of determining the invariant mass position, one now has to think about a fit function to suit the problem. In general a Gaussian fit is sufficient as long as it gets modified with an exponential part on the left side to account for the tail caused by Bremsstrahlung. With the Gaussian

$$G(M_d) = exp\left(-\frac{1}{2}\left(\frac{M_d - M_m}{\sigma}\right)^2\right) \tag{23}$$

where d stands for daughter pairs (d= $\gamma\gamma$ or d = $\gamma\gamma^*$) and m for mother particle respectively, the following function can be used to fit the invariant mass

$$f_{data}(M_d) = \begin{cases} A\left[G(M_d + exp\left(\frac{M_d - M_m}{\lambda}\right)\left[1 - G(M_d)\right]\right] + B + CM_d & , M_d < M_m \\ A\left[G(M_d)\right] + B + CM_d & , M_d \geq M_m \end{cases} \tag{24}$$

$$f_{MC}(M_d) = \begin{cases} A\left[G(M_d + exp\left(\frac{M_d - M_m}{\lambda}\right)\left[1 - G(M_d)\right]\right] & , M_d < M_m \\ A\left[G(M_d)\right] & , M_d \geq M_m. \end{cases} \tag{25}$$

With the parameters:

- the amplitude A
- the standard deviation σ of the Gaussian $G(M_d)$

- λ stands for the inverse slope of the tail caused by Bremsstrahlung
- the peak position of the reconstructed meson M_m
- the remaining background in terms of the offset B and finally the linear slope C.

With these fits it is now possible to determine the peak position and peak width in all transverse momentum ranges and for all cuts.

To illustrate this, fig. 23 and fig. 24 show the fit of these functions with the listed p_T ranges for the two γ decay for the π^0 and the η meson, respectively. In these plots one can clearly see a peak in the invariant mass distribution at the rest mass of each meson. So this happens at approximately 135 Mev/c^2 for the π^0 meson and at approximately 548 Mev/c^2 for the η meson. The green line which is drawn into the bins gives the mean of the Gaussian and therefore the reconstructed mass of the respective meson.
The binning of the transverse momentum range would be best if in each p_{T}- bin there were at least 100-200 entries. It shall be noted that for the η meson this was not possible in all bins, and especially in regions of higher transverse momenta it was difficult to achieve that. The anchored Monte Carlo Simulation had significantly less statistics than the data for both mesons as seen in table 4. And therefore the plots do not look as nicely as the ones in fig. 23 and fig. 24. Nevertheless these plots can be found in the Appendix A.3.
Another thing than can be seen in the plots is the fit range for each p_{T} bin as the grey dashed line. The range was chosen to go from 0.04 to 0.2 GeV/c^2 for the π^0 and from 0.4 to 0.7 GeV/c^2 for the η meson.
If one compares the plots for the π^0 to the ones for the η meson it appears that the background subtraction worked a lot better for the π^0 meson. For the fits on the η meson there still is a negative slope beneath the invariant mass peak. Whereas for the π^0 the background seems mostly gone so that the asymmetric Gaussian starts and ends at almost zero for most of the p_{T} ranges. This issue was already observed in Run 2 analyses and has nothing to do with the upgrades in Run 3.

From the invariant mass spectrum the fit parameters as well as the peak position and the peak width can be obtained. In fig. 25 the mean position of the peak, the inverse slope of the Bremsstrahlungs tail λ and the FWHM (Full Width Half Maximum) divided by 2.36 of the peak are plotted as a function of the transverse momentum. These plots serve the purpose of comparing between the results from the Monte Carlo simulation and the results from data. In ideal circumstances the ratio between the two is expected to be one. All of the plots for the fit parameters can also be found for the Dalitz decay in the Appendix A.3.1.
For the graphic of the mean value, one expects the mean of the π^0 meson to be at 0.135 GeV/c^2. But it is apparent that both, the values of the data and the values of the MC, are not in accordance with this anticipated value. They differ from the rest mass depending on p_{T} and the

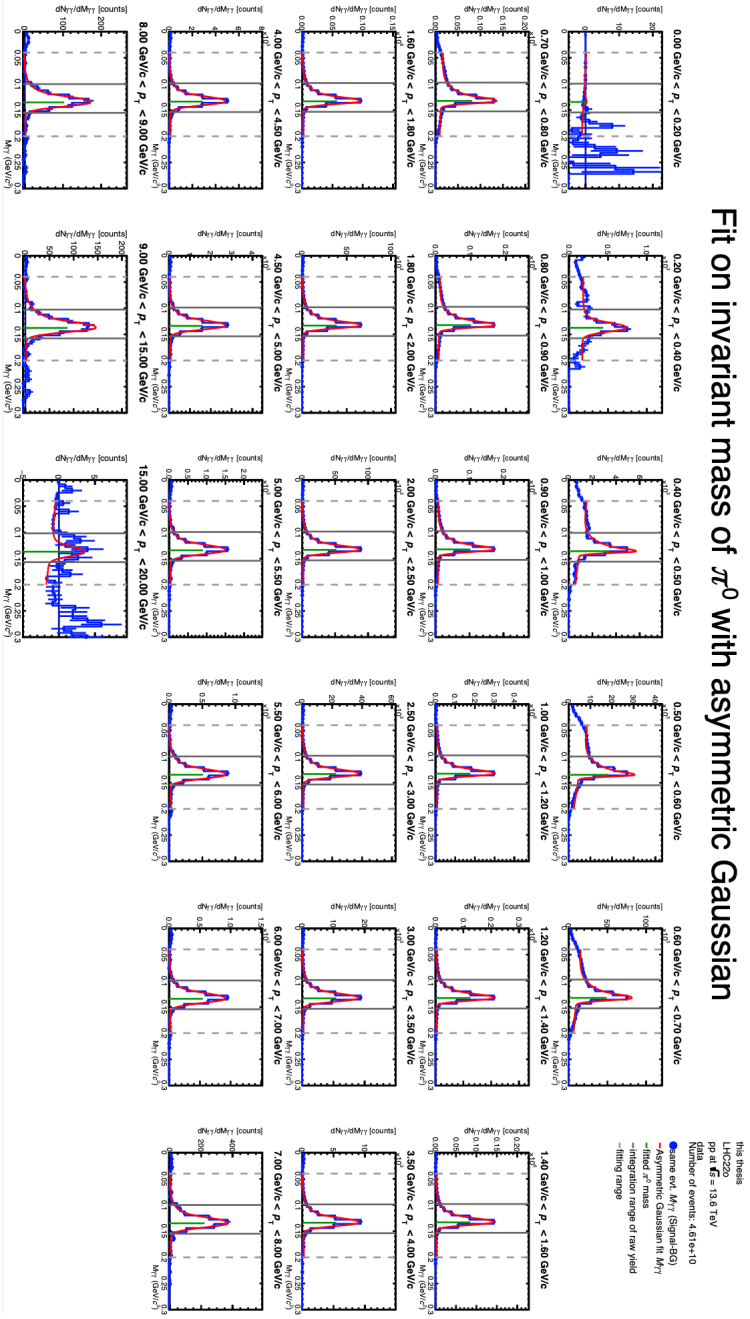

Figure 23: Fit of the asymmetric Gaussian to the invariant mass spectrum of the two γ decay after subtraction of the combinatorial background for each transverse momentum range for the π^0 meson. Here the full data set was used.

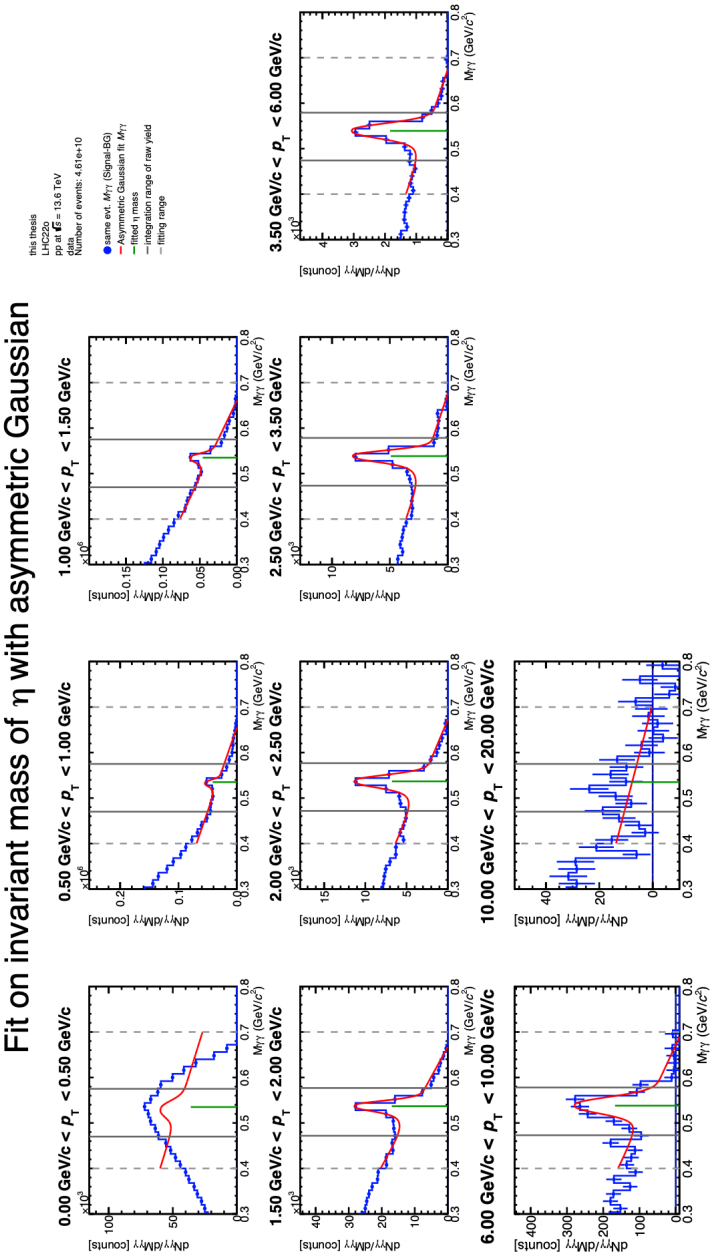

Figure 24: Fit of the asymmetric Gaussian to the invariant mass spectrum of the two γ decay after subtraction of the combinatorial background for each transverse momentum range for the η meson. Here the full data set was used.

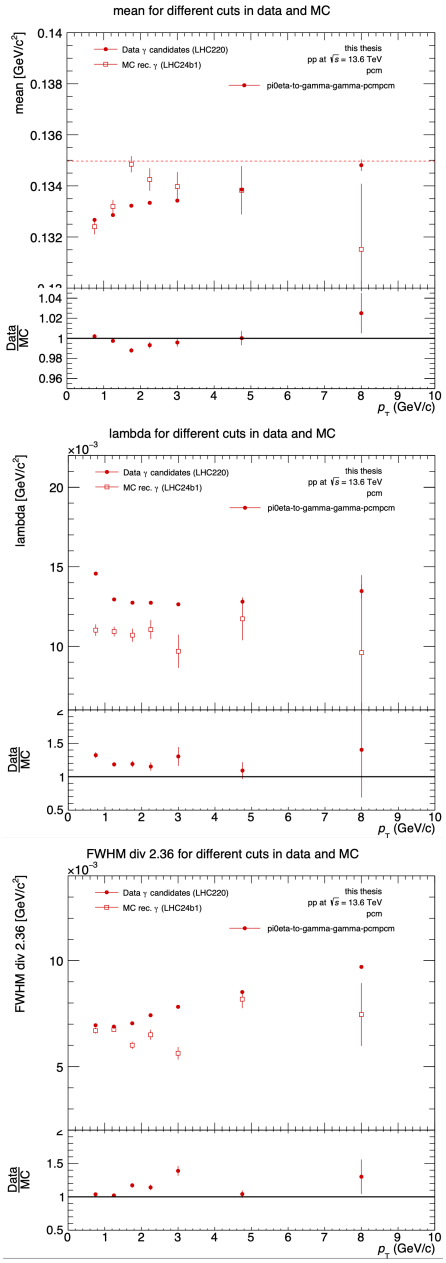

Figure 25: Comparison between the result obtained with Monte Carlo (empty squares) and with data (solid dots) of the obtained fit parameters from the asymmetric Gaussian and the given ratio between data and Monte Carlo. Upper: mean value for the asymmetric Gaussian, middle: inverse slope λ of the Bremsstrahlung tail of the fit function, lower: FWHM/2.36 of the peak of the asymmetric Gaussian.

values for data are always lower then the results from the Monte Carlo Simulation. The values seem to be systematically below the rest mass of the π^0, except for the higher p_{T} range. This observation could be reasoned by the asymmetry of the Gaussian due to the tail caused by Bremsstrahlung. As this could cause the mean to be shifted to smaller masses. When looking at the ratio between data and MC the deviation is smaller than two percent for the whole transverse momentum range.
The figure in the middle plots the inverse slope of the Bremsstrahlung tail λ as a function of the transverse momentum p_{T}. Here one would expect the values to be more or less the same, and to not depend on the transverse momentum. This can be seen for most of the points, just the first few data points at low p_{T} seem to be out of range a little bit as a slope can be seen there. Also, if one compares data to Monte Carlo a deviation of 30 % is visible. This suggests that a systematic error is still made or that some property is not yet implemented correctly in the Monte Carlo simulation. This assumption could be tested by applying a cut to not have as much Bremsstrahlung, for example by setting R $>$ 65 cm, and then checking the results for the λ parameter.
The FWHM plot in fig. 25 shall give measure to the width of the peak obtained from the fit. By combining the Gaussian with the tail caused by Bremsstrahlung, the width of the curve - which is normally given as σ from the Gaussian - is no longer delivering the complete value of the peak width. Therefore the FWHM/2.36 is used, which is no longer the same as the σ value. This is the sufficient property for the peak width in this case. However, as expected, in the plot the data points seem to have a slope. Meaning that the mass resolution gets larger the higher the transverse momentum gets. In comparison to the Monte Carlo simulation the deviations are up to 40 %.

To further work with the data and especially to calculate the invariant yield the raw yield is needed. Therefore it has to be extracted from these plots. In general, this can be achieved by subtracting the mixed event background and the remaining background estimated with the linear fit and then integrating over the invariant mass peak. For the integration range an asymmetrical range has to be chosen to make sure to account for the Bremsstrahlung. The integration limits chosen are the upper integration limit:

$$M_{\pi^0}^{up} = M_{\pi^0} + 0.02\ GeV/c^2 \tag{26}$$

$$M_{\eta}^{up} = M_{\eta} + 0.03\ GeV/c^2 \tag{27}$$

and the lower integration limit:

$$M_{\pi 0}^{low} = M_{\pi^0} - 0.035\ GeV/c^2. \tag{28}$$

$$M_{\eta}^{low} = M_{\eta} - 0.065\ GeV/c^2 \tag{29}$$

These chosen integration limits can also be seen in the invariant mass plot from fig. 23 and fig. 24 as the dark grey lines on the left and right side of the invariant mass peak. Extracting the integration range for the raw yield calculation was the main reason for doing all these fits to the invariant mass spectra.
What might catch attention is that in the plots there are no green or grey lines drawn into some of the p_{T} bins. This is the case if either there was too little statistics or too much background to make a sufficient fit. And therefore no mean was drawn into the plot.

With this the raw yield can be obtained as

$$N_{raw}^{\pi^0(\eta)} = \int_{M^{low}}^{M^{up}} (N_d - N_{comb.BG})\ dM_d - \int_{M^{low}}^{M^{up}} (B + CM_d)\ dM_d \tag{30}$$

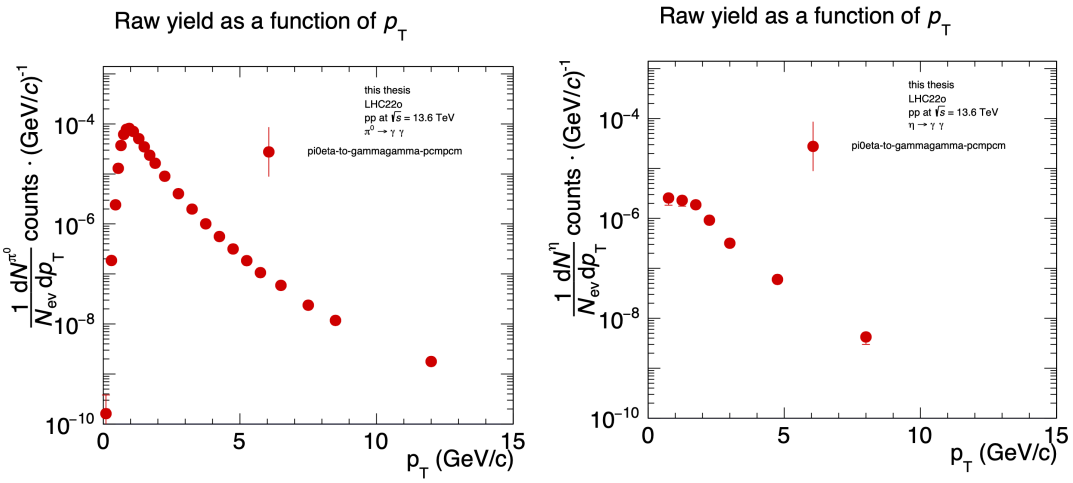

Figure 26: Extracted raw yields from the LHC22o full dataset. Left: extracted raw yield for the two γ decay mode of the π^0 meson. Right: extracted raw yield for the two γ decay mode of the η meson.

In fig. 26 the raw yield obtained in this way from data can be seen for the two γ decay mode and in fig. 27 for the Dalitz decay. In each figure the results obtained from the π^0 are shown on the left side and the results for the η meson on the right. For the Monte Carlo simulation the results can be found in the Appendix A.3.
It is noticeable that the raw yield of the π^0 meson reaches higher values for both decay modes than the η meson does. For both figures this difference is of about one order of magnitude. This could have multiple reasons. First of all the branching ratio of the two decay modes is smaller for the η meson than for the π^0 meson. The exact numbers for the branching ratios

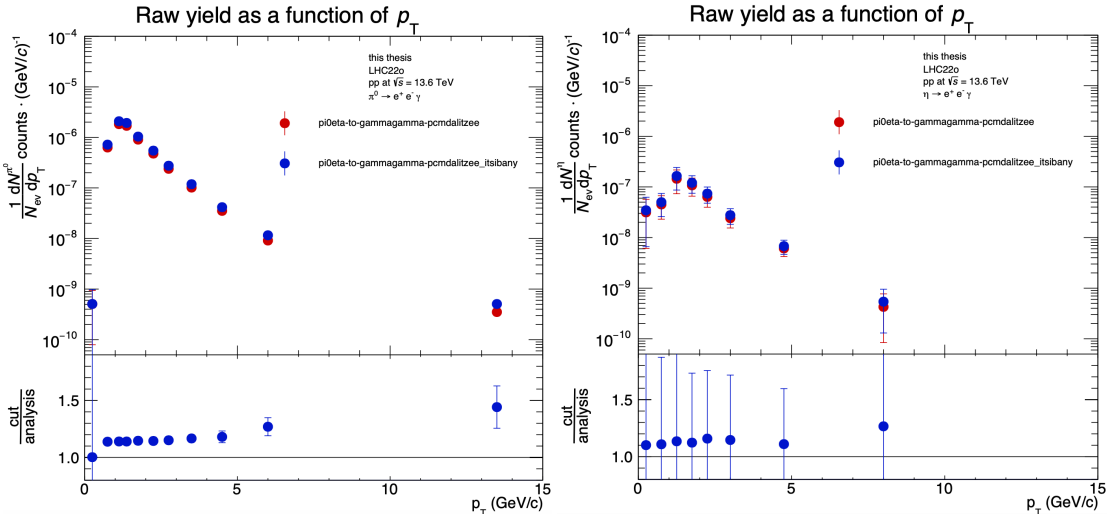

Figure 27: Extracted raw yields from the LHC22o full dataset. Left: extracted raw yield for the Dalitz decay mode of the π^0 meson. Right: extracted raw yield for the Dalitz decay mode of the η meson

can be found in table 8. And secondly the production cross section of the η meson is smaller than the production cross section for the π^0 meson. Lastly, this could also be due to a smaller efficiency of the η meson at low p_T. It shall be noted that here only the p_T bins with a sufficient fit were taken into account, as only those are able to deliver reliable results. Therefore the first bin was not accounted for in the further analysis.
When looking at the two different cuts that were used for the Dalitz decay mode, a very similar course of the curve can be seen. But the data points for the cut, which considers any Inner Barrel ITS hit, are consistently a little bit higher. This behaviour increases the higher the transverse momentum gets. Especially for the π^0 meson one can observe this more clearly as there it was possible to achieve more data points by choosing a smaller binning. Nevertheless one can clearly see a similar shape in all of the raw yield plots consisting of a very steep rise of the curve at low p_T and then a more shallow drop after reaching the peak.

6.2 Corrections on the neutral meson

In this subsection the goal is to extract the acceptance and reconstruction efficiency to be able to calculate the corrected yields of the neutral mesons. As the Monte Carlo simulation of the used data set had very little statistics, especially concerning the Dalitz decay of the η meson, all of the analysis in this section will be made for both decay modes of the π^0 meson and only for the two γ decay of the η meson.

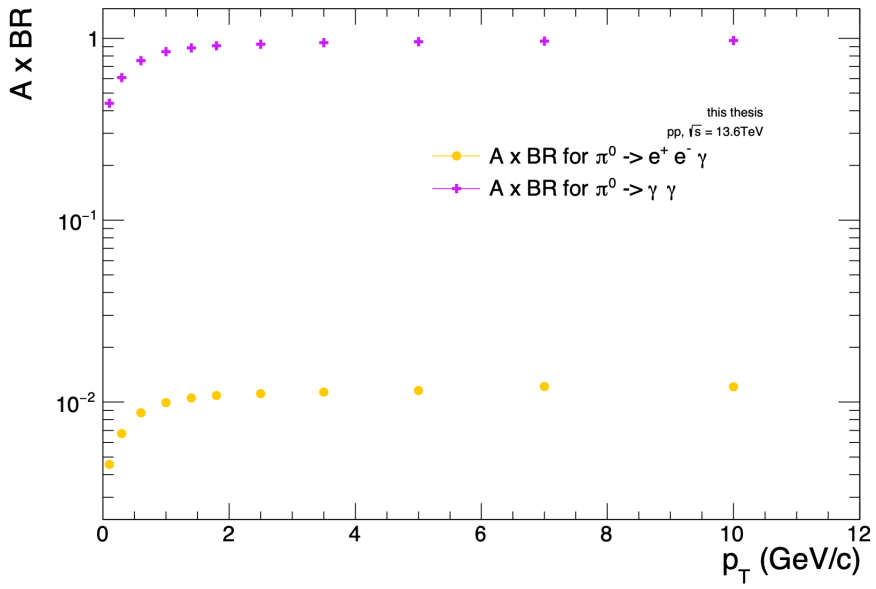

Figure 28: Geometrical acceptance $A_{\pi^0}(p_T)$ for the two γ decay (violet) and the Dalitz decay (orange) as well as the calculated ratio between the two decay modes (lower) for the data set LHC22o pass6 small

The geometrical acceptance of a detector can be calculated by dividing the number of primary mesons that appear inside the fiducial region - and have daughter particles which are also inside the fiducial acceptance - by the number of all primary mesons generated inside the fiducial region.

$$A_{\pi^0(\eta)}(p_T) \cdot BR = \frac{N^{daughters\ in\ acceptance}_{\pi^0(\eta)}(p_T)}{N^{all}_{\pi^0(\eta)}(p_T)}\Bigg|_{|y|<y_{max}} \tag{31}$$

In fig. 28 the geometrical acceptance can be seen for both decay modes [3].
As one would expect the acceptance for the Dalitz has its plateau at approximately one percent and the acceptance for the two γ decay at approximately 99 percent. The reason for this originates from the different branching ratios of the two decay modes. Given the definition of the acceptance in eq. 31, the geometrical acceptance should have its plateau region exactly at the value of the branching ratio. So speaking for the π^0 meson at 0.988 for the two γ decay mode and at 0.012 for the Dalitz decay mode.

To further correct the data it is necessary to take a look at the reconstruction efficiency of

[3] It shall be noted, that for this plot the small data set, which is listed in table 4, was used because the needed data for the daughters in acceptance was not available for the full data set.

the two decay modes. The efficiency is given as

$$\varepsilon_{\pi^0(\eta)}(p_T) = \frac{N^{validated}_{\pi^0(\eta)}(p_T)}{N^{daughters\ in\ acceptance}_{\pi^0(\eta)}(p_T)}\Bigg|_{|y|<y_{max}}. \tag{32}$$

Here the numerator is the number of mesons that were reconstructed and matched with the MC simulation truth. The denominator of the reconstruction efficiency is the number of particles by which both the mother and the daughter particles are within the fiducial acceptance.

When looking at equation 31 and equation 32 one can remark that the numerator of the geometrical acceptance is the same as the denominator of the reconstruction efficiency. That is why it often makes sense to take a look at the product of these two components

$$\varepsilon_{\pi^0(\eta)} \cdot A_{\pi^0(\eta)} \cdot BR = \frac{N^{validated}_{\pi^0(\eta)}(p_T)}{N^{all}_{\pi^0(\eta)}(p_T)}\Bigg|_{|y|<y_{max}} \tag{33}$$

As the histogram of the daughters in acceptance was no longer needed for this purpose, this analysis was again done for the full data set. The results for the product of efficiency and acceptance for the full dataset can be seen in fig. 29. In the figure the result for the two γ decay mode is plotted in comparison to the Dalitz decay as well as the ratio between the two. When now comparing the values these curves reach it appears that the two differ more for lower p_{T} ranges. For higher transverse momentum they differ by about one order of magnitude. The observed higher deviation for lower transverse momenta can be reasoned by the applied selection criteria to cut out pions for the dilepton criteria in table 3. As the pion Bethe Bloch curve intersects the electron curve, some e^+ and e^- are left out in the lower p_{T} range for the Dalitz decay due to this cut. For higher p_{T} values the difference between the two decay modes reaches a factor of 10. As the efficiency of the two decay modes can be calculated with

$$\varepsilon^{\gamma\gamma}_{\pi^0(\eta)} = (CP \cdot \varepsilon^{e^+e^-}_{\gamma})^2 \cdot BR(\gamma\gamma) \tag{34}$$

$$\varepsilon^{e^+e^-\gamma}_{\pi^0(\eta)} = \varepsilon_{e^+} \cdot \varepsilon_{e^-} \cdot CP \cdot \varepsilon^{e^+e^-}_{\gamma} \cdot BR(e^+e^-\gamma), \tag{35}$$

the ratio of the efficiencies between the two γ and the Dalitz decay mode can be approximated with the conversion probability (CP) divided by the branching ratio of the Dalitz decay, which is about 0.01. Since the conversion probability is around 0.1 this observation for high transverse momenta is expected to be around one order of magnitude as visible in fig. 29.

A comparative analysis of the product of efficiency, acceptance and branching ratio at $\sqrt{s} = 13.0$ TeV and $\sqrt{s} = 13.6$ TeV is presented in fig. 30. In general one can observe that even though the two curves follow the same shape, one can clearly tell that this quantity is

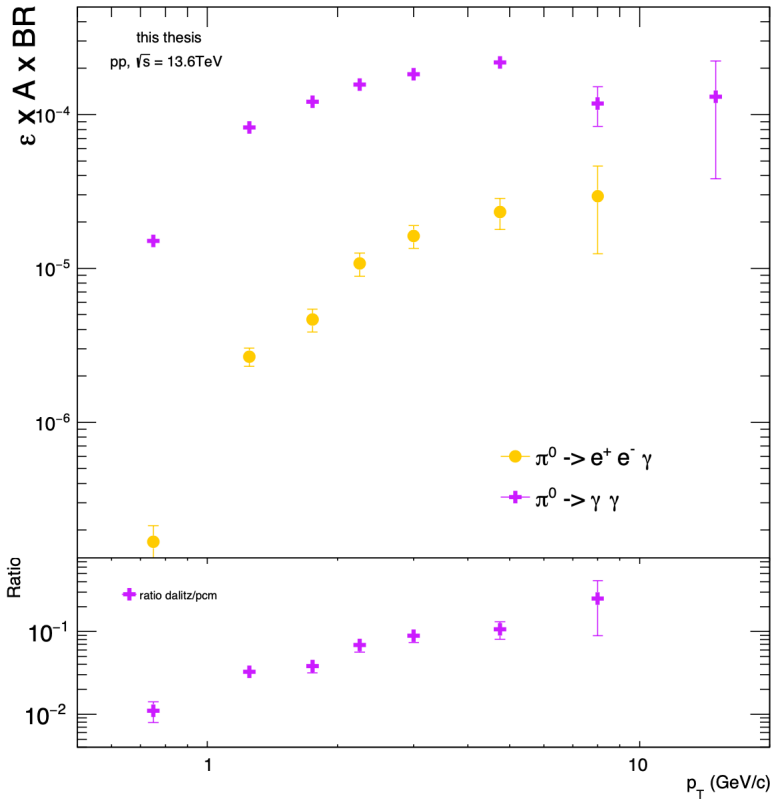

Figure 29: product of the reconstruction efficiency, the geometrical acceptance and the branching ratio for the used cuts. Upper: results for this product for the two γ decay mode of the π^0, lower: results for this product for the Dalitz decay mode of the π^0.

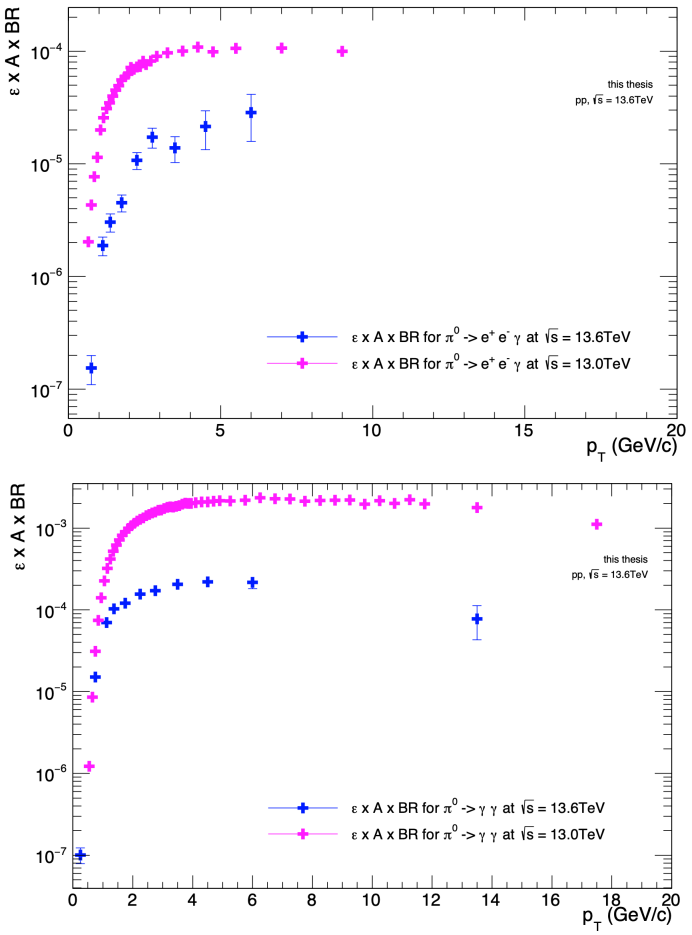

Figure 30: Comparison of the result for efficiency times acceptance times branching ratio at $\sqrt{s} = 13.0$ TeV (pink) and at $\sqrt{s} = 13.6$ TeV (blue). Top: comparison for the Dalitz decay mode. Bottom: comparison for the two γ decay mode.

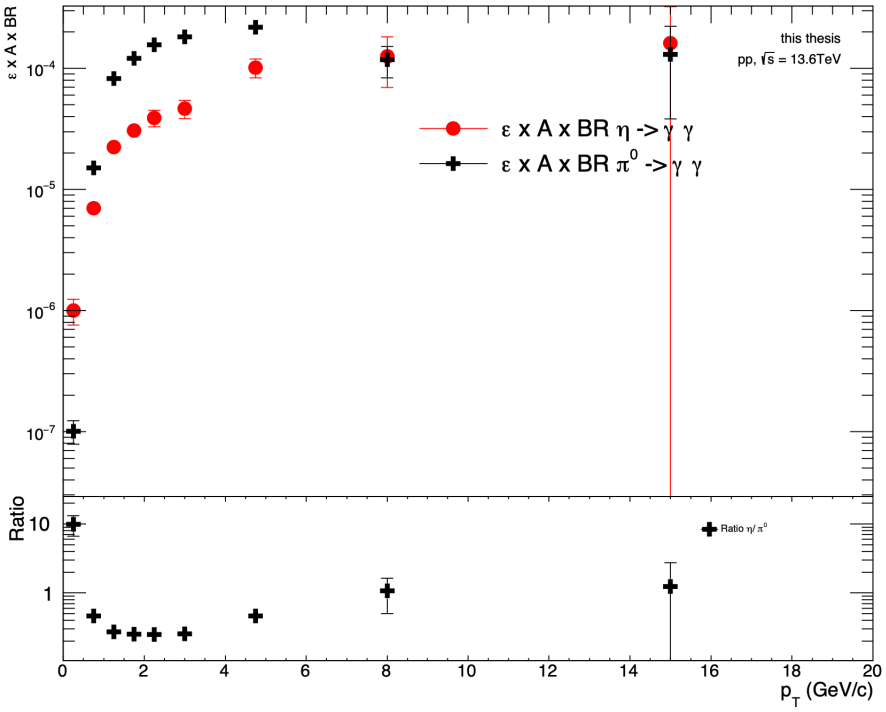

Figure 31: Comparison of the product of efficiency, acceptance and branching ratio for the π^0 meson and the η meson for the two γ decay channel

significantly lower for Run 3 than for Run 2. For both decay modes there is a difference at higher p_{T} ranges of about one order of magnitude. As the efficiency achieved in Run 3 is already known to be lower than in Run 2 this result is just another proof for this observation and this was expected.

In the final step of analysing the product of efficiency, acceptance and branching ratio one can also compare the two mesons. Therefore fig. 31 shows the results for the two γ decay mode for the π^0 meson in black and the results for the η meson in red. Here one can observe a deviation between these curves that decreases the higher the transverse momentum gets. For low p_{T} the ratio between the two curves has a high value of approximately 10.

One more remark shall be made concerning the error calculation used in this thesis. Here Gaussian error propagation was used, although it is known to have some defects [38]. Therefore a comparison with the TEfficiency was made using the statistical option "kFCP" as recommended by the PDG ([39]). The corresponding plots can be found in the Appendix (A.4.2, A.4.4) where the results of this comparison of the error bars are shown. With this method one obtains asymmetric errors. For the further analysis process asymmetric errors are difficult to

work with. Since the errors which are obtained for the Gaussian error propagation are in the same order of magnitude, this thesis will go on with the errors obtained with Gaussian error propagation. Nevertheless it would be important to make this comparison once again as soon as more statistics are available for the Monte Carlo Simulation.

As the two main components, the geometrical acceptance and the reconstruction efficiency, are calculated by now, it is possible to have a look at the fully corrected invariant yield of the mesons.

$$E\frac{d^3N}{dp^3} = \frac{1}{2\pi}\frac{1}{p_T}\frac{d^2N}{dydp_T} = \frac{1}{2\pi N_{ev}}\frac{1}{\varepsilon_{\pi^0(\eta)}A_{\pi^0(\eta)}BR}\frac{1}{p_T}\frac{N_{raw}^{\pi^0(\eta)}}{\Delta y \Delta p_T}, \tag{36}$$

where N_{ev} stands for the number of events, p_T stands for the transverse momentum, $N_{raw}^{\pi^0(\eta)}$ for the raw yield derived from the data, Δy is the rapidity range and Δp_T is the bin width of each p_{T} bin.

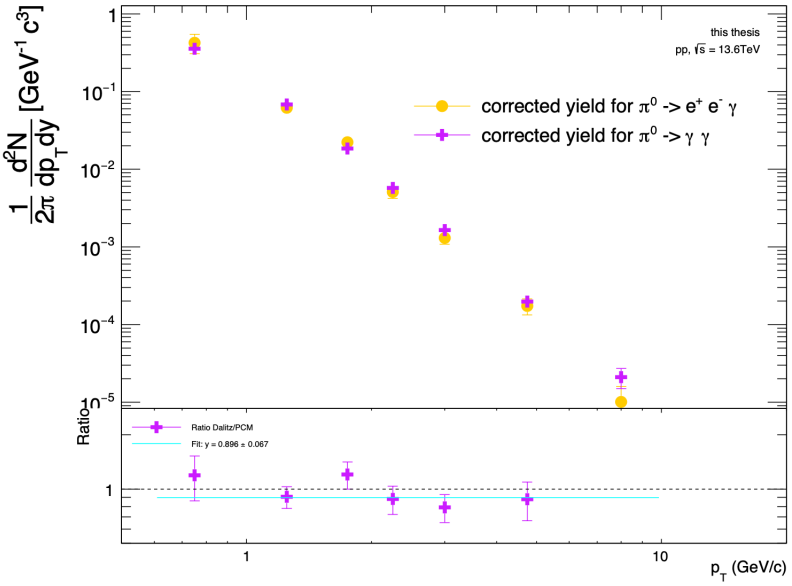

Figure 32: Corrected yield $\frac{1}{2\pi}\frac{d^2N}{dp_T dy}$ for the π^0 meson reconstructed using the Dalitz decay mode (orange) and the two γ decay mode (violet) as well as the ratio between the two decay modes for the π^0 meson

Let´s take a look at the results for the data set LHC22o which can be seen in fig. 32. There the results for the corrected yield are plotted for the Dalitz and the two γ decay mode for the π^0 meson as well as the ratio between them. The same plot can also be found for the η meson in the Appendix A.4.3. If it was an optimal run, the corrected yield obtained with the two γ decay mode is expected to be the same as the corrected yield obtained with the Dalitz decay,

so that the ratio of the two modes would be one. In the case of the derived plots for this thesis, one can clearly see that the two curves follow the same shape and they are in the same order of magnitude as well.
As already mentioned in the motivation of this thesis, it is of great importance to compare the two decay modes with each other. Therefore the ratio of the two decay channels was added to fig. 32 and a polynomial of the order zero was fitted to the ratio points. It seems that there is no clear systematic trend of the ratio. Some of the points are above and some points are below one, and the ratio fluctuates from 0.6 up to values of approximately 1.1. But as the fitted line is located at 0.882 ± 0.065 the corrected yield of the two γ decay slightly tends to be of a higher value than the corrected yield of the Dalitz decay.

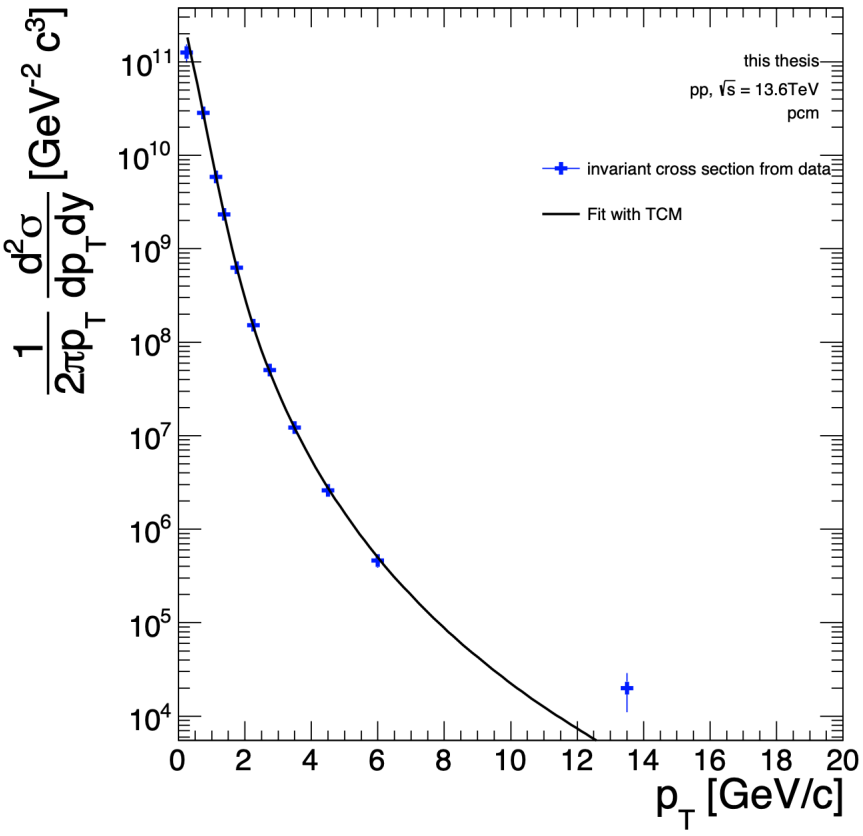

Figure 33: Result of the Two-Component Model for the π^0 meson. The differential invariant cross section and the result of the fit for the two γ decay can be seen.

The data points of the corrected yield can additionally be fitted with the so called Two-

Component Model (TCM) [40]. This model has been modified to suit the obtained results.

$$\frac{1}{2\pi p_T}\frac{d^2\sigma}{dp_T dy} = A_e exp\left(-\frac{\sqrt{p_T^2+M^2}-M}{T_e}\right) + A\left(1+\frac{p_T^2}{T^2 n}\right)^{-n} \tag{37}$$

where $\frac{1}{2\pi p_T}\frac{d^2\sigma}{dp_T dy}$ is the differential invariant cross section which can be obtained from the corrected yield by multiplying by the factor $\sigma_{FT0} = 59.4 \cdot 10^{-3}$ barn [41]. The other variables in this equation are the meson mass in GeV/c^2 and the fitting variables A_e and A which are normalization factors given in $GeV^{-2}c^3$, the inverse slope parameters T_e and T and finally n which is the power law order. The plot obtained after applying this fit to the data points of the differential invariant cross section of the two γ decay can be seen in fig. 33. The function seems to be a good fit for the data points at low p_{T}. But at higher transverse momentum ranges one can see some deviations as the fit function is too low to fit all of the data points. In order to make a qualitative statement about this, the fit parameters must be analysed.

Collision Energy (TeV)	13	13.6
A_e $\left(\frac{pbarn\cdot c^3}{GeV^2}\right)$	$(427 \pm 49) \cdot 10^9$	$(366.00 \pm 0.16) \cdot 10^9$
T_e (GeV)	0.157 ± 0.007	0.2084 ± 0.0006
A $\left(\frac{pbarn\cdot c^3}{GeV^2}\right)$	$(26 \pm 2) \cdot 10^9$	$(40.50 \pm 0.07) \cdot 10^9$
T (GeV)	0.65 ± 0.01	0.49 ± 0.004
n	2.96 ± 0.01	2.82 ± 0.024
m	0.30 ± 0.05	-

Table 10: Parameters of the TCM parametrisation for the π^0 meson in Run 2 ([40]) and Run 3 for the two γ decay.

To categorize the values of the fit parameters, the same fit was applied to the corrected yield from the previous run of ALICE at a collision energy of 13.0 TeV. The fit parameters from this fit and the fit parameters obtained for Run 3 are listed in table 10. In this table the results for the two γ decay are shown, but the fit was also applied to the Dalitz decay. The results for this as well as a list of the fit parameters can be found in the Appendix A.4.1.

First thing to be noted when comparing the results for the fit parameters is that there is one additional fit parameter m for the fit at $\sqrt{s} = 13$ TeV. This is because the fit function from Run 2

$$E\frac{d^3\sigma}{dp^3} = A_e exp\left(-\frac{\sqrt{p_T^2+M^2}-M}{T_e}\right) + A\left(1+\frac{p_T^2}{T^2 n}\right)^{-n-mp_T} \tag{38}$$

has an additional term that is linear with the transverse momentum to account for a deviation of the π^0 from the fit function in equation 37 for very high p_{T}. This term was left out for the

fit of Run 3 data because reliable statistics were only available for low and middle ranges of p_{T} for this thesis. Therefore this fit parameter will not be discussed any further.
Apart from that, one can see that even though the fit parameters vary all of them are in the same order of magnitude for Run 2 compared to Run 3. This is what would be expected, as in general the differential invariant cross section measured for a meson should not differ widely for such a change in the collision energy. However, as some changes concerning the used detectors and the cuts that were applied to the particles were made, small deviations may appear. In general the first component of the sum in equation 37 is responsible for the fit in low transverse momentum range and the second component is in charge of the higher p_{T} range. As can be seen in fig. 33 the TCM fits very good in low p_{T} and therefore the normalisation factors for A_e agree within the errors between the results obtained for $\sqrt{s} = 13.0$ TeV and $\sqrt{s} = 13.6$ TeV. When taking a look at the normalisation factors A_e and A, one can notice that the normalisation factor is always larger for higher collision energy. For higher p_{T} the fit gets worse and consequently also the normalisation factor A is not as similar between the two runs. Besides that the temperature parameters T_e and T also differ in comparison with Run 2. For the low p_{T} the result from Run 3 is of a higher value whereas the result for the low p_{T} is of a smaller value for the temperature parameter. And lastly the power law order of the TCM fit for 13.6 TeV is slightly smaller than for Run 2. To get a more precise statement more Monte Carlo statistics especially in higher p_{T} ranges would be helpful. Also only PCM measurements were taken into account and it could be useful to combine them with the measurements from the calorimeter. For now there is still a lot to be understood to be able to find a better explanation for these deviations. The only reason that could interpret the deviations between the fit parameters is that the values for the collision energy of 13 TeV were taken from a paper ([40]) which already includes statistical and systematic errors and the combination of different detectors. For this thesis no systematic, but only statistical uncertainties were incorporated.

6.3 Comparison of the corrected yield

In order to get a better impression of the results of this analysis, some comparisons will be drawn in this section. The first goal is to compare the corrected yield to a PYTHIA 8 simulation ([42]) and then all of the quantities will be compared to the results from Run 2 at a collision energy of $\sqrt{s} = 13.0$ TeV like already done for the TCM fit.

The results of the comparison to the model predicition of PYTHIA 8 can be seen in fig. 34. The PYTHIA curve shall give a theoretical estimate of what the result is expected to look like based on this event generator. This model is less of a perfect measure of how the curve has to look and more of another prediction for comparing the results to get an impression of how good the implementation has worked. Fig. 34 shows the two resulting plots where the curve predicted by PYTHIA 8 is green and the points obtained from data are blue. For the two γ decay one can see a good match of the data points to the PYTHIA 8 prediction for low

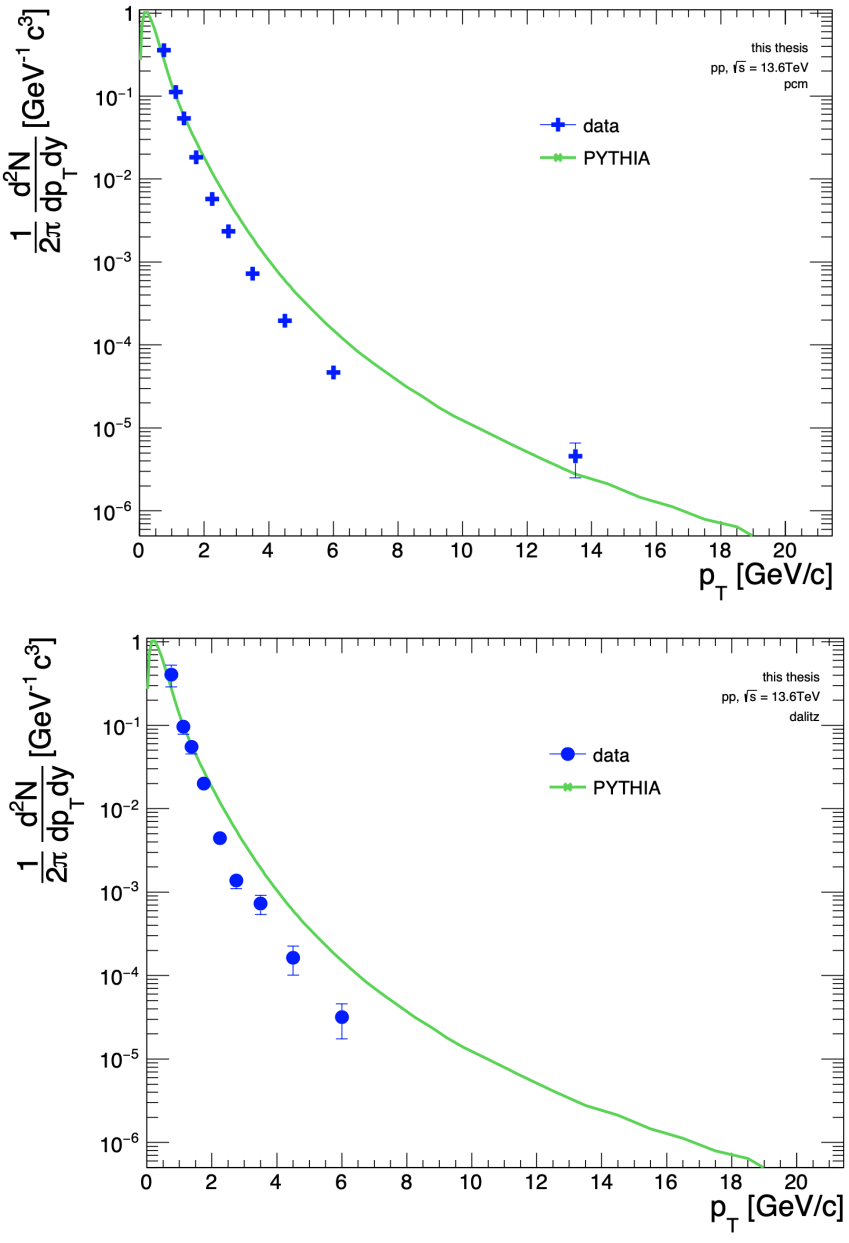

Figure 34: Comparison of the corrected yield obtained from data (blue) and the theoretical PYTHIA curve (green). Top: comparison for the two γ decay mode. Bottom: comparison for the Dalitz decay mode

transverse momenta. For higher p_{T} ranges the PYTHIA curve is always above the data points. The same effect can also be observed for the Dalitz decay mode. There, the agreement with the PYTHIA prediction is also best at low p_{T} between zero and three GeV/c. In the paper draft for the results for Run 2 at a collision energy of $\sqrt{s} = 13$ TeV, the PYTHIA 8 prediction is also above the data points, the only difference to the results from this thesis is that there no p_{T} dependence was observed.

To further estimate the data used in this analysis it can be useful to compare the results at $\sqrt{s} = 13.6$ TeV with the results from the last ALICE Run 2 at $\sqrt{s} = 13$ TeV. For this the almost published data from the ALICE Collaboration was used.

Finally one can take a look at the invariant yields from the two runs. Fig. 35 shows the comparison between them. One would expect the invariant yield at $\sqrt{s} = 13.6$ TeV to be overall larger than the invariant yield at $\sqrt{s} = 13$ TeV. This difference is expected to increase with p_{T}, so that at low p_{T} approximately a constant factor can be observed and this difference increases from there on. When taking a look at fig. 35 one can notice that here we observe that the curve at $\sqrt{s} = 13$ TeV is higher than the curve for Run 3 for intermediate to high p_{T}. At low transverse momenta the curves seem to agree and for the two γ decay mode it even looks as if the curve for Run 3 is slightly higher. But the higher the transverse momentum gets, the higher also gets the deviation between the two curves. Contrary to what was expected the curve for the collision energy $\sqrt{s} = 13$ TeV is higher than the curve for the collision energy of $\sqrt{s} = 13.6$ TeV. No explanation has yet been found for this behaviour. As the PYTHIA 8 model also predicted higher values for the corrected yield at the same p_{T} range this behaviour should be analysed further. This problem can probably be better understood by varying all the cuts and checking whether one cut is the source of the deviation. It would also be important to get more Monte Carlo statistics to obtain better results.

In fig. 36 the ratio between the invariant yield of the η meson and the invariant yield of π^0 meson are plotted as a function of the transverse momentum range. Here again in blue the results from a collision energy of $\sqrt{s} = 13.6$ TeV can be seen compared to the results obtained at a collision energy of $\sqrt{s} = 13$ TeV in pink. The first thing that is noticed are the large error bars of the ratio obtained from Run 3 data. The main reason for this is a lack of Monte Carlo statistics that has already been mentioned before in this analysis. Apart from that one can see that the trend from Run 2 is overall followed for $\sqrt{s} = 13.6$ TeV. The order of magnitude as well as the shape of the curve look similar at both energies.

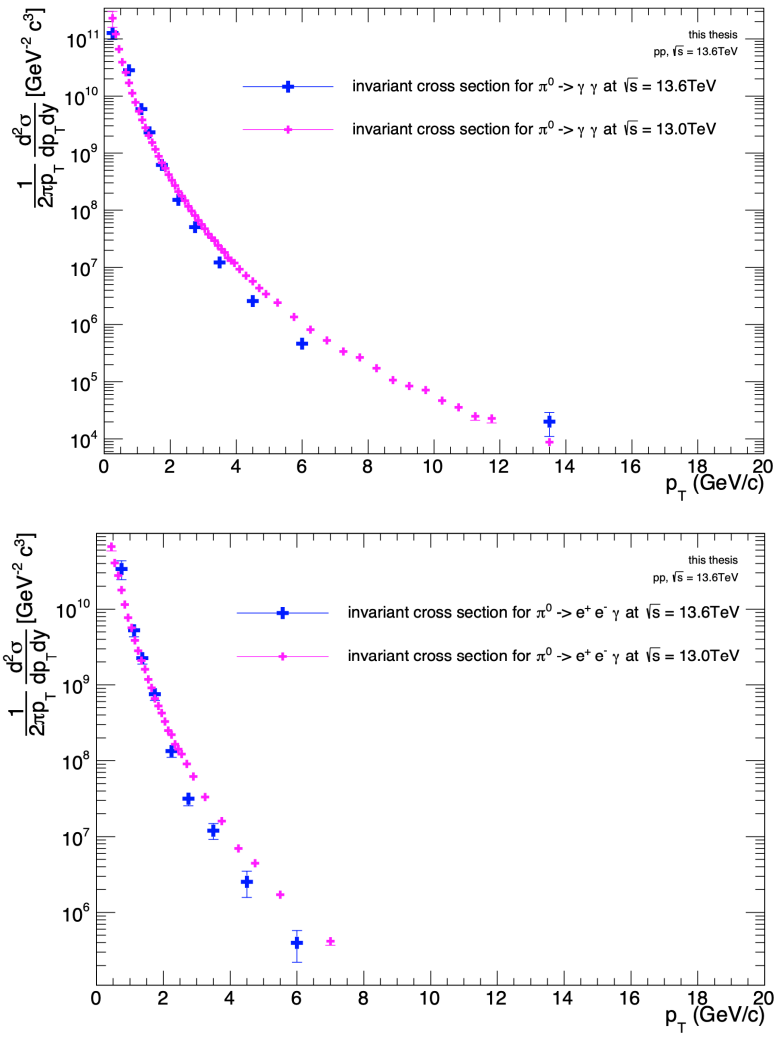

Figure 35: Comparison of the result for the invariant yield at $\sqrt{s} = 13.0$ TeV (pink) and at $\sqrt{s} = 13.6$ TeV (blue). Top: Comparison of the two γ decay mode. Bottom: Comparison of the Dalitz decay mode.

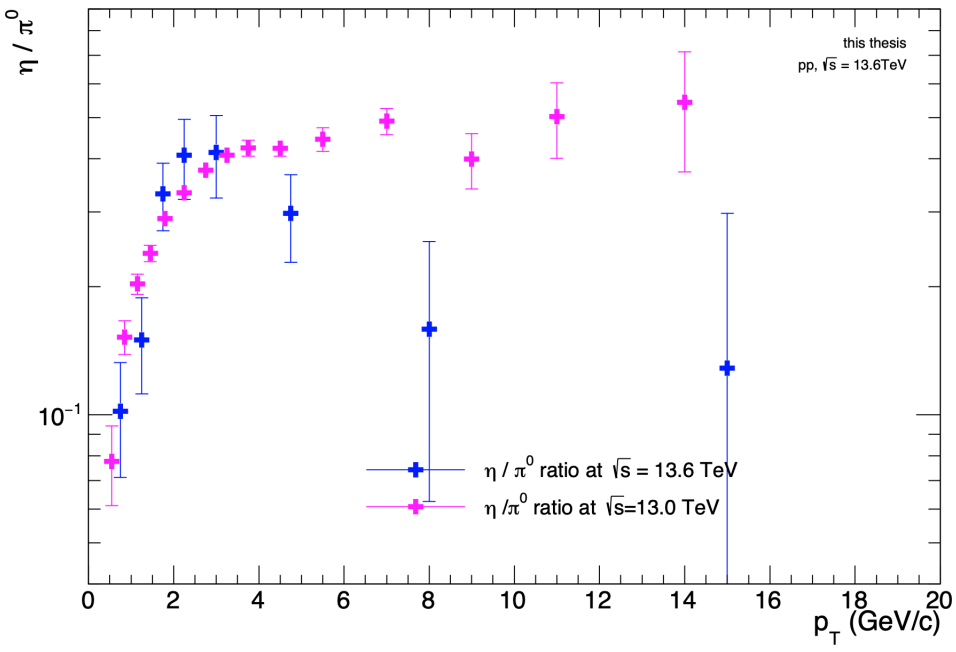

Figure 36: Ratio of the invariant yield of the η meson and the π^0 meson for the two γ decay channel. In pink the results for this ratio can be seen for Run 2 and in blue the results for Run 3

7 Conclusion and Outlook

For this thesis measurements of the differential invariant yields of the π^0 and η mesons were performed using the two main decay channels in pp-collisions at $\sqrt{s} = 13.6$ TeV. To achieve that, a detailed analysis of the invariant mass of the π^0 and the η meson was performed. The invariant mass spectra in p_{T} intervals were fitted with an asymmetric Gaussian and by integrating over the obtained peak the raw yield was obtained. Furthermore, corrections in terms of efficiency and acceptance were made on the data and with that the differential cross section of both mesons was received. As the whole analysis was executed on two decay modes this thesis also provided a comparison between the two modes. Also a first η/π^0 ratio was calculated at the collision energy of $\sqrt{s} = 13.6$ TeV. Additionally, a comparison between the results of Run 2 and Run 3 was performed.

During the analysis of the invariant mass it was found that the used fit function - the asymmetric Gaussian - worked well to compensate for the Bremsstrahlung-tail. From these fits it was then possible to obtain a reasonable integration and transverse momentum range and with that the raw yield got calculated. For the corrections that were performed on the raw yields, it has already been known that the efficiency for Run 3 was smaller than the efficiency which was reached in Run 2. This expectation showed in the comparison of the products of efficiency, acceptance and branching ratio. There the result for Run 3 was around one order of magnitude smaller than the result for Run 2 at $\sqrt{s} = 13$ TeV. For the corrected yield it is visible that the Dalitz decay and the two γ decay have a conformity of 0.882 ± 0.065 for the reconstruction of the π^0 meson. For the reconstruction of the η meson the agreement between the two decay modes is 0.923 ± 0.286. These values are a satisfying consensus especially regarding the available Monte Carlo statistics.
The outcome of the invariant yield compared to the model predictions of PYTHIA 8 showed that a good agreement in low transverse momentum ranges was reached. At higher p_{T} the PYTHIA model predicted values were too high compared to the values obtained from the data of Run 3. This behaviour was also observed for Run 2 of ALICE and therefore is no surprise. In a further comparison with said results from Run 2, it was shown that at higher collision energy the invariant yield matches for the lower p_{T} range and reaches lower values for higher transverse momenta. As this behaviour has been noticed for the PYTHIA prediction as well, systematic studies should be done at high p_{T} to understand if the data were properly measured or if something should be changed. When taking a look at the results obtained at different collision energies in the past, it is noticeable that the invariant yield gets larger the higher the collision energy is. And that the deviation is larger the higher the transverse momentum is.
This thesis also provides a first ratio between the invariant yields of the two mesons the η and π^0. Here it is visible that the curve for Run 2 matches with the result obtained for Run 3

especially at low transverse momentum. At higher p_{T} the ratio at $\sqrt{s} = 13.6$ TeV was slightly smaller but the current statistical uncertainties do not allow to draw any conclusion.

7.1 Outlook

Even though this thesis was able to provide first steps in the analysis of neutral mesons at $\sqrt{s} = 13.6$ TeV there are still many things to do to complete this analysis. As mentioned multiple times during the analysis, the statistics that were available especially for the Monte Carlo Simulation were not satisfying. To make a more detailed statement and to check the results obtained in this thesis for a smaller binning and at higher transverse momentum more Monte Carlo statistics are crucial. This has already been initiated and the new Monte Carlo set is on its way. However, the implementation of this new set is not in the time frame of this thesis.

Another important step to complete the analysis is to take systematic uncertainties into account. This can be done by varying the used cuts. Especially the dE/dx cut to exclude pions in the dilepton cuts in table 3 should be changed, as this cut wastes a lot of efficiency for the reconstruction in the Dalitz decay channel. The reason for this is that the Bethe-Bloch curve of the pions intersects the curve of the electrons. When now cutting out the σ range around the pions many electrons get lost. This is a pity and could be changed to make place for better results.

Finally, it shall be mentioned that the material budget weights have not yet been calculated for this data set and this version of the V^0-finder and are not yet implemented in the analysis. This should also be a next step to check the material implementation and calibrate the detector.

In conclusion this thesis started off the analysis of neutral mesons in ALICE Run 3 at $\sqrt{s} = 13.6$ TeV. By using the $\gamma\gamma$ and the Dalitz decay modes the reconstruction of the π^0 and η meson was performed. Even though there are still some important things left to do until the analysis is complete, the python scripts developed for this thesis and the analysis done will help with the further analysis process.

References

[1] *Geant4*. URL: https://geant4.web.cern.ch.

[2] Felix Schlepper. *Svertexer with tpc-only tracks*. 2023. URL: https://indico.cern.ch/event/1351889/contributions/5696031/attachments/%202762206/4810535/291123.pdf.

[3] CERN webpage. *The Standard Model*. URL: https://home.cern/science/physics/standard-model. (accessed: 15.04.2024).

[4] Ulrich Uwer. "Vorlesungsskript: Experimentalphysik 4 -". In: (2023), pp. 891–921.

[5] Peter Braun-Munzinger and Johanna Stachel. "The quest for the quark–gluon plasma". In: *Nature* 448(7151).302-309 (2007). DOI: 10.1038/nature06080.

[6] CERN. *Heavy ions and quark-gluon plasma*. URL: https://www.home.cern/science/physics/heavy-ions-and-quark-gluon-plasma. (accessed: 16.04.2024).

[7] ALICE Collaboration. "The ALICE experiment: A journey through QCD". In: CERN-EP-2022-227 (2022). DOI: https://doi.org/10.48550/arXiv.2211.04384.

[8] Fabio Sauli. *Interaction of photons and neutrons with matter. In Gaseous Radiation De tectors: Fundamentals and Applications*. Cambridge University Press, 2014.

[9] Wolfgang Demtröder. *Experimentalphysik 4. Kern-, Teilchen- und As- trophysik*. Springer-Verlag GmbH Berlin Heidelberg, 2017. ISBN: 978- 3-662-52883-9.

[10] Silvia Masciocci. *Detectors for particle tracking and identification*. URL: https:%20//www.physi.uniheidelberg.de/~sma/teaching/GraduateDays2017/sma_Detectors_1_InteractionsWithMatter.pdf. (accessed: 26.04.2024).

[11] Christian Sonnabend. *ALICE TPC dE/dx performance*.

[12] Prof. Dr. Johanna Stachel. "Detectors in Nuclear and Particle Physics". In: (2018). URL: https://www.physi.uni-heidelberg.de/~fschney/detektoren/detector_all.pdf.

[13] ALICE Collaboration. "The ALICE Transition Radiation Detector: Construction, operation, and performance". In: *Elsevier* (2018). DOI: https://www.sciencedirect.com/science/article/pii/S0168900217309981.

[14] *The Large Hadron Collider*. URL: https://home.cern/science/accelerators/large-hadron-collider. (accessed: 10.05.2024).

[15] *The CERN accelerator complex, layout in 2022 Complexe des accélérateurs du CERN en janvier 2022*. URL: https://cds.cern.ch/record/2800984/files/CCC-v2022.png. (accessed: 13.05.2024).

[16] *ALICE*. URL: https://home.cern/science/experiments/alice. (accessed: 10.05.2024).

[17] ALICE Collaboration. "ALICE upgrades during the LHC Long Shutdown 2". In: *CERN-EP-2023-009* (2023). URL: https://arxiv.org/pdf/2302.01238.

[18] *ALICE ITS*. URL: https://alice-collaboration.web.cern.ch/menu_proj_items/its. (accessed: 10.05.2024).

[19] ALICE Collaboration. "Letter of Intend for A Large Ion Collider Experiment". In: (1933). DOI: https://cds.cern.ch/record/290825/files/SC00000003.pdf.

[20] on behalf of the ALICE Collaboration F.Reidt. "Upgrade of the ALICE ITS detector". In: *Elsevier* (2023). DOI: https://arxiv.org/abs/2111.08301.

[21] Panos Charotos. *The ALICE ITS upgrade: Pixels for quarks*. 2019. URL: https://ep-news.web.cern.ch/content/alice-its-upgrade-pixels-quarks. (accessed: 10.05.2024).

[22] B Abelev et al and (The ALICE Collaboration). "Technical Design Report for the Upgrade of the ALICE Inner Tracking System". In: *Journal of Physics G: Nuclear and Particle Physics* (2014). DOI: https://cds.cern.ch/record/1625842?ln=de.

[23] ALICE TPC collaboration et al. "The upgrade of the ALICE TPC with GEMs and continuous readout". In: *Journal of Instrumentation* (2021). DOI: https://iopscience.iop.org/article/10.1088/1748-0221/16/03/P03022.

[24] *ALICE TPC*. URL: https://alice-collaboration.web.cern.ch/menu_proj_items/tpc. (accessed: 10.05.2024).

[25] *ALICE TRD-Introduction*. URL: http://www-alice.gsi.de/trd/intro.html. (accessed: 14.05.2024).

[26] Johannes Stiller. *Working principle of the ALICE Transition Radiation Detector*. URL: http://www-alice.gsi.de/trd/WorkingPrincipleOfTheALICETRD.gif. (accessed: 14.05.2024).

[27] ALICE TOF Group. "Particle identification with the ALICE TOF detector at very high particle multiplicity". In: (2003). URL: https://www.fisica.unisa.it/antonio.dibartolomeo/Pubblicazioni/Alice/EPJ-C32(s02,s165-s177)2004.pdf.

[28] ALICE Collaboration. "Technical Design Report of the Time of Flight System (TOF)". In: (2000). URL: https://cds.cern.ch/record/430132/files/alice_toftdr.pdf.

[29] *ALICE TOF*. URL: https://alice-collaboration.web.cern.ch/node/34978. (accessed: 14.05.2024).

[30] Roger Forty. *Time-of-flight technologies*. URL: https://indico.cern.ch/event/999817/contributions/4253048/attachments/2240084/3797788/TOF%20technologies.pdf. (accessed: 14.05.2024).

[31] *ALICE FIT*. URL: https://alice-collaboration.web.cern.ch/menu_proj_items/FIT. (accessed: 23.06.2024).

[32] ALICE Collaboration. "ALICE: Physics Performance Report, Volume II". In: *iop* (2006). DOI: 10.1088/0954-3899/32/10/001. URL: https://iopscience.iop.org/article/10.1088/0954-3899/32/10/001.

[33] Alica Marie Endrich (Bachelor thesis). *Performance study on photon measurements using the Photon Conversion Method with ALICE in Run 3*. 2024.

[34] Alica Marie Endrich. *AlicePCMRun3-main*.

[35] *AlicePCMRun3-main*. URL: https://github.com/juliaschlaegel/AlicePCMRun3-main.

[36] Particle Data Group. *The Review of Particle Physics (2024)*. URL: https://pdg.lbl.gov/2024/tables/contents_tables.html. (accessed: 08.07.2024).

[37] ALICE Collaboration. "Analysis Note: Neutral meson production in pp collisions at s = 5.02 TeV using the Dalitz decay channel (PCM-)". In: (2019).

[38] Marc Paterno. "Calculating Efficiencies and Their Uncertainties". In: (2004). URL: https://inspirehep.net/files/57287ac8e45a976ab423f3dd456af694.

[39] *TEfficiency Class Reference*. URL: https://root.cern.ch/doc/master/classTEfficiency.html. (accessed: 10.07.2024).

[40] ALICE Collaboration. "Light neutral meson production in pp collisions at $\sqrt{s} = 13$ TeV". In: ().

[41] Y. Zang et al. "Inclusive J/ cross sections in pp collisions in s = 13.6 TeV at midrapidity with Run 3 data". In: (2024). URL: https://alice-notes.web.cern.ch/system/files?file=notes/analysis/1532/2024-05-15-Inclusive_Jpsi_cross_section_of_pp_collisions_at_13_6_TeV.pdf.

[42] C.Bierlich et al. "A comprehensive guide to the physics and usage of PYTHIA 8.3". In: *SciPost Phys. Codebases 8* (2022). DOI: arXiv:2203.11601. URL: https://www.pythia.org/download/pdf/pythia8300.pdf.

[43] Jerome Jung. "Dielectron production in pp collisions at s=13 TeV measured in a dedicated low magnetic-field setting with ALICE". In: (2020).

A Appendix

A.1 Chosen transverse momentum ranges

p_T ranges:
0.0 GeV/c $\leq p_T \leq$ 0.2 GeV/c
0.2 GeV/c $\leq p_T \leq$ 0.4 GeV/c
0.4 GeV/c $\leq p_{\mathrm{T}} \leq$ 0.5 GeV/c
0.5 GeV/c $\leq p_T \leq$ 0.6 GeV/c
0.6 GeV/c $\leq p_T \leq$ 0.7 GeV/c
0.7 GeV/c $\leq p_T \leq$ 0.8 GeV/c
0.8 GeV/c $\leq p_T \leq$ 0.9 GeV/c
0.9 GeV/c $\leq p_T \leq$ 1.0 GeV/c
1.0 GeV/c $\leq p_T \leq$ 1.2 GeV/c
1.2 GeV/c $\leq p_T \leq$ 1.4 GeV/c
1.4 GeV/c $\leq p_T \leq$ 1.6 GeV/c
1.6 GeV/c $\leq p_T \leq$ 1.8 GeV/c
1.8 GeV/c $\leq p_{\mathrm{T}} \leq$ 2.0 GeV/c
2.0 GeV/c $\leq p_T \leq$ 2.5 GeV/c
2.5 GeV/c $\leq p_T \leq$ 3.0 GeV/c
3.0 GeV/c $\leq p_T \leq$ 3.5 GeV/c
3.5 GeV/c $\leq p_T \leq$ 4.0 GeV/c
4.0 GeV/c $\leq p_T \leq$ 4.5 GeV/c
4.5 GeV/c $\leq p_T \leq$ 5.0 GeV/c
5.0 GeV/c $\leq p_T \leq$ 5.5 GeV/c
5.5 GeV/c $\leq p_T \leq$ 6.0 GeV/c
6.0 GeV/c $\leq p_T \leq$ 7.0 GeV/c
7.0 GeV/c $\leq p_T \leq$ 8.0 GeV/c
8.0 GeV/c $\leq p_T \leq$ 9.0 GeV/c
9.0 GeV/c $\leq p_T \leq$ 15.0 GeV/c
15.0 GeV/c $\leq p_T \leq$ 20.0 GeV/c

Table 11: Overview of the transverse momentum ranges used for the invariant mass analysis of the π^0 meson for the two γ decay mode

p_T ranges:
0.0 GeV/c $\leq p_T \leq$ 0.5 GeV/c
0.5 GeV/c $\leq p_T \leq$ 1.0 GeV/c
1.0 GeV/c $\leq p_{\mathrm{T}} \leq$ 1.25 GeV/c
1.25 GeV/c $\leq p_T \leq$ 1.50 GeV/c
1.50 GeV/c $\leq p_T \leq$ 1.60 GeV/c
2.0 GeV/c $\leq p_T \leq$ 2.50 GeV/c
2.50 GeV/c $\leq p_T \leq$ 3.0 GeV/c
3.0 GeV/c $\leq p_T \leq$ 4.0 GeV/c
4.0 GeV/c $\leq p_T \leq$ 5.0 GeV/c
5.0 GeV/c $\leq p_T \leq$ 7.0 GeV/c
7.0 GeV/c $\leq p_T \leq$ 20.0 GeV/c

Table 12: Overview of the transverse momentum ranges used for the invariant mass analysis of the π^0 meson for the Dalitz decay

p_T ranges:
0.0 GeV/c $\leq p_T \leq$ 0.5 GeV/c
0.5 GeV/c $\leq p_T \leq$ 1.0 GeV/c
1.0 GeV/c $\leq p_{\mathrm{T}} \leq$ 1.5 GeV/c
1.5 GeV/c $\leq p_T \leq$ 2.0 GeV/c
2.0 GeV/c $\leq p_T \leq$ 2.5 GeV/c
2.5 GeV/c $\leq p_T \leq$ 3.5 GeV/c
3.5 GeV/c $\leq p_T \leq$ 6.0 GeV/c
6.0 GeV/c $\leq p_T \leq$ 10.0 GeV/c
10.0 GeV/c $\leq p_T \leq$ 20.0 GeV/c

Table 13: Overview of the transverse momentum ranges used for the invariant mass analysis of the η meson and for the π^0 meson to compare to the η meson

A.2 Detailed interaction rates

run number	interaction rate [kHz]
526641	498
526964	505
527041	499
527057	510
527109	490
527240	494
527850	505
527871	508
527859	505
527899	508
528292	508
528461	507
528531	513

Table 14: Interaction rates for the different Run numbers that were used for the data and Monte Carlo Sets.

A.2.1 Explanation of φ_v

As already mentioned in chapter 4.2, φ_v is the angle between the direction of the magnetic field and the direction that is normal to the plane which the e^+e^- pair opens. Mathematically this means

$$\varphi_v = arccos\left(\frac{\vec{w}\cdot\vec{a}}{|\vec{w}|\cdot|\vec{a}|}\right) \tag{39}$$

with

- the normalised direction of the sum of the momenta of the two decay particles: $\vec{u} = \frac{\vec{p_+}+\vec{p_-}}{|\vec{p_+}+\vec{p_-}|}$
- the unit vector perpendicular to the the momenta of the electron and positron: $\vec{v} = \frac{\vec{p_+}\times\vec{p_-}}{|\vec{p_+}\times\vec{p_-}|}$
- the vector perpendicular to $\vec{u}$ and $\vec{v}$: $\vec{w} = \vec{u}\times\vec{v}$
- the unit vector perpendicular to $\vec{u}$ and the direction of the magnetic field $\vec{a} = \frac{\vec{u}\times\vec{z}}{|\vec{u}\times\vec{z}|}$

where $\vec{p_+}$ and $\vec{p_-}$ are the momentum vectors of the positron and electron and $\vec{z}$ is the direction of the magnetic field [43].
Dilepton pairs that origin from photon conversion can only move in the direction perpendicular to the magnetic field. For now let´s assume that the magnetic field is in the $\vec{z}$ direction. Than the electron and positron have to be in the x-y-plane. Therefore $\vec{v}$ is in the direction of the magnetic field and this leads to $\vec{w}$ and $\vec{a}$ to point in opposite directions.
However, as primary dileptons are not bound to be in the plane perpendicular to the magnetic field, this relation does not hold for them. And therefor the φ_v cut can cancel out dileptons from photon conversions. But of course some primary dileptons are not considered with this selection criterion as well.

A.3 Invariant mass appendices

A.3.1 Invariant mass analysis of the π^0 meson

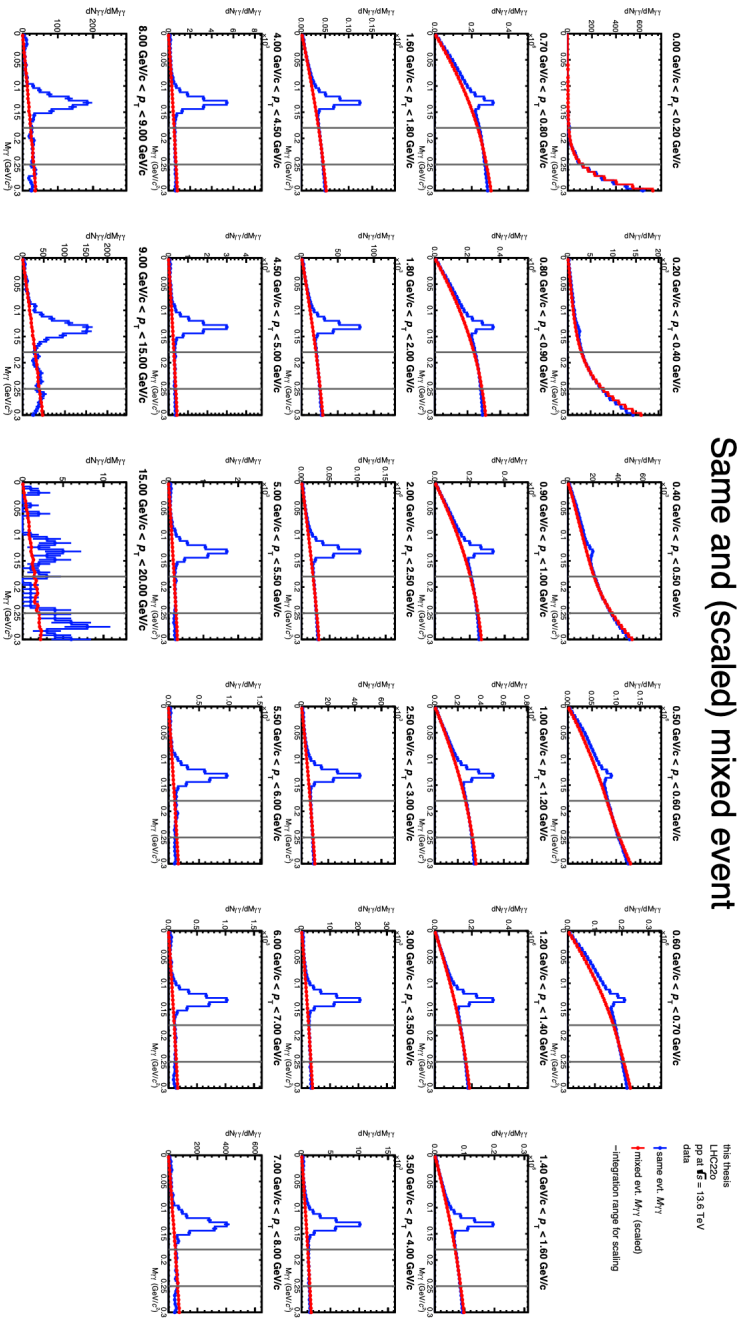

Figure 37: Same and mixed background subtraction to the invariant mass spectrum of the two γ decay for each transverse momentum range for the π^0 meson. Here the full data set was used.

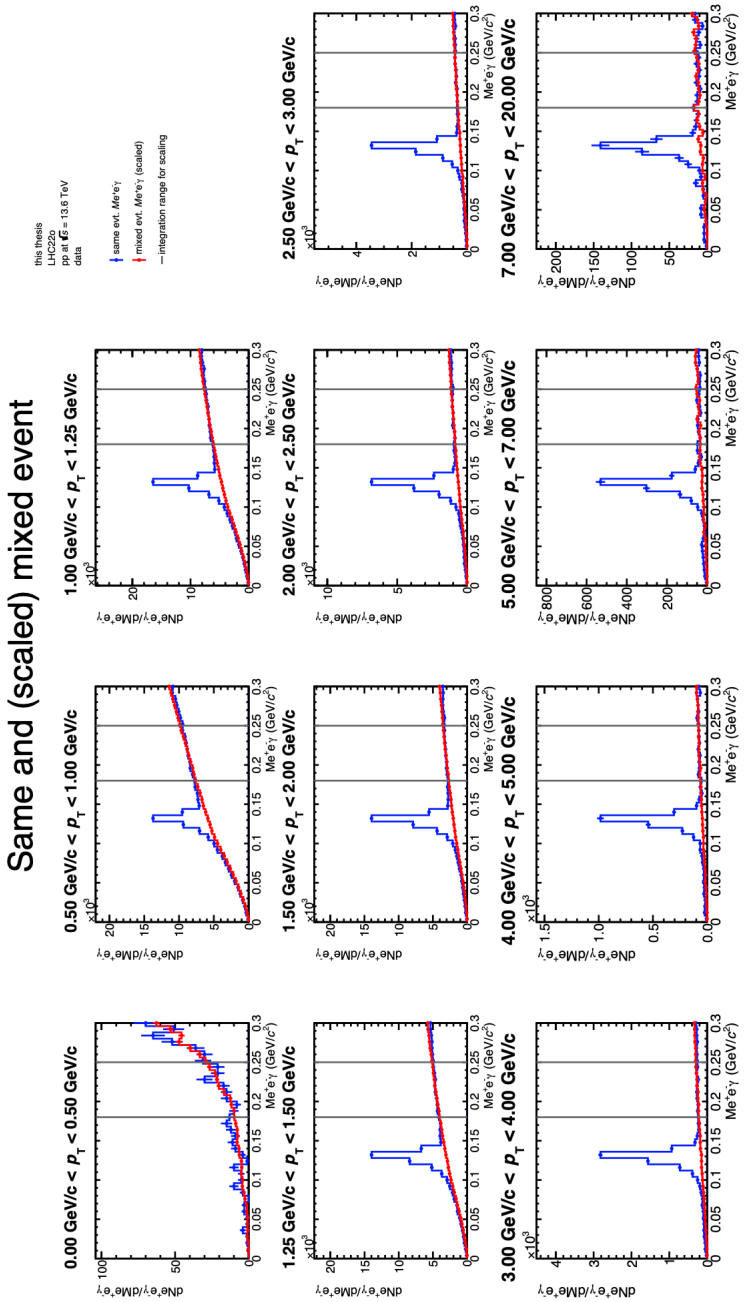

Figure 38: Same and mixed background subtraction to the invariant mass spectrum of the Dalitz decay for each transverse momentum range for the π^0 meson. Here the full data set was used.

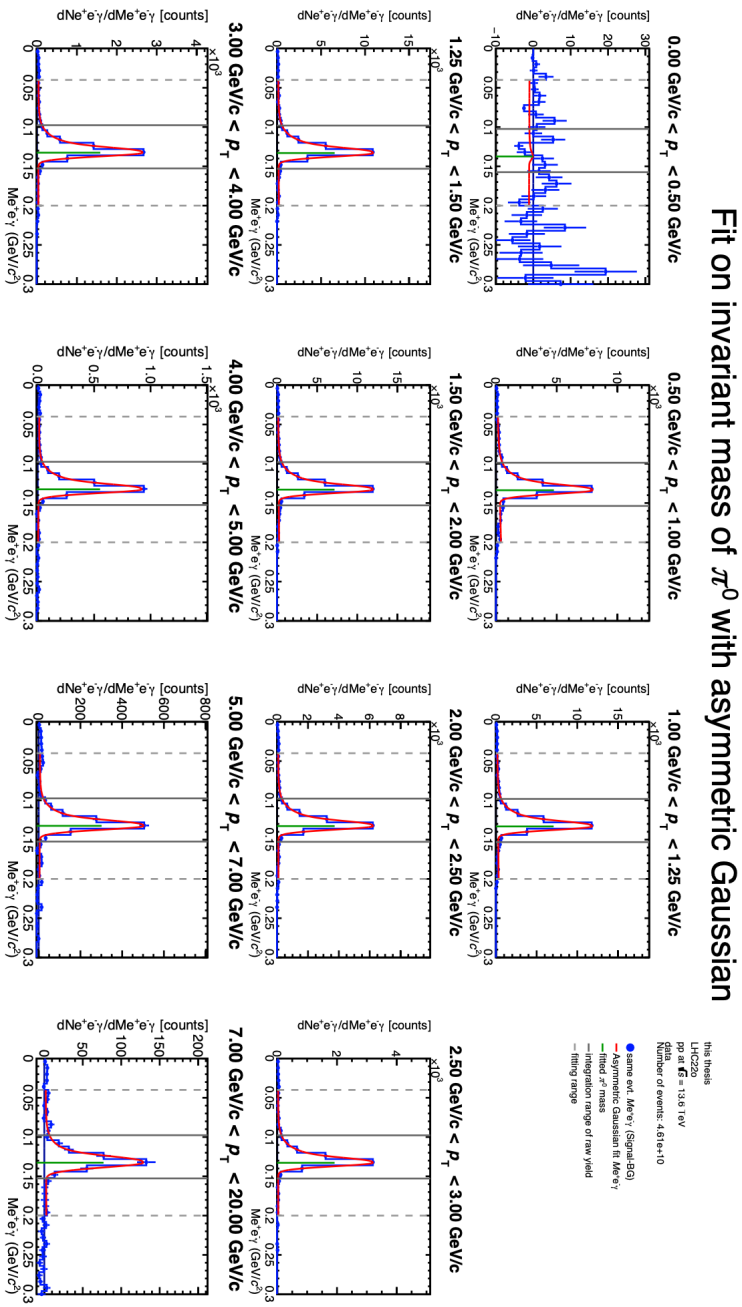

Figure 39: Fit of the asymmetric Gaussian to the invariant mass spectrum of the Dalitz decay after subtraction of the combinatorial background for each transverse momentum range for the π^0 meson. Here the full data set was used.

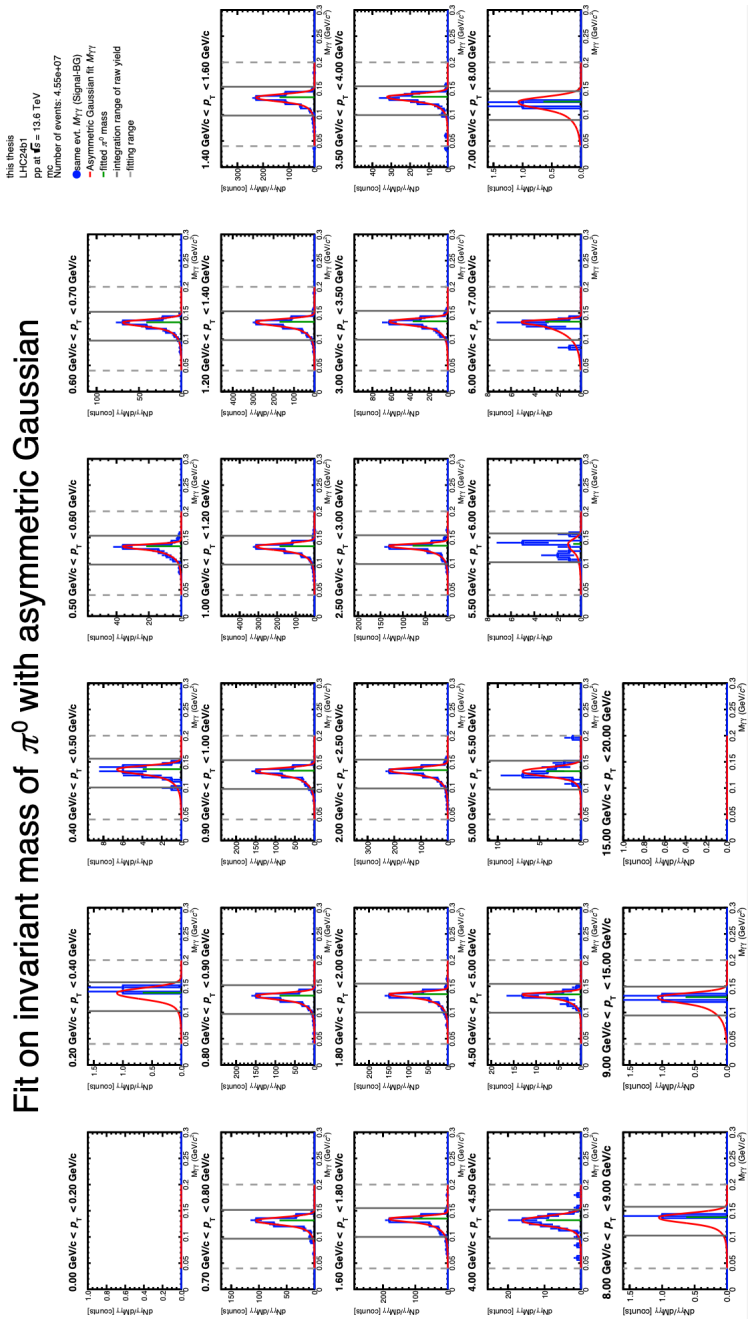

Figure 40: Fit of the asymmetric Gaussian to the invariant mass spectrum of the two γ decay after subtraction of the combinatorial background for each transverse momentum range for the Monte Carlo Simulation of the π^0 meson. Here the full data set was used.

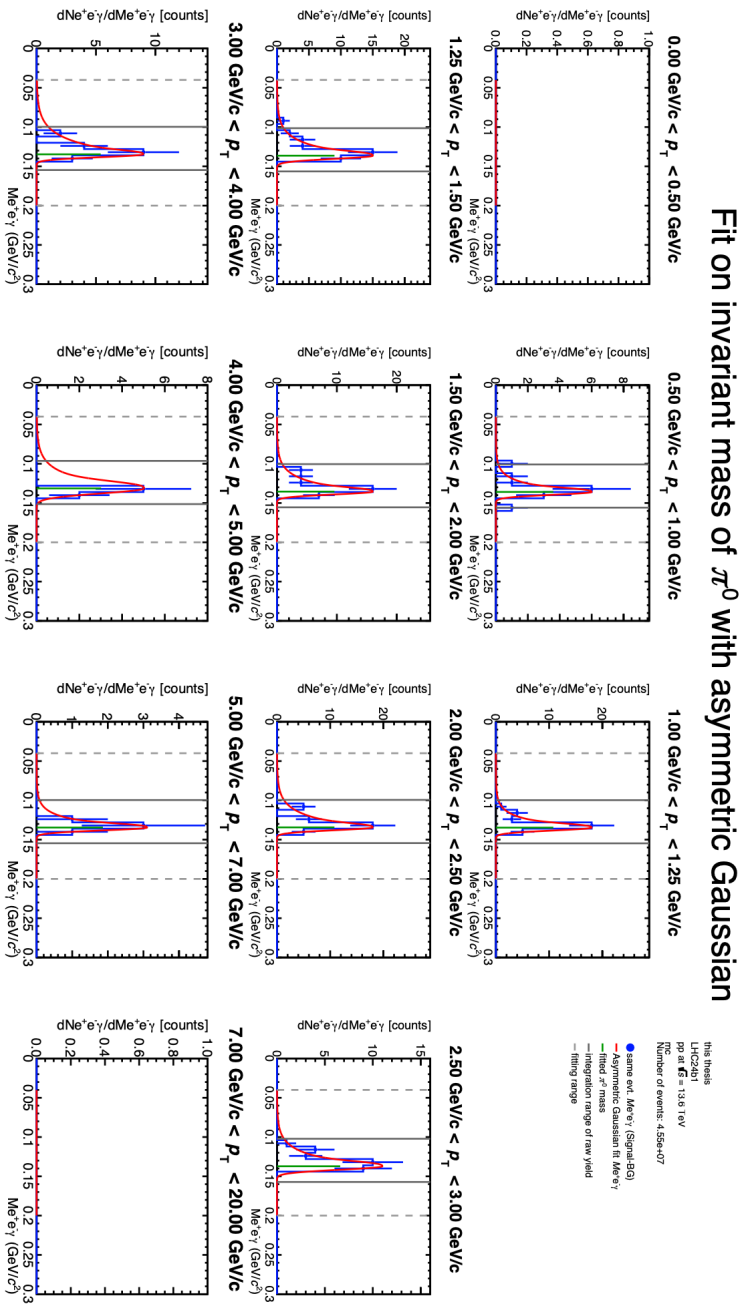

Figure 41: Fit of the asymmetric Gaussian to the invariant mass spectrum of the Dalitz decay after subtraction of the combinatorial background for each transverse momentum range for the Monte Carlo Simulation of the π^0 meson. Here the full data set was used.

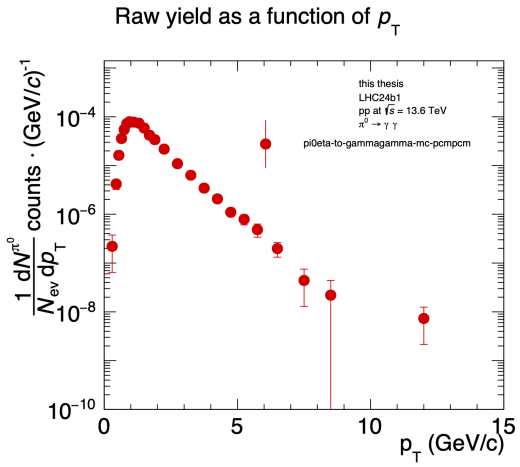

Figure 42: raw yield for the π^0 meson extracted from Monte Carlo Simulation for the two γ decay channel

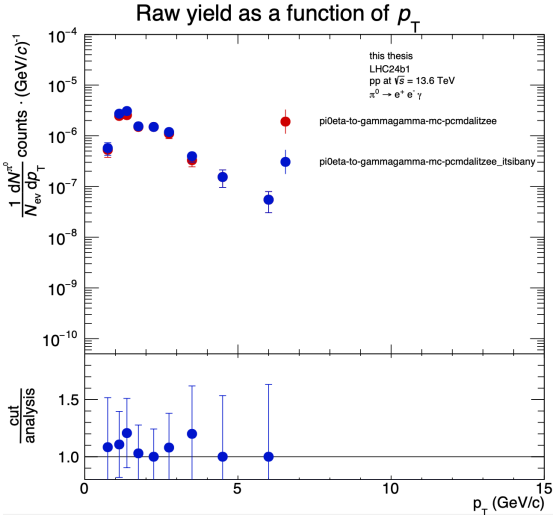

Figure 43: raw yield for the π^0 meson extracted from Monte Carlo Simulation for the Dalitz decay channel

A.3.2 Invariant mass analysis of the π^0 meson with the binning that is compatible to the η meson

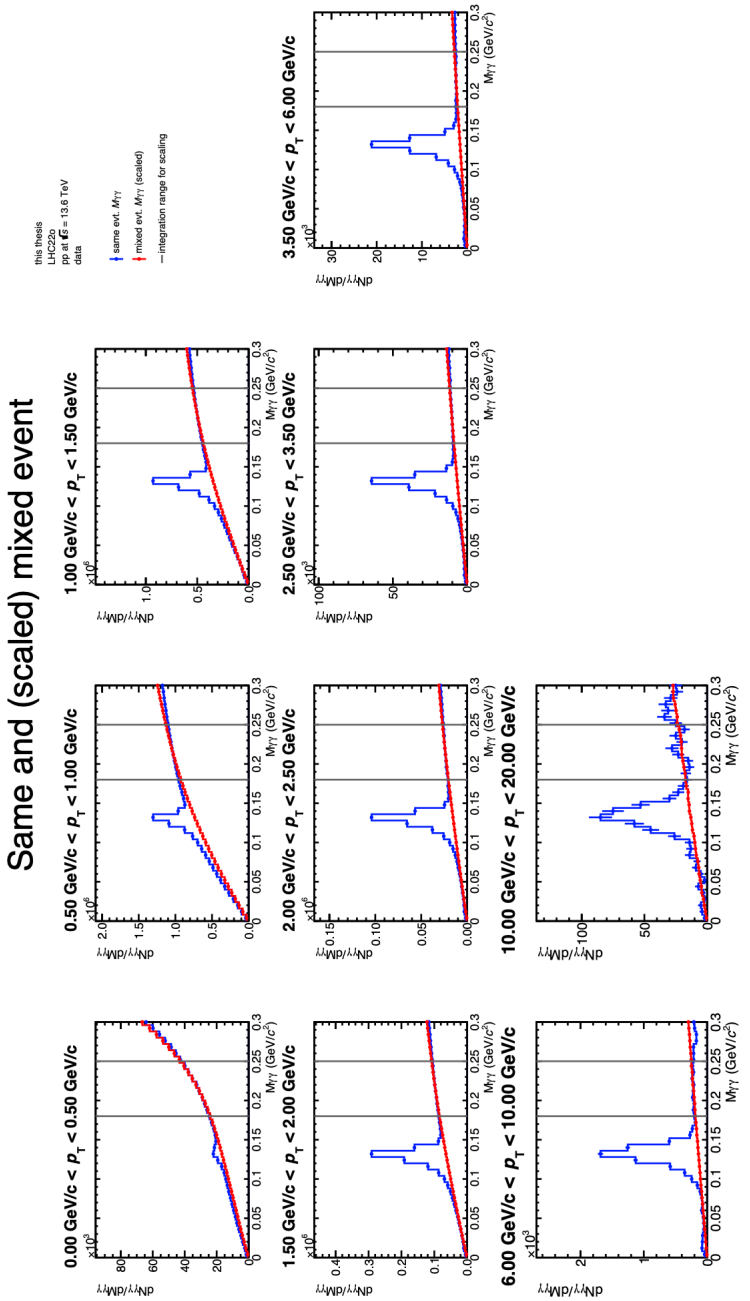

Figure 44: Same and mixed background subtraction to the invariant mass spectrum of the two γ decay for each transverse momentum range for the π^0 meson. Here the full data set was used in the binning compatible to the η meson.

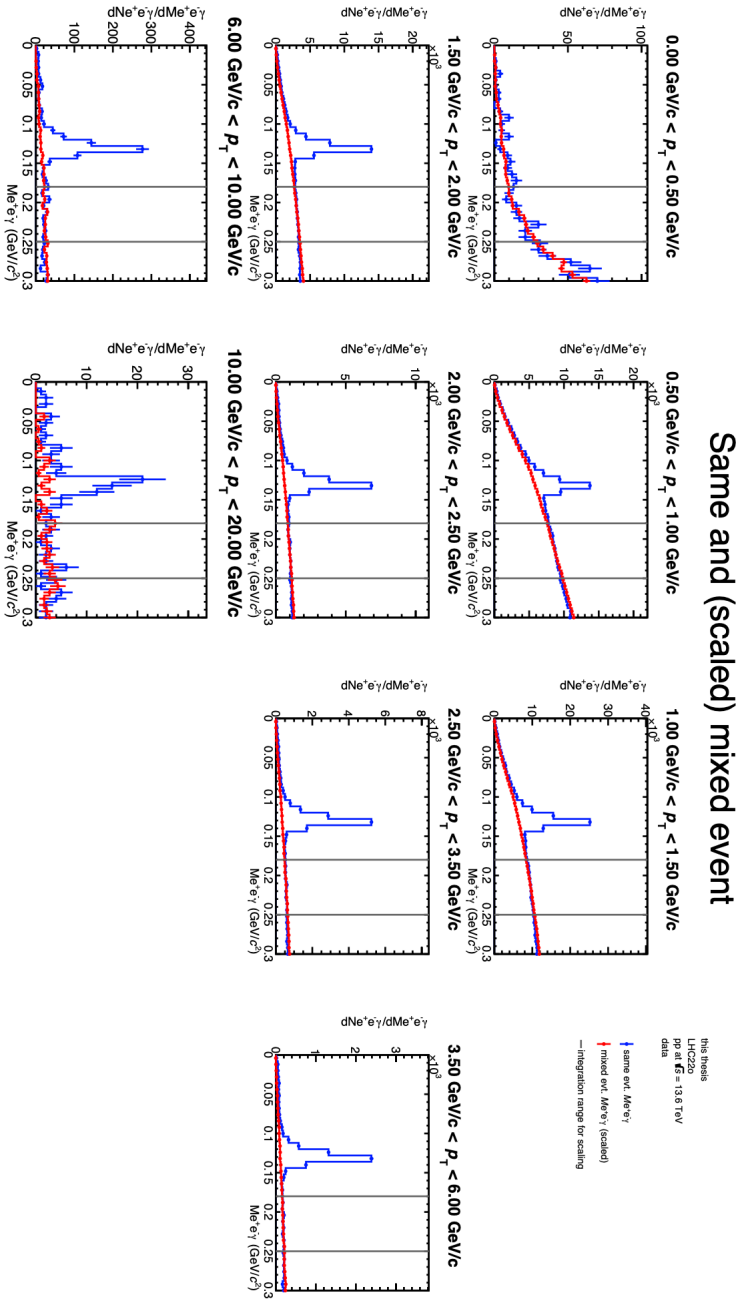

Figure 45: Same and mixed background subtraction to the invariant mass spectrum of the Dalitz decay for each transverse momentum range for the π^0 meson. Here the full data set was used in the binning compatible to the η meson.

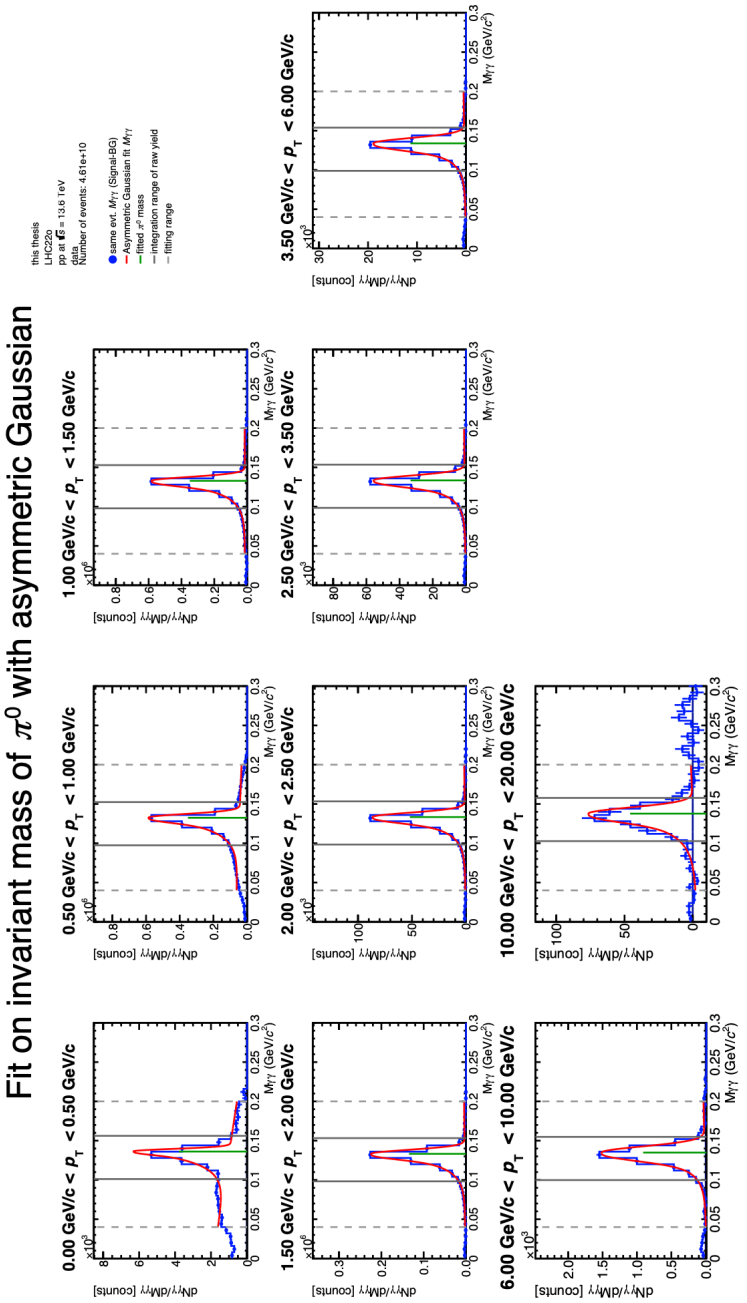

Figure 46: Fit of the asymmetric Gaussian to the invariant mass spectrum of the two γ decay after subtraction of the combinatorial background for each transverse momentum range for the π^0 meson. Here the full data set was used in the binning compatible to the η meson.

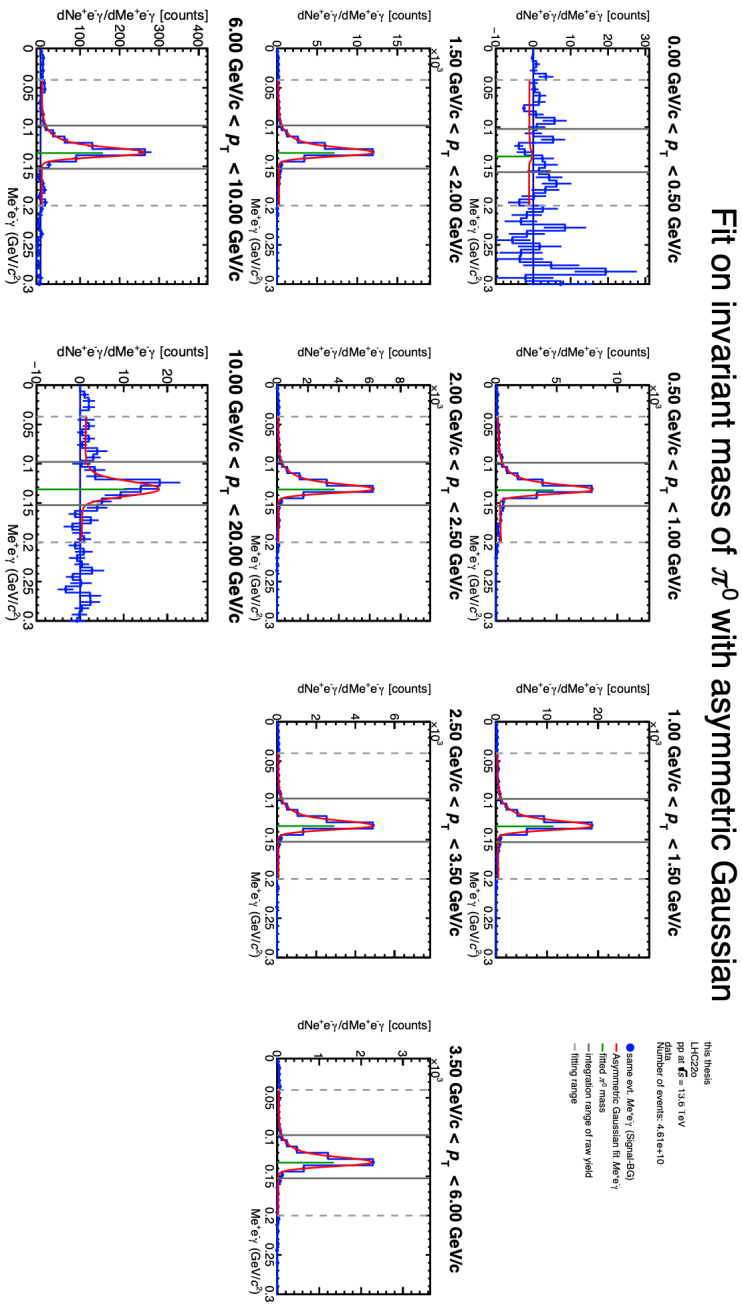

Figure 47: Fit of the asymmetric Gaussian to the invariant mass spectrum of the Dalitz decay after subtraction of the combinatorial background for each transverse momentum range for the π^0 meson. Here the full data set was used in the binning compatible to the η meson.

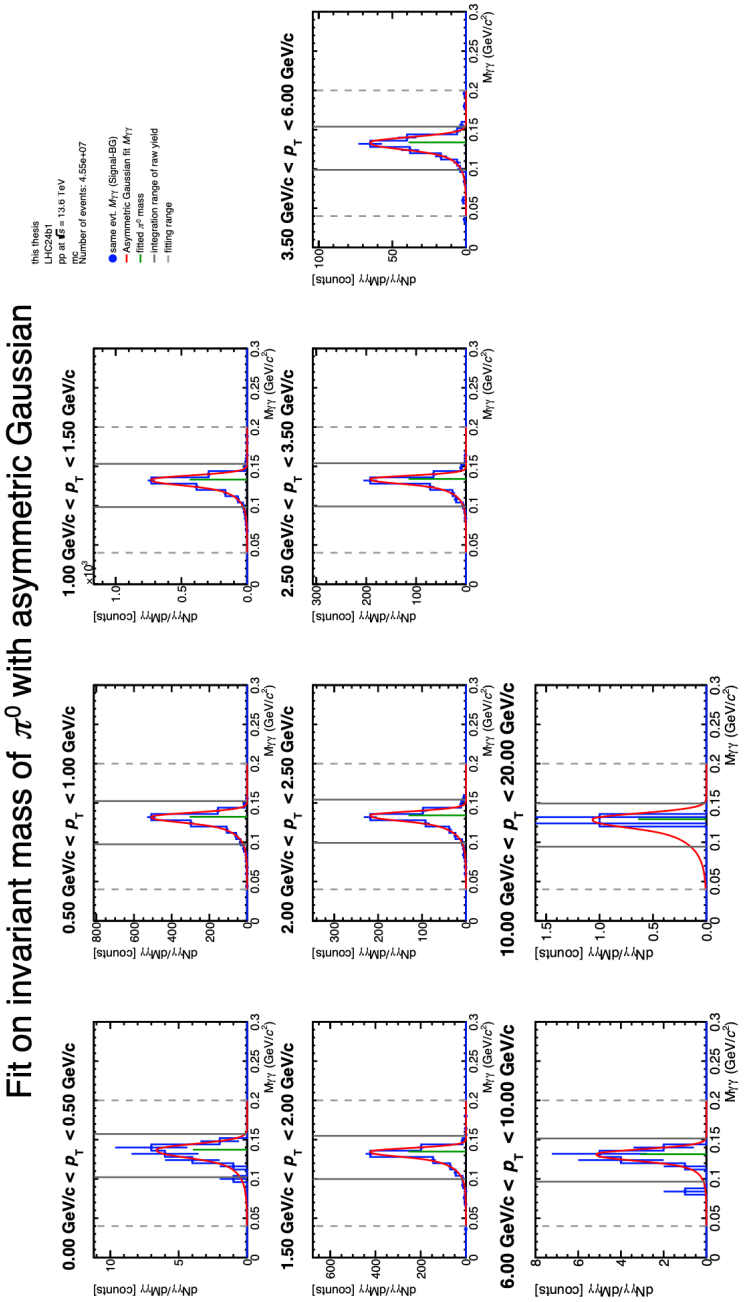

Figure 48: Fit of the asymmetric Gaussian to the invariant mass spectrum of the two γ decay after subtraction of the combinatorial background for each transverse momentum range for the Monte Carlo Simulation of the π^0 meson. Here the full data set was used in the binning compatible to the η meson.

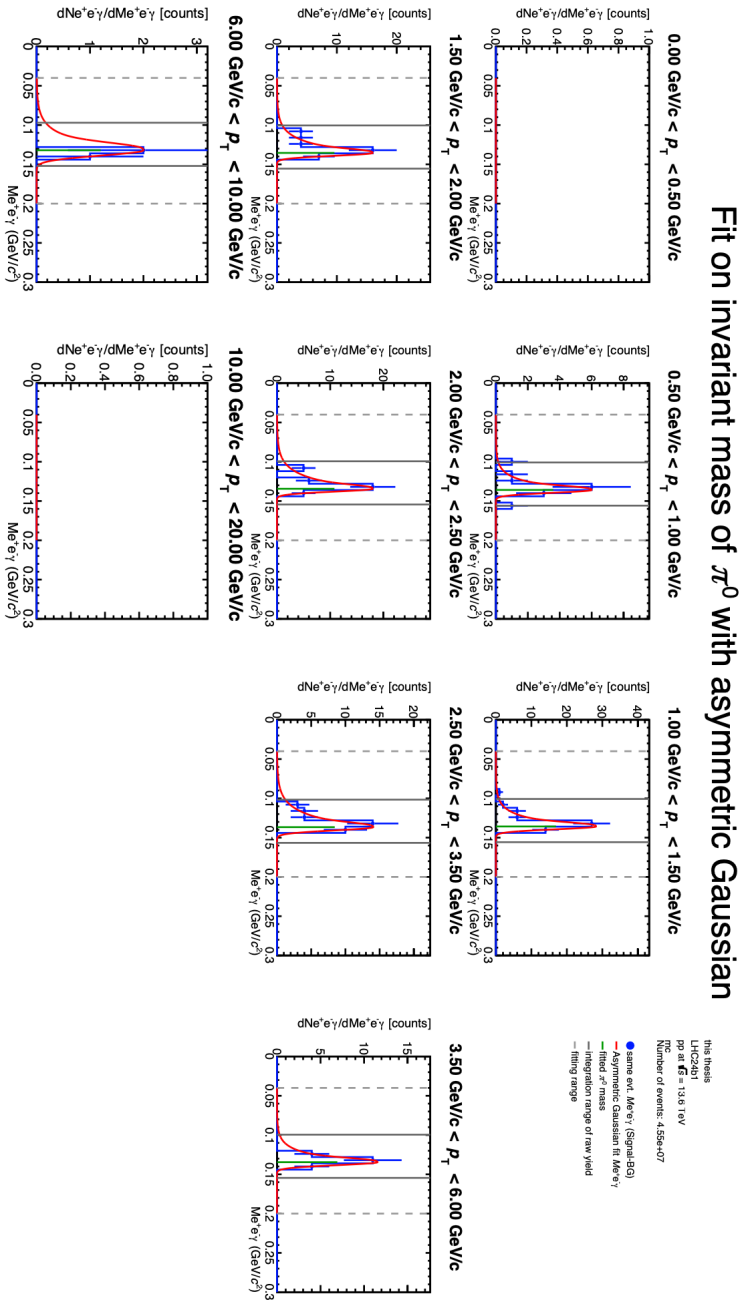

Figure 49: Fit of the asymmetric Gaussian to the invariant mass spectrum of the Dalitz decay after subtraction of the combinatorial background for each transverse momentum range for the Monte Carlo Simulation of the π^0 meson. Here the full data set was used in the binning compatible to the η meson.

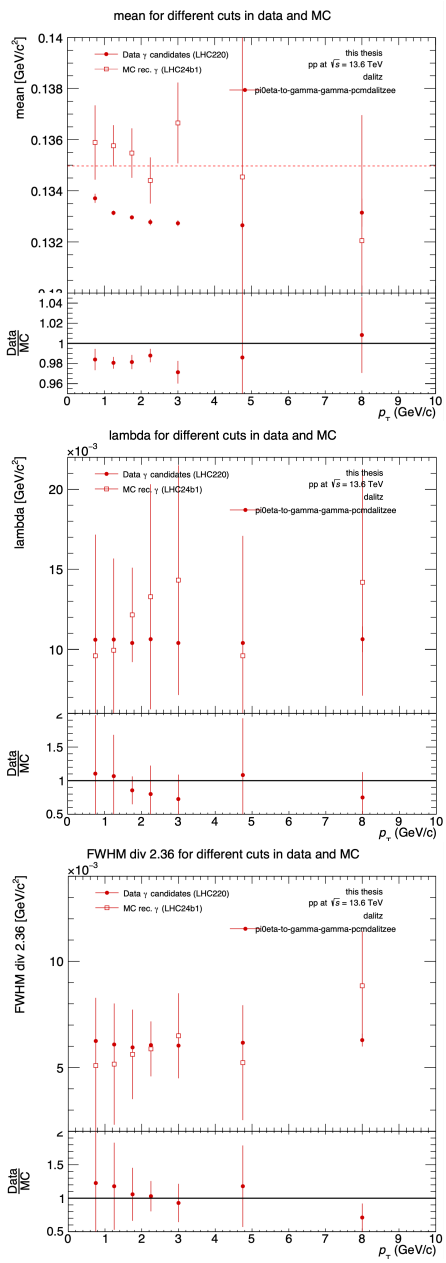

Figure 50: Comparison between the result obtained with Monte Carlo (empty squares) and with data (solid dots) of the obtained fit parameters from the asymmetric Gaussian and the given ratio between data and Monte Carlo. Upper: mean value for the asymmetric Gaussian, middle: inverse slope λ of the Bremsstrahlung tail of the fit function, lower: FWHM/2.36 of the peak of the Gaussian. Here for the Dalitz decay channel of the π^0 meson.

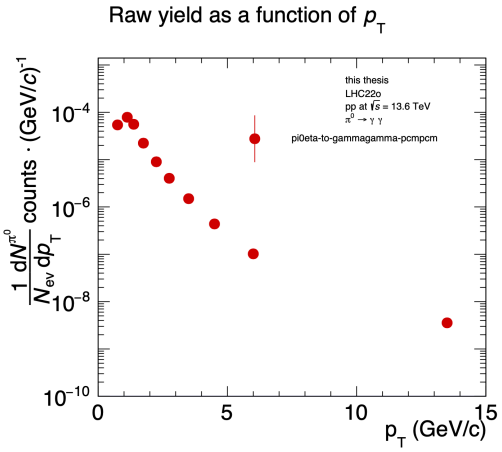

Figure 51: raw yield for the π^0 meson extracted from data for the two γ decay channel used in the binning compatible to the η meson

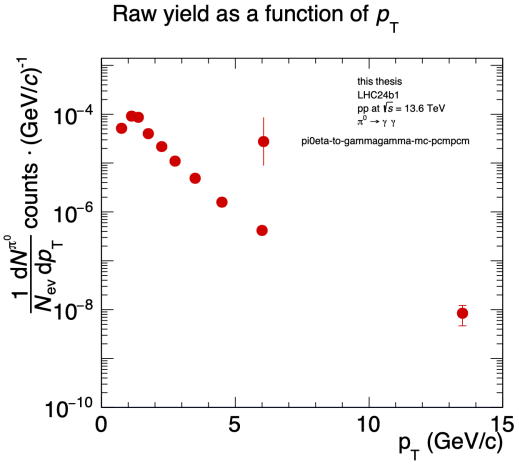

Figure 52: raw yield for the π^0 meson extracted from Monte Carlo Simulation for the two γ decay channel used in the binning compatible to the η meson

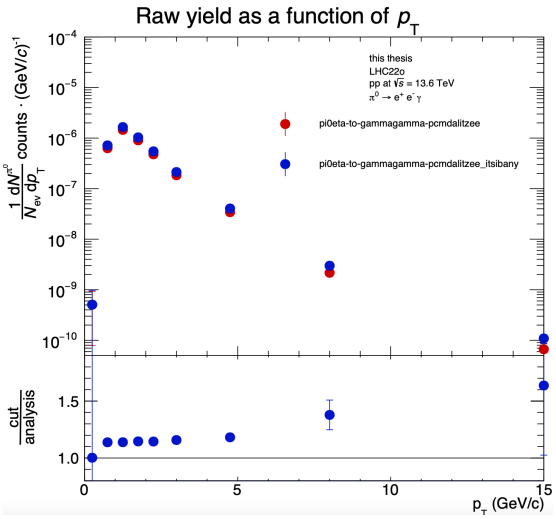

Figure 53: raw yield for the π^0 meson extracted from data for the Dalitz decay channel

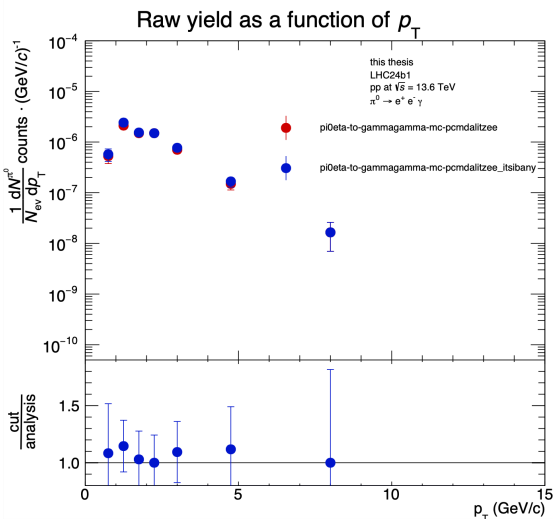

Figure 54: raw yield for the π^0 meson extracted from Monte Carlo Simulation for the Dalitz decay channel

A.3.3 Invariant mass analysis of the η meson

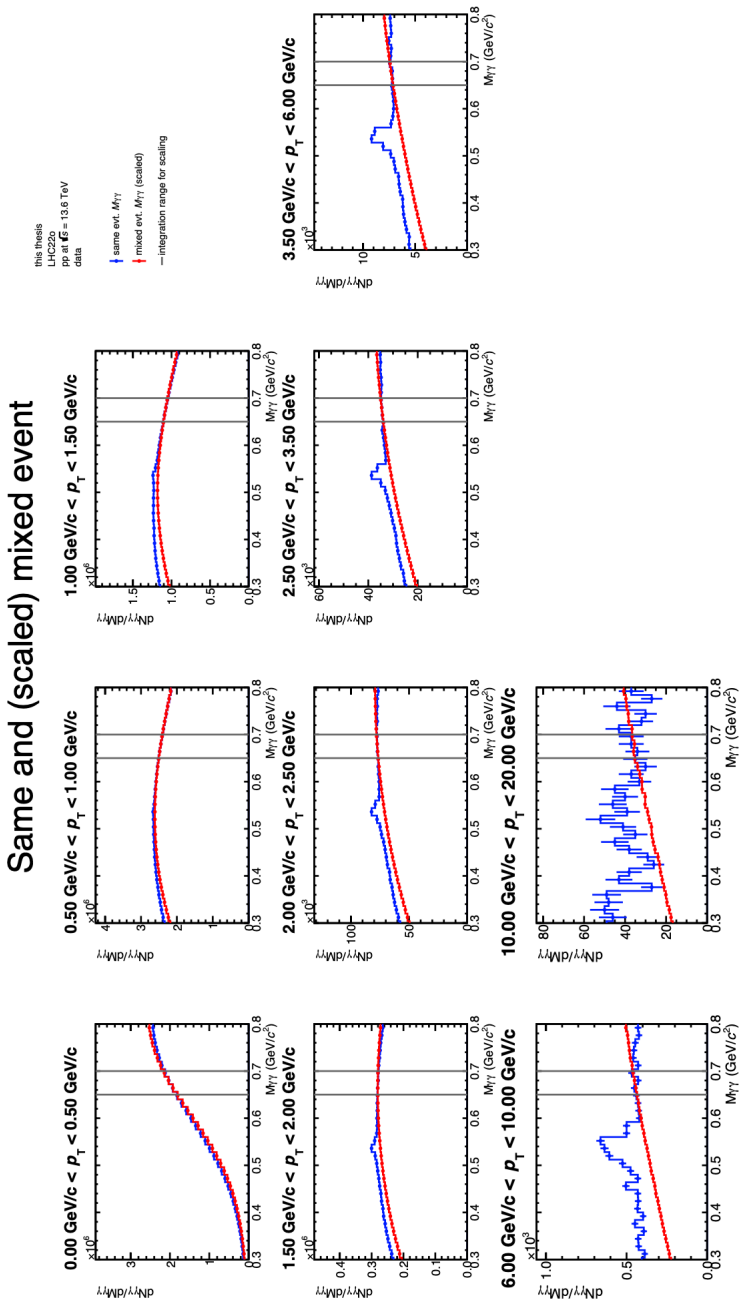

Figure 55: Same and mixed background subtraction to the invariant mass spectrum of the two γ decay for each transverse momentum range for the η meson. Here the full data set was used.

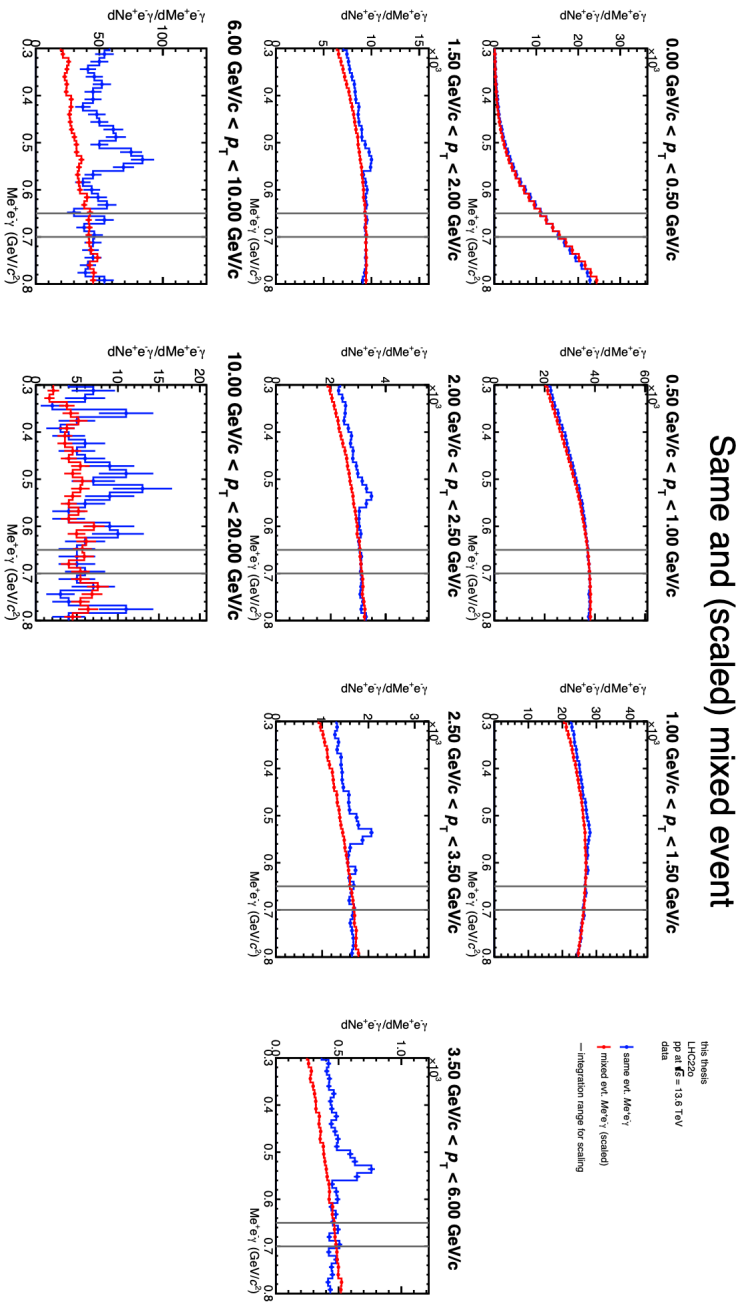

Figure 56: Same and mixed background subtraction to the invariant mass spectrum of the Dalitz decay for each transverse momentum range for the η meson. Here the full data set was used.

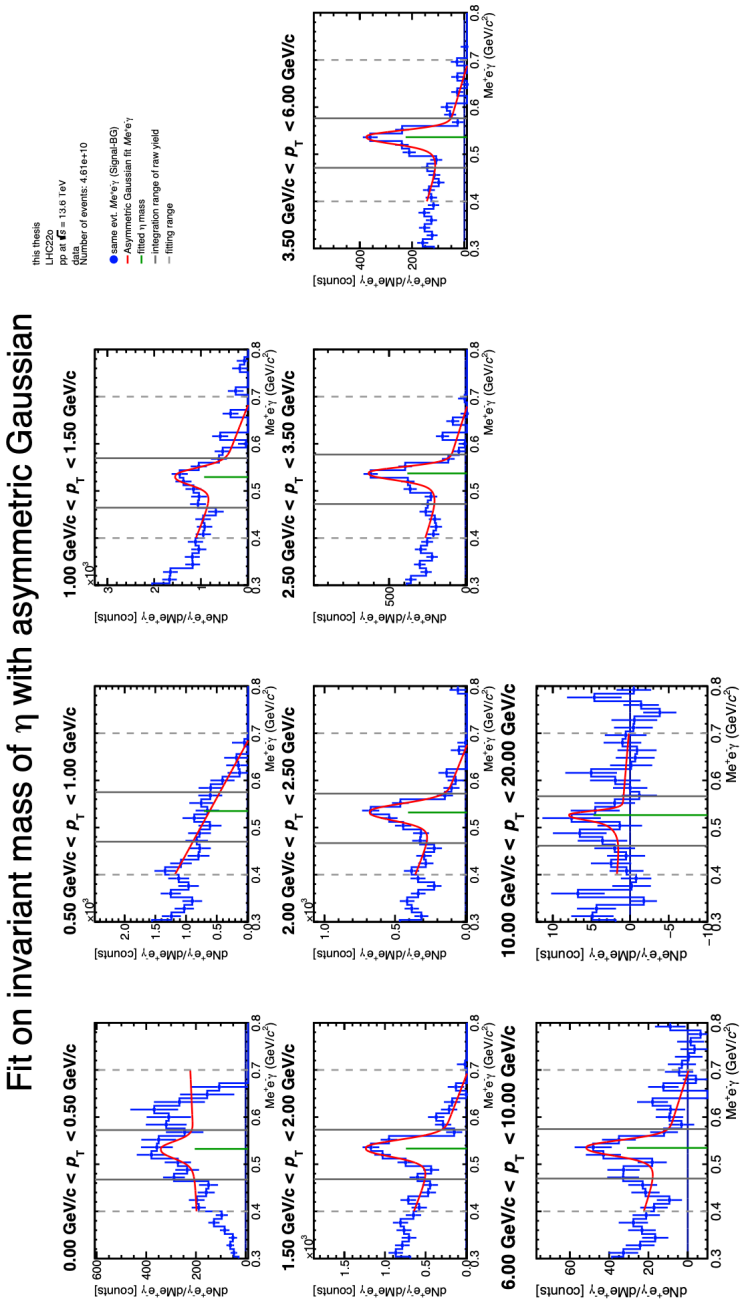

Figure 57: Fit of the asymmetric Gaussian to the invariant mass spectrum of the Dalitz decay after subtraction of the combinatorial background for each transverse momentum range for the η meson. Here the full data set was used.

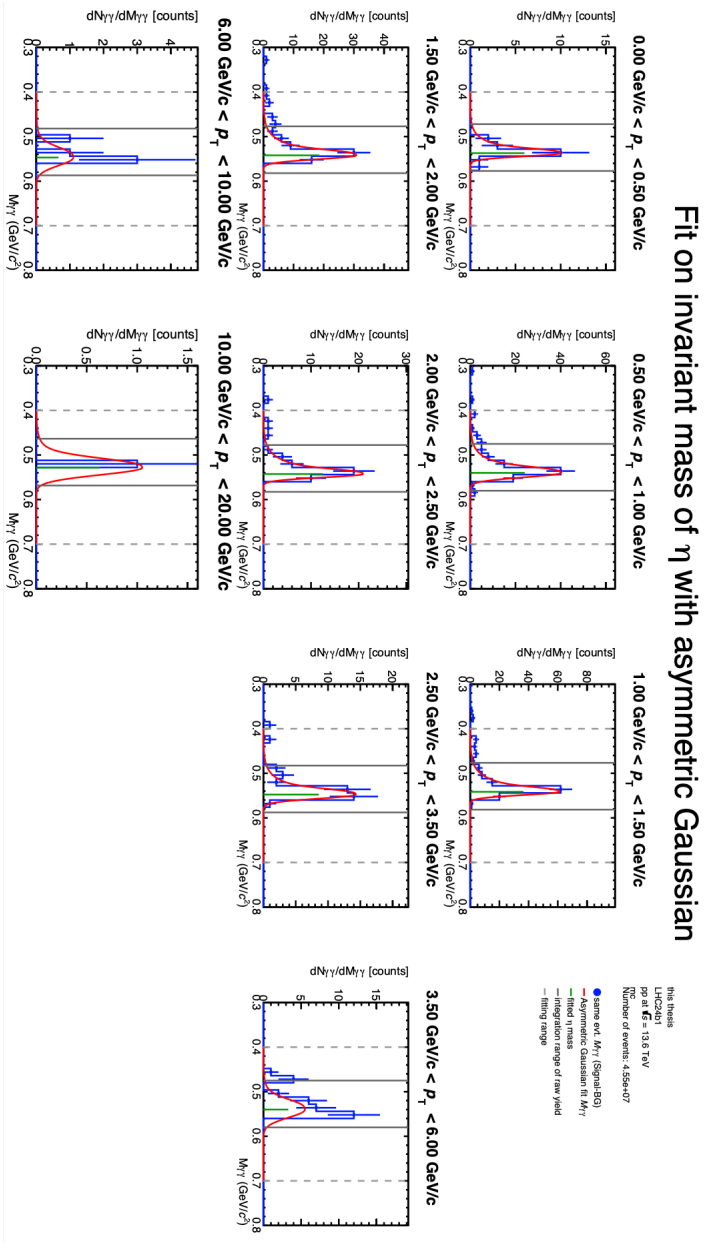

Figure 58: Fit of the asymmetric Gaussian to the invariant mass spectrum of the two γ decay after subtraction of the combinatorial background for each transverse momentum range for the Monte Carlo Simulation of the η meson. Here the full data set was used.

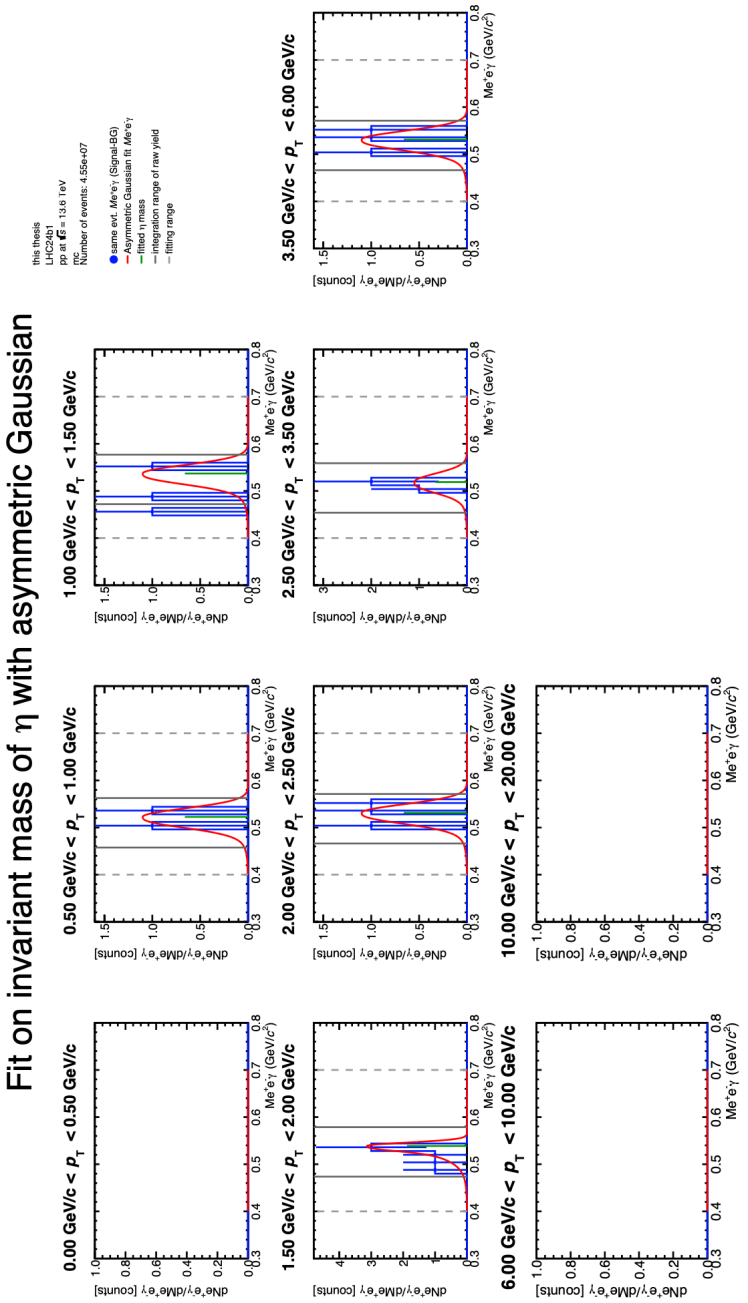

Figure 59: Fit of the asymmetric Gaussian to the invariant mass spectrum of the Dalitz decay after subtraction of the combinatorial background for each transverse momentum range for the Monte Carlo Simulation of the η meson. Here the full data set was used.

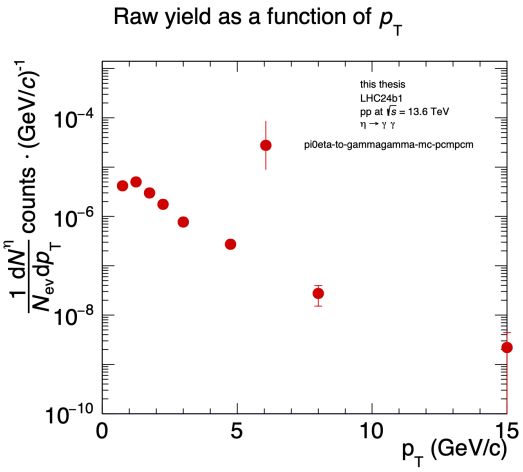

Figure 60: raw yield for the η meson extracted from Monte Carlo Simulation for the two γ decay channel

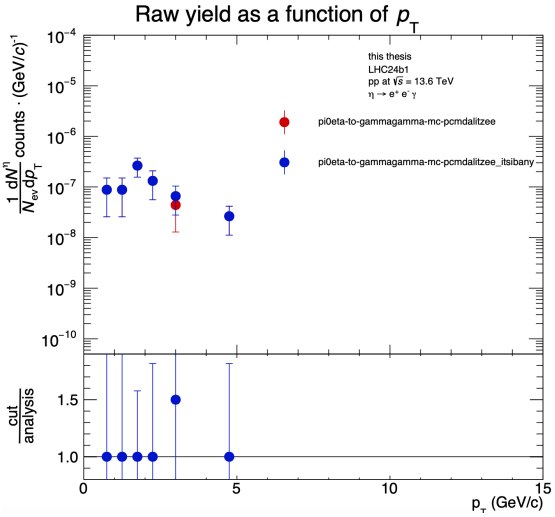

Figure 61: raw yield for the η meson extracted from Monte Carlo Simulation for the Dalitz decay channel

A.4 Appendices for the correction process

A.4.1 Corrections for the π^0 meson

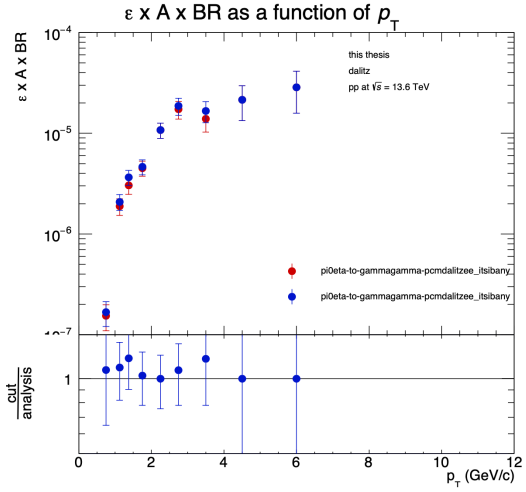

Figure 62: Comparison of the product of efficiency, acceptance and branching ratio between the two cuts of the Dalitz decay for the π^0 meson.

Collision Energy (TeV)	13.0 (this thesis)	13.6
A_e $\left(\frac{pbarn \cdot c^3}{GeV^2}\right)$	(343.266 ± 66.4) $\cdot 10^9$	(196.120 ± 42.517) $\cdot 10^9$
T_e (GeV)	0.175 ± 0.020	0.202 ± 0.016
A $\left(\frac{pbarn \cdot c^3}{GeV^2}\right)$	(22.360 ± 9.989) $\cdot 10^9$	(40.500 ± 17.993) $\cdot 10^9$
T (GeV)	0.675 ± 0.081	0.565 ± 0.019
n	3.014 ± 0.101	3.427 ± 0.152

Table 15: Parameters of the TCM fit for the π^0 meson in Run 2 and Run 3 for the Dalitz decay

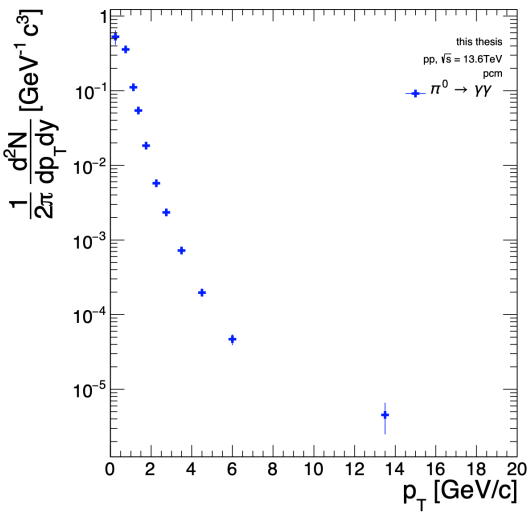

Figure 63: Invariant yield for the π^0 meson in the two γ decay channel

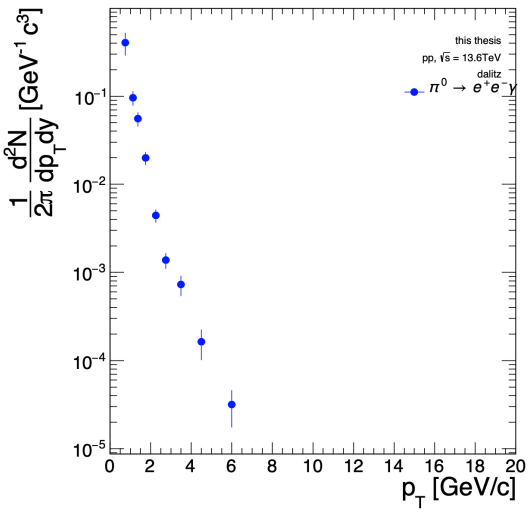

Figure 64: Invariant yield for the π^0 meson in the Dalitz decay channel

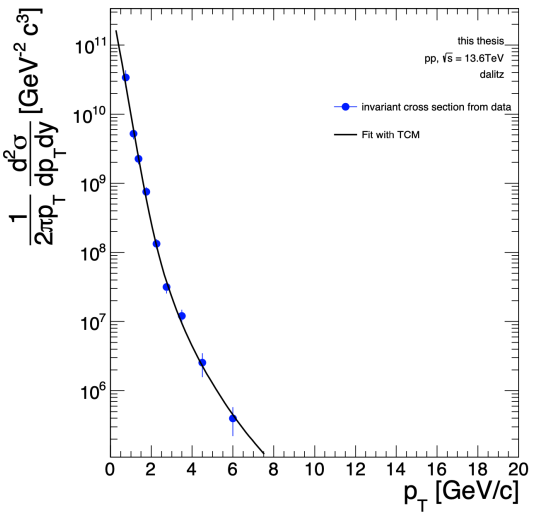

Figure 65: Two Component Model fit to the corrected yield for the Dalitz decay of the π^0 meson

A.4.2 Comparison of the TEfficiency of the π^0 meson

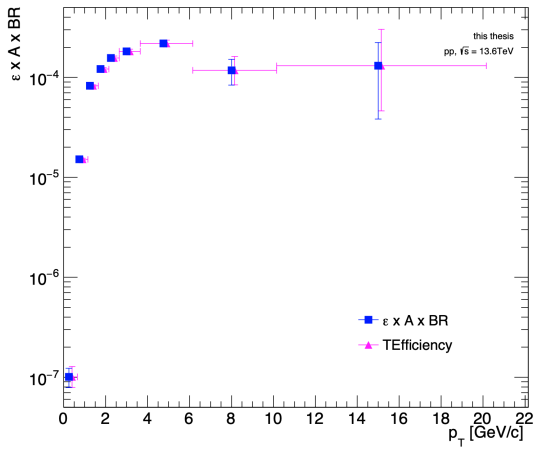

Figure 66: Comparison of the product of TEfficiency, acceptance and branching ratio with the product of efficiency, acceptance and branching ratio used in this thesis for the two γ decay of the π^0 meson

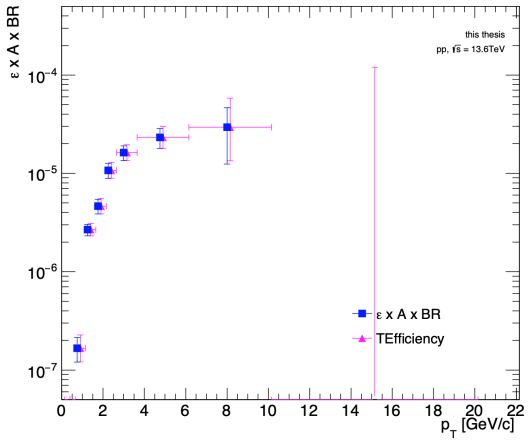

Figure 67: Comparison of the product of TEfficiency, acceptance and branching ratio with the product of efficiency, acceptance and branching ratio used in this thesis for the Dalitz decay of the π^0 meson

A.4.3 Corrections for the η meson

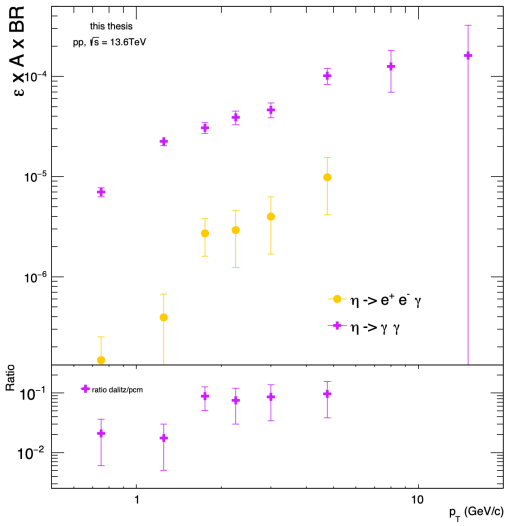

Figure 68: Product of efficiency, acceptance and branching ratio for the two decay modes of the η meson

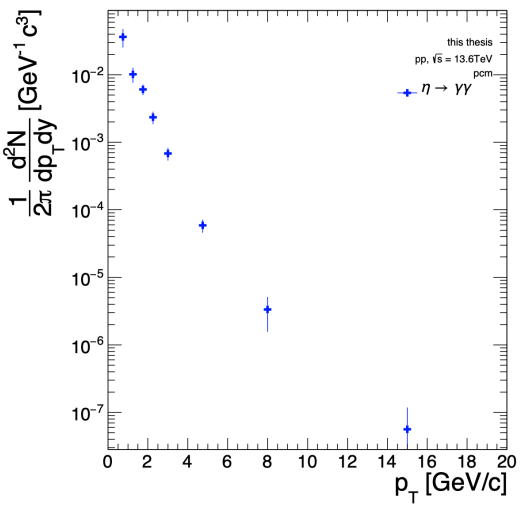

Figure 69: Invariant yield for the η meson in the two γ decay channel

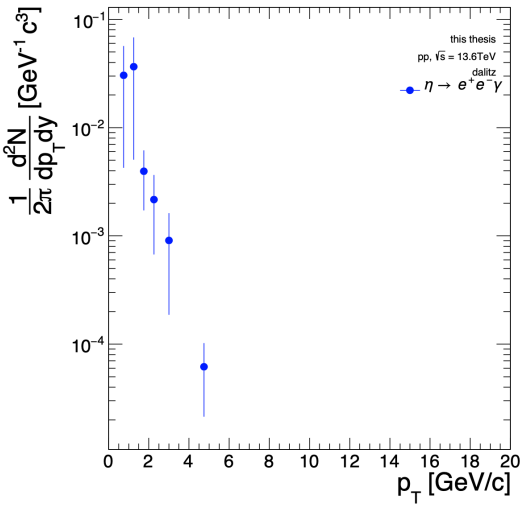

Figure 70: Invariant yield for the η meson in the Dalitz decay channel

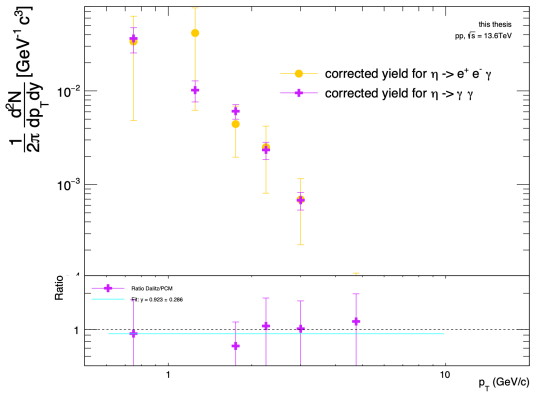

Figure 71: Comparison between the invariant yield of the two γ decay mode and the Dalitz decay mode for the η meson.

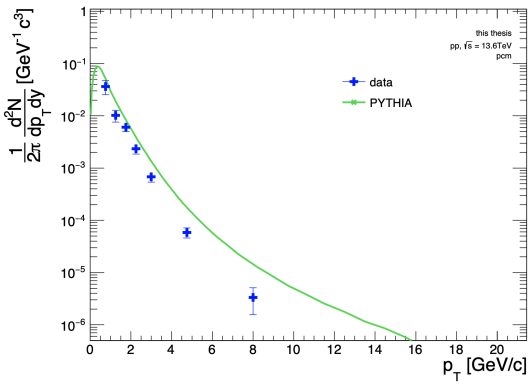

Figure 72: Comparison between the PYTHIA 8 simulation (green) and the results obtained in this thesis for the η meson for the two γ decay

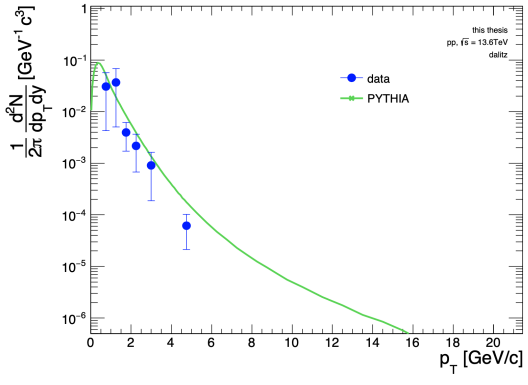

Figure 73: Comparison between the PYTHIA 8 simulation (green) and the results obtained in this thesis for the η meson for the Dalitz decay

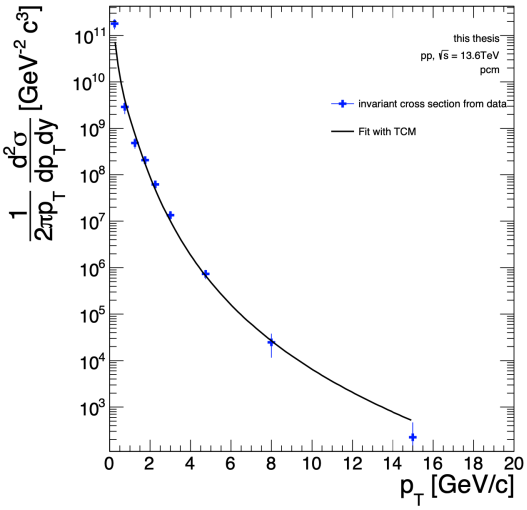

Figure 74: TCM fit to the invariant yield obtained for the η meson for the two γ decay mode

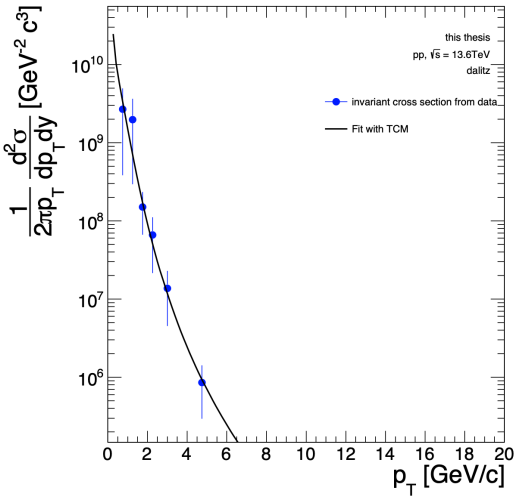

Figure 75: TCM fit to the invariant yield obtained for the η meson for the Dalitz decay mode

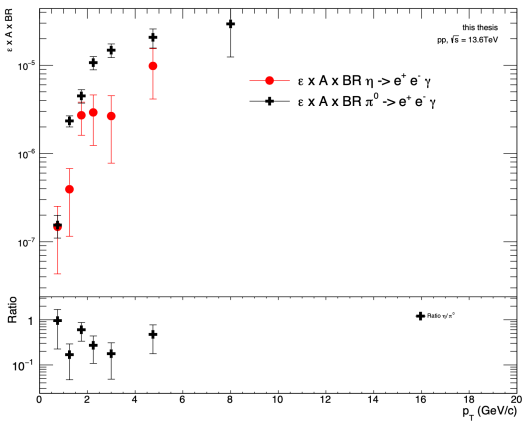

Figure 76: Comparison of the product of efficiency, acceptance and branching ratio for the η and the π^0 meson for the Dalitz decay mode.

A.4.4 Comparison of the TEfficiency of the η

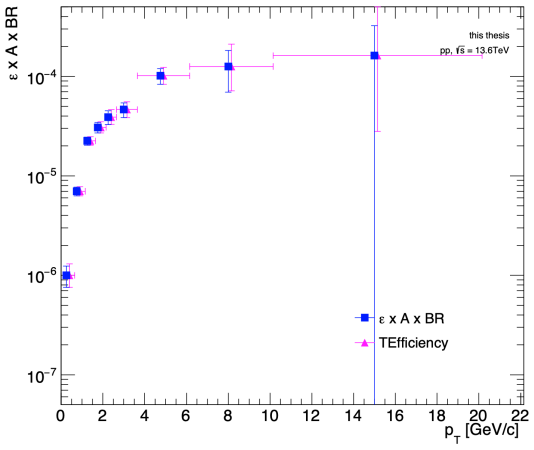

Figure 77: Comparison of the product of TEfficiency, acceptance and branching ratio with the product of efficiency, acceptance and branching ratio used in this thesis for the two γ decay of the η meson

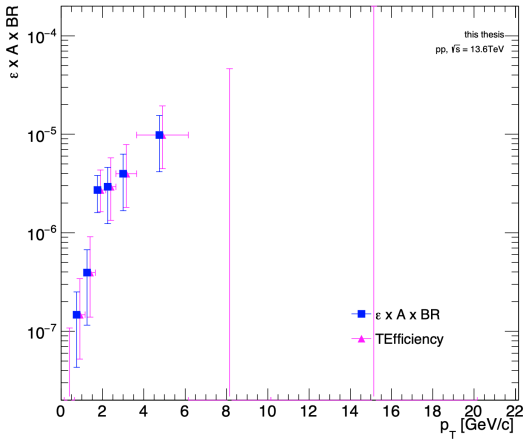

Figure 78: Comparison of the product of TEfficiency, acceptance and branching ratio with the product of efficiency, acceptance and branching ratio used in this thesis for the Dalitz decay of the η meson

B Acronyms

LHC Large Hadron Collider

CERN Conseil europée pour la Recherche nucléaire

ALICE A Large Ion Collider Experiment

QGP Quark-Gluon Plasma

O2 Online-Offline

QCD Quantum Chromo Dynamics

ITS 2 Inner Tracking System 2

TPC Time Projection Chamber

TRD Transition Radiation Detector

TOF Time of Flight

FIT Fast Interaction Trigger

MAPS Monolithic Active Pixel Sensors

IROC inner readout channel

OROC outer readout channel

GEMs Gas Electron Multipliers

MRPCs Multigap Resistive Plate Chambers

MCP´s Micro Channel Plate-based photomultipliers

PCM Photon Conversion Method

PHOS Photon Spectrometer

EMCal Electromagnetic Calorimeter

C List of figures

List of Figures

D List of tables

List of Tables

E Acknowledgements

Firstly, i would like to express my gratitude to Prof. Dr. Johanna Stachel for providing me with the opportunity to write my Bachelor's thesis under her supervision. Furthermore, i would like to thank Prof. Dr. Klaus Reygers for acting as the second examiner of my thesis.

I would like to express my sincerest gratitude to Dr. Ana Marin for providing me with invaluable guidance and support throughout the process of my thesis, and for acting as an outstanding mentor. I am particularly grateful for her willingness to address all queries that arose during the analysis process and for her consistently constructive feedback.

Also i want to express my heartfelt appreciation to my mother, Claudia Schlägel, who checked my entire thesis for any potential grammatical or linguistic errors. Also i want to thank Marius Baumann and Philipp Weingardt for proofreading my thesis.

Finally i would like to express my gratitude to my friends and family for their unwavering support, encouragement and love throughout my studies.

F Declaration of Authorship

Ich versichere, dass ich diese Arbeit selbstständig verfasst und keine anderen als die angegebenen Quellen und Hilfsmittel benutzt habe.
Heidelberg, den 27.07.2024,

Julia Schlägel